

UNIVERSITÀ DEGLI STUDI “ROMA TRE”



Corso di Dottorato di Ricerca in Fisica
XXXII Ciclo

**Search for an invisibly decaying Z' dark
boson at Belle II in $e^+e^- \rightarrow \mu^+\mu^-(e^\pm\mu^\mp)$
+ missing energy final states**

Giacomo De Pietro

Docenti guida:

Dott. Paolo Branchini

Dott. Enrico Graziani

Coordinatore:

Prof. Giuseppe Degrassi

Contents

Contents	iii
1 Theoretical framework and motivations	1
1.1 Introduction to the Standard Model	1
1.1.1 Brief summary of the mathematical formulation of SM	3
1.2 Dark Matter	4
1.3 Dark mediators and portals	6
1.4 A light vector boson as dark mediator candidate: the Z' case	7
2 The Belle II experiment	11
2.1 SuperKEKB	11
2.1.1 The nano-beam scheme	12
2.2 The Belle II detector	13
2.2.1 Detector overview	14
2.3 Vertex Detector (VXD)	16
2.4 Central Drift Chamber (CDC)	16
2.5 Particle Identification (PID)	17
2.5.1 Time-Of-Propagation counter (TOP)	17
2.5.2 Aerogel Ring-Imaging Cherenkov detector (ARICH)	18
2.6 Electromagnetic Calorimeter (ECL)	19
2.7 Superconducting magnet	20
2.8 K_L and Muon Detector (KLM)	20
2.9 Trigger	21
2.9.1 Level 1 trigger (L1)	21
2.9.2 High Level Trigger (HLT)	22
3 Analysis overview	23
3.1 Analysis overview	23
4 Data sets and event selection	25
4.1 Used data sets	25
4.2 Basic selections	27
4.2.1 Standard Z'	27
4.2.2 LFV Z'	27

4.3	Further selections	28
4.3.1	Standard Z'	28
4.3.2	LFV Z'	29
5	Recoil mass distribution and resolution	33
5.1	Recoil mass distribution	33
5.2	Recoil mass resolution	35
5.2.1	Validation using Phase 2 data	35
6	The τ suppression strategy and its optimization	39
6.1	τ suppression and optimization for standard Z'	39
6.2	τ suppression application to the LFV Z'	44
6.3	Definition of the recoil mass windows	45
6.4	Expected signal efficiencies and background yields over the entire recoil mass spectrum	46
7	Systematic uncertainties and data validation	53
7.1	Systematic uncertainties	53
7.1.1	Uncertainty related to trigger	53
7.1.2	Uncertainty related to tracking	54
7.1.3	Uncertainty related to PID	55
7.2	Validation of MC simulated samples on data	55
7.2.1	Data validation with ee sample	56
7.2.2	Data validation with $\mu\mu\gamma$ (and $e\mu\gamma, ee\gamma$) sample	57
7.2.3	Data validation with $\mu\mu$ (and $e\mu$) sample using a reversed τ suppression procedure	61
7.2.4	Trigger validation	65
7.2.5	Data validation summary	66
7.3	Summary of the systematic uncertainties	67
8	Statistical interpretation	69
8.1	The Bayesian approach	69
8.2	The model	70
8.3	Checking the background only hypothesis	70
9	Results, prospects and summary	73
9.1	Results	73
9.1.1	Standard Z'	73
9.1.2	LFV Z'	75
9.2	Prospects	77
9.3	Summary	79
	Bibliography	81

Abstract

The Standard Model (SM) is a successful and highly predictive theory of fundamental particles and interactions. However, it cannot be considered as a complete description of nature due to the fact that many phenomena, including Dark Matter, are not accounted for.

One of the simplest ways to extend the SM is by adding an extra $U(1)'$ gauge group to the theory. An additional gauge boson, here called Z' , would arise and couple to both SM and undiscovered particles such as dark matter constituents [1, 2, 3, 4]. We consider here the invisible decays of a Z' boson in two different models: 1) a Z' in the framework of a $L_\mu - L_\tau$ symmetry [4, 5]; 2) a Lepton Flavour Violating (LFV) Z' which couples to all leptons [6, 7].

Model 1) is poorly constrained at low masses, and the specific invisible decay topology is investigated here for the first time. At the moment, the only similar measurement in the framework of the $L_\mu - L_\tau$ symmetry has been performed by the BaBar experiment for a Z' decaying to muons [8]. Under a $L_\mu - L_\tau$ symmetry, the Z' boson would couple only to μ , τ and the respective ν_μ and ν_τ neutrinos among the SM particles, with a coupling constant g' . The expected branching fractions (BF) to neutrino decays are predicted to vary between 33% and 100% depending on the Z' mass [9]. In the case of kinematically accessible decays to Dark Matter particles χ , we assume $\text{BF}(Z' \rightarrow \chi\bar{\chi}) = 1$.

As far as model 2) is concerned, we address our interest here only to the LFV $e - \mu$ coupling [6, 7].

In this work we test the $L_\mu - L_\tau$ Z' model in $e^+e^- \rightarrow \mu^+\mu^- + \text{missing energy}$ processes and perform a model-independent search for a LFV Z' in $e^+e^- \rightarrow e^\pm\mu^\mp + \text{missing energy}$ processes using the 2018 data set of the Belle II detector.

Belle II operates at the SuperKEKB electron-positron collider [10] at the KEK laboratory in Tsukuba, Japan. Data were collected from April to July 2018 during the so called Phase 2 commissioning run at the center-of-mass energy of the $\Upsilon(4S)$ resonance peak. The total integrated luminosity, collected by the Belle II detector during 2018, used in this analysis is 276 pb^{-1} [11].

The signal signature is a narrow peak in the distribution of the mass recoiling against the $\mu\mu$ system in the $L_\mu - L_\tau$ Z' analysis and the $e\mu$ in the LFV case. The analysis is performed selecting events with only two tracks, identified as $\mu\mu$ or $e\mu$, and minimal activity in the electromagnetic calorimeter are selected. The selection is optimized using simulated events prior to examining data for the standard Z' . The same selection, aside from an electron in the final state, is adopted for the LFV Z' . Control samples are then used to check the estimate of the background and to infer correction factors and related uncertainties.

Upper limits to g' are computed by applying a counting technique for each bin of the recoil

mass distribution. We found no significant excess and set for the first time 90% Confidence Level (CL) upper limits to g' in the range from $\mathcal{O}(10^{-2})$ to 1.

For the LFV Z' model-independent search, upper limits are interpreted in terms of signal efficiency times cross section. We found no significant excess and set for the first time 90% CL upper limits to the efficiency times cross section of the order of 10 fb.

A paper that summarizes the results presented in this work is prepared and submitted for publication to Physical Review Letters [12].

Chapter 1

Theoretical framework and motivations

1.1 Introduction to the Standard Model

The Standard Model (SM) of elementary particles is the current theory that best describes the fundamental forces that rule the microscopic world. The SM places all the constituents of the matter and their interactions except gravity in a coherent theoretical framework. This theory is able to explain and predict all physics effects observed at a fundamental level, so it might seem that the microscopic world is well understood. However, at very different energy and space scales, astronomical and cosmological measurements reveal large effects non-explainable with SM interactions. Some of these macroscopic effects could have a microscopical origin out of SM theory. Examples are the *baryon asymmetry* (asymmetry between baryonic matter and antibaryonic matter in the observable universe, not explainable with *CP* violation from SM source), or *dark matter* (anomalies in gravitational effects explainable with a not-electromagnetic matter). Besides, several SM measurements show some tensions with respect to theoretical expectation, even if they are experimentally not significant enough to claim the discovery of New Physics.

The SM is a relativistic quantum field theory, in which the basic constituents are represented by spin- $\frac{1}{2}$ fields while interactions are mediated by spin-1 gauge bosons. All the fields (particle) in the SM acquire mass through the interaction with the spin-0 Higgs boson.

The strong force is mediated by gluons (g), massless bosons that exist in 8 color states, according to Quantum Chromodynamics (QCD), the theory of strong interactions. The strong charge which exists in three kinds, is called color, so that all colored particles interact strongly. Since gluons carry color charge they can interact with themselves.

The electromagnetic force is mediated by the photon (γ), a massless boson that exists in 2 states of polarization, and it interacts with all the particles with electric charge. This charge exists in one single kind and can assume positive or negative value. The photons do not carry electric charge.

The bosons mediating the weak force are W^+ , W^- and Z^0 , three massive bosons, two electrically charged and one neutral. Since a weak charge is assigned to all the particles, all the particles of the SM interact weakly. Electromagnetic and weak force arise from the

same symmetry group of the theory and can be treated as a single force, called electroweak interaction.

In the SM matter is composed of fermions which are divided in two main categories: quarks and leptons. The quarks interact with the electroweak force and the strong force, instead leptons interact only with the electroweak force.

There are 6 kinds of quarks, classifiable in 3 generations of doublets. Each doublet contains an up-type quark with electric charge $\frac{2}{3}e$ and a down-type quark with electric charge $-\frac{1}{3}e$, where $e \approx 1.602 \cdot 10^{-19}$ C is the absolute value of the charge of the electron. Different kind of quarks are classified according to a quantum number. The doublets are:

$$\begin{pmatrix} u \\ d \end{pmatrix}, \begin{pmatrix} c \\ s \end{pmatrix}, \begin{pmatrix} t \\ b \end{pmatrix},$$

where the letters correspond to up, down, charm, strange, top, bottom. These quantum numbers are called flavour, and they are conserved in the strong and electromagnetic interaction, but not in the weak one. In this picture, 6 quantum numbers are assigned to each quark, with all values set to 0 except the one corresponding to its kind, that will be +1 for up quarks, -1 for down quarks (for instance, a charm quark has $U = D = S = T = B = 0$ and $C = 1$, instead a bottom quark has $U = D = C = S = T = 0$ and $B = -1$). These 3 generations have a completely specular picture of antiquarks (since quarks are $\frac{1}{2}$ -spin fermions, they follow the Dirac equation), with reversed flavour number, electric charge, and color. Isolated quarks are not observable because of color-confinement principle of QCD (all observable particles isolated must be colorless), but a bound state of one quark and one antiquark (meson) or a bound state of three quark (baryon) can be colorless and so observable as isolated states. The number of quarks is not conserved in the SM processes, but the difference $N_q - N_{\bar{q}}$ is constant, implying that the lightest baryon (the proton) must be stable in the SM and that the baryon number N_B is a conserved quantity within the SM framework.

The leptons are also classified in 3 generations of doublets:

$$\begin{pmatrix} e \\ \nu_e \end{pmatrix}, \begin{pmatrix} \mu \\ \nu_\mu \end{pmatrix}, \begin{pmatrix} \tau \\ \nu_\tau \end{pmatrix},$$

where each doublet is composed by a charged and massive lepton (with electric charge $-e$) and a massless and neutral neutrino. Three more quantum numbers called *lepton family number* (L_e, L_μ, L_τ), conserved in all the known interactions¹, are defined. Each lepton has the lepton family number of its generation equal to 1 and the numbers of the other generation equal to 0. Lepton number L is defined as the sum of lepton family number. As quarks, leptons have corresponding antileptons (with reversed electric charge and lepton family number).

The Higgs Boson H is a scalar, electrically neutral and massive particle. Through the

¹The neutrino oscillation process violates the $L_{e,\mu,\tau}$ conservation and treats massive neutrinos, but is not included in the simplest version of SM. Anyway the neutrino oscillation phenomena can be included in an extended version of SM.

Higgs mechanism it gives mass to the particles that couple to it. The result is a non-trivial hierarchy of mass between the particles of the SM: the massive bosons have masses in the scale of $100 \text{ GeV}/c^2$, the quarks cover from few MeV/c^2 to about $173 \text{ GeV}/c^2$ of quark t and the massive leptons from about $0.5 \text{ MeV}/c^2$ to about $1.7 \text{ GeV}/c^2$ (in Figure 1.1 the precise values are shown). Both in quarks and leptons the mass is bigger in higher generation, thus finally the three generations appear as three copy of the same structure that differ only in mass (and therefore in available decays and lifetime). The previous statement is exactly true for leptons and it is called *lepton universality*, instead for quarks generations there are differences in couplings that generate the phenomenology of heavy flavour physics.

mass →	$\approx 2.3 \text{ MeV}/c^2$	$\approx 1.275 \text{ GeV}/c^2$	$\approx 173.07 \text{ GeV}/c^2$	0	$\approx 126 \text{ GeV}/c^2$
charge →	$2/3$	$2/3$	$2/3$	0	0
spin →	$1/2$	$1/2$	$1/2$	1	0
	u up	c charm	t top	g gluon	H Higgs boson
QUARKS					
	$\approx 4.8 \text{ MeV}/c^2$	$\approx 95 \text{ MeV}/c^2$	$\approx 4.18 \text{ GeV}/c^2$	0	
	$-1/3$	$-1/3$	$-1/3$	0	
	$1/2$	$1/2$	$1/2$	1	
	d down	s strange	b bottom	γ photon	
	$0.511 \text{ MeV}/c^2$	$105.7 \text{ MeV}/c^2$	$1.777 \text{ GeV}/c^2$	$91.2 \text{ GeV}/c^2$	
	-1	-1	-1	0	
	$1/2$	$1/2$	$1/2$	1	
	e electron	μ muon	τ tau	Z Z boson	
LEPTONS					
	$< 2.2 \text{ eV}/c^2$	$< 0.17 \text{ MeV}/c^2$	$< 15.5 \text{ MeV}/c^2$	$80.4 \text{ GeV}/c^2$	
	0	0	0	0	
	$1/2$	$1/2$	$1/2$	1	
	ν_e electron neutrino	ν_μ muon neutrino	ν_τ tau neutrino	W W boson	
					GAUGE BOSONS

Figure 1.1: Summary table of elementary particles of SM and their classifications.

1.1.1 Brief summary of the mathematical formulation of SM

The fields of the SM are the fermion fields ψ_i (where i is the kind of fermion), the gluons fields G_a (where a runs from 1 to 8), the electroweak fields W_1, W_2, W_3 and B , the Higgs field φ . The SM is a gauge theory and its group of symmetry is:

$$SU(3)_C \otimes SU(2)_L \otimes U(1)_Y ,$$

where $SU(3)_C$ is the gauge group of QCD and acts on G_a (where the subscript C is for “color”), $SU(2)_L \otimes U(1)_Y$ is the gauge group of electroweak theory, and $SU(2)_L$ acts on $W_{1,2,3}$ and φ , and $U(1)_Y$ acts on B and φ (where the subscript L is for “left” and Y is for “hypercharge”).

Inside the lagrangian of the SM a kinetic term of free field ($C_{\mu\nu}C^{\mu\nu}$, where $C_{\mu\nu}$ is the gauge tensor associated with the field) is present for B, W and G and then the dynamical terms of interaction between fermions and boson fields. (i.e. an electroweak term \mathcal{L}_{EW} , where B and W_j enter, and a chromodynamic term \mathcal{L}_{QCD} , where G_a enters) are present.

A trivial mass term in the form $C^\mu C_\mu$ (where C is a generic field) is forbidden to keep the theory gauge invariant, but with the introduction of a complex scalar field φ , it is possible

to “give mass to vector bosons”. This spontaneous symmetry breaking mechanism gives to the Higgs field a non-vanishing vacuum expectation value that represents a mass-scale of the model. In conclusion, the Higgs mechanism mix the four electroweak field to obtain three massive field, W^\pm charged fields and the Z^0 field, and the photon massless field A (with own symmetry group $U(1)_{EM}$).

The Higgs Mechanism can be extended to give to the fermions their masses adding a Yukawa term (a term that couple a scalar and a fermion field, like $\bar{\psi}\varphi\psi$) in the lagrangian. The mass scales of the fermions (the coupling constant of these terms) are free parameters of the SM.

The SM does not have any of the simpler discrete symmetry: the charge conjugation C which inverts all the internal quantum numbers of a particle transforming particle into its antiparticle, the parity operator P which reverses the spatial coordinate and momenta of a particle and the time reversal T which inverts the arrow of time are not conserved in the SM processes. In addition, the electroweak interaction violates also the combination CP . Instead the combination of the three symmetries CPT is a symmetry of the SM.

A comprehensive review of the SM can be found in [13].

1.2 Dark Matter

Astrophysical and cosmological observations of Dark Matter (DM) are perhaps the most persuasive experimental evidence for physics beyond the SM. DM may not be composed of particles at all, but the SM in describing ordinary matter gives us a strong reason to consider a particle description of DM as well.

Although there are several evidences of its existence at different scales, very little is known about DM. We know that DM constitutes about 25% of the energy density of our universe (being 5 times more abundant with respect to the known SM matter) and also that has a key role in the comprehension of the evolution of the universe itself. Moreover, we know that DM is coupled to SM particles, as well as by gravitational force, at most at the weak interactions scale and is stable on cosmological timescales. Most of the DM properties are still unknown.

The first and oldest evidence of the DM existence concerns the observation of the rotational velocity of galaxies, which could not be explained by only the barionic visible mass. Rubin and collaborators extensively studied more than 60 galaxies [14], measuring the rotational velocity from the analysis of the spectral lines (Doppler effect). In absence of invisible mass, the velocity of stars in the galaxy should be described as the velocity of our planet around the Sun, thus $v(r) = \sqrt{Gm(r)/r}$, where $v(r)$ is the velocity, G is the gravitational constant and $m(r)$ is the mass within a radius r . The dependence from the radius goes as $1/\sqrt{r}$, decreasing as the distance from the center increases. Surprisingly the data observed showed a flat behaviour, meaning that the velocity does not decrease with increasing distances. The expected and observed behaviours are shown in Figure 1.2. The agreement is restored if an invisible massive halo fills all the space and it is not concentrated, as the ordinary mass, close to the central bulge of the galaxy.

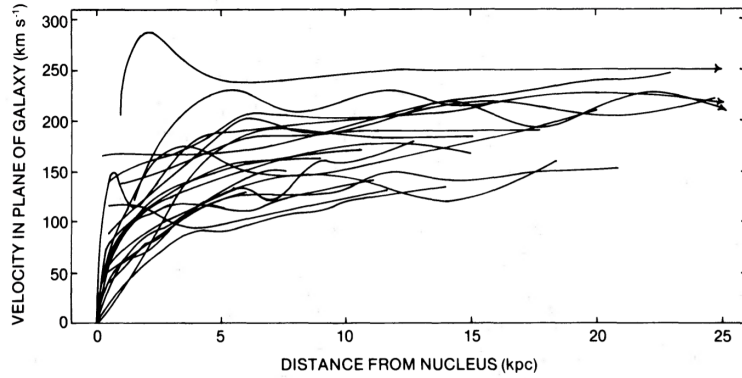


Figure 1.2: Rotational velocity of the galaxies (measured by Rubin and collaborators) as a function of their radius [14].

The second evidence derives from the observation of the gravitational lensing effect. This effect is due to the deformation of the spacetime in presence of a mass affecting the motion of bodies and light. Gravitational lensing effect allows, due to the bending of the light, to spot objects placed directly behind a closer one. Without entering into details, from the reconstructed image of the hidden object it is possible to determine the amount of mass generating the gravitational effect. As an example, observations performed on Abell 370 cluster led to an estimation of the total mass of the cluster to be between 10^2 and 10^3 times the observed one [15].

Other important evidences are provided by the measurement of the anisotropies in the cosmic microwave background and by collisions of a galaxy cluster, called “bullet”, with a bigger one.

Currently there are three possible experimental methods used to investigate the particle nature of DM: direct detection, indirect detection and direct production at colliders.

Direct detection of DM particles is based on the assumption that a constant flux of them may pass through the Earth and weakly interacts with the ordinary matter. It would be thus possible to measure the recoil energy of nucleons weakly interacting with these particles. The experimental setup should then include a huge detector which has to be optimized to minimize the background contamination: the most important backgrounds usually come from cosmic rays, natural radioactivity and the intrinsic radioactivity of the detector. The DM interaction with the detector’s nuclei can have different features: it could be either elastic or inelastic, spin-dependent or spin-independent. Up to now, experiments of direct detection just came to set upper and lower limits of the DM mass and couplings, without revealing their nature.

The idea behind the indirect detection is to detect the SM particles produced in the annihilation of DM particles far in the universe, that occurs with a high probability in regions of space with high density of DM, like galaxies centers. Antiparticles, neutrinos and gamma rays are the most useful annihilation products to be detected. For this reason the indirect strategy focuses on finding an excess in the flux of the annihilation products. Identifying the possible source of the flux and observe whether it could be a region containing a large density of DM or not helps to discriminate between background and DM decay products.

Assuming that DM particles interacts with the SM ones, they can also be produced at

colliders. As said before, DM particles have to be stable and, as they only interact weakly with ordinary matter, they escape the detector. However, the presence of a DM particle would leave a distinctive signature inside the detector: as DM escapes detection, an energy imbalance is expected to be measured.

1.3 Dark mediators and portals

In many models, DM particles couple to SM through the effect of new dark mediators. Depending on the type of the dark mediator, different “portals” between the SM and the DM particles can be identified:

- a *scalar portal*, in which a new scalar particle S can couple to the SM Higgs field φ : $\mathcal{L} \supset \mu S \varphi^\dagger \varphi + \lambda S \varphi^\dagger \varphi$; if this scalar acquires a vacuum expectation, it can mix with the SM Higgs;
- a *pseudoscalar portal*, in which a new pseudoscalar particle a can couple to the SM fermionic fields ψ : $\mathcal{L} \supset (\partial_\mu a / f_a) \bar{\psi} \gamma^\mu \gamma^5 \psi$; this term is obtained, for example, from the spontaneous breaking of a global symmetry, where f_a is the scale at which the symmetry is broken, and if the scale f_a is sufficiently large, the pseudoscalar particle naturally obtains a small mass and small couplings; in addition to fermionic couplings, this kind of mediator generally induces couplings to the SM gauge bosons: $\mathcal{L} \supset -\sum_i (\alpha_i C_i / 8\pi f_a) F_{(i)\mu\nu} \tilde{F}_{(i)}^{\mu\nu} a$, where $i = Y, 2, 3$ labels the different gauge groups of the SM, $F_{(i)\mu\nu}$ denotes the corresponding field strength tensor and $\tilde{F}_{(i)}^{\mu\nu}$ is the dual field strength tensor;
- a *neutrino portal*, in which a new fermionic particle N can couple to the SM fields: $\mathcal{L} \supset y_N L \varphi N$, where y_N is the Yukawa coupling and L is the $SU(2)_L$ fermionic doublet; in this case, N can be an heavy (sterile) right handed neutrino, typically invoked for generating a SM neutrino mass term;
- a *vector portal*, in which a new vector particle A' can couple to the SM fermionic fields: $\mathcal{L} \supset g' \bar{\psi} \gamma^\mu \psi A'_\mu$, where g' is the coupling constant of the new interaction; the A' can also couple with the ordinary SM photon through the kinetic mixing mechanism: $\mathcal{L} \supset (\epsilon/2) A'_{\mu\nu} F_Y^{\mu\nu}$, where ϵ is the kinetic mixing parameter and $A'_{\mu\nu}$ ($F_Y^{\mu\nu}$) is the field strength tensor of the A' (hypercharge) vector field.

Each of the new particles introduced above can be also a viable DM candidate [16], provided it is sufficiently light and its couplings to the SM are so small that it is stable on cosmological timescales.

Depending on the details of the model, the introduced mediators can couple to both quarks and leptons, only to quarks (leptophobic) or only to leptons (leptophilic). In principle, they can also couple with different strength to down-type quarks and to up-type quarks. The scalar and the pseudoscalar mediators are furthermore expected to couple to fermions proportional to their mass. The crucial point is that - in contrast to DM candidates from

portal interactions - mediators from portal interactions may have sizeable couplings to the SM, which can potentially be probed in particle colliders through the direct production.

Once produced, the mediator can have three different types of decays: invisible decays, leptonic decays or hadronic decays. If the DM mass is less than half of the mediator mass, the first decay mode is expected to be the dominant one and the production of the mediator will lead to missing momentum in the detector. If invisible decays are kinematically forbidden, there will typically be both leptonic and hadronic decays (unless of course the mediator is either leptophilic or leptophobic). For scalar and pseudoscalar mediators the leptonic decay modes will be dominated by the heaviest lepton that is kinematically accessible, while vector mediators are usually postulated to couple democratically with all the available leptons. Calculating the hadronic branching fractions for mediators in the GeV range is a difficult problem due to the onset of non-perturbative effects.

1.4 A light vector boson as dark mediator candidate: the Z' case

It is usually denoted with Z' the class of a viable extension of the SM which deals with a new light dark boson associated to an additional $U(1)$ gauge symmetry. In this work two interesting theoretical frameworks have been considered:

1. a Z' boson belonging to the $L_\mu - L_\tau$ symmetry;
2. a Z' boson coupling to all leptons and violating the lepton flavor conservation.

The first case deals with a light vector boson in the mass range of $\approx 100 \text{ MeV}/c^2$ to tens of GeV/c^2 and with a new coupling constant $g' \approx 10^{-6} - 10^{-3}$, which gained a lot of attention also from a theoretical point of view thanks to the minimal gauged $U(1)_{L_\mu - L_\tau}$ model, achievable by gauging the $L_\mu - L_\tau$ current. This model predicts a dark vector boson candidate coupled only to the heaviest generations of leptons (μ , τ and their corresponding neutrinos ν_μ , ν_τ), free of gauge anomalies without any extension of particle content [4, 5].

Moreover, it can solve many open issues in particle physics, like the well-known discrepancy associated with the muon anomalous magnetic moment, but also the high energy cosmic neutrino spectrum, and the problem of DM abundance by providing a way to balance the annihilation rate to sterile neutrinos in the early universe. Furthermore, it may explain the rare B decay anomalies observed in the $B \rightarrow K^{(*)}l^+l^-$ analyses [17].

This gauge interaction is well-hidden from most experiments due to its lack of coupling to first-generation leptons. In addition, it is still poorly constrained in the low mass region and the invisible decay signature has been investigated in this work for the first time. Currently, the only existing limits for the low mass range are provided by the BaBar search [8], which searched for a visible final state with the Z' decaying into a pair of muons and therefore it cannot provide any information below the dilepton invariant mass threshold, and by neutrino-nucleus scattering processes at neutrino beam bump experiments, as measured by the CCFR experiment [18, 19]. The existing limits are shown in Figure 1.3.

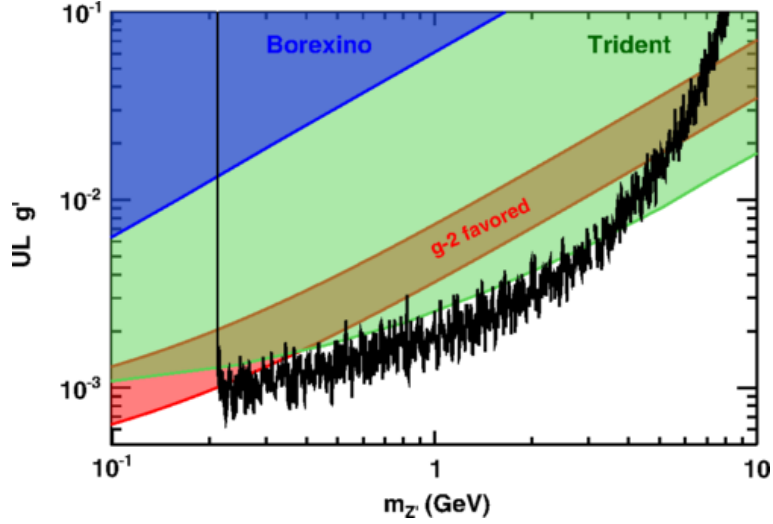


Figure 1.3: Existing limits at 90% CL on the new coupling constant g' as a function of the Z' mass measured by BaBar, together with the constraints derived from the neutrino-nucleus scattering processes measured by CCFR [8]. The region consistent with the discrepancy between the calculated and measured anomalous magnetic moment of the muon within 2σ is shaded in red.

The Feynman diagram depicting the process of interest for this search in e^+e^- collisions is shown in Figure 1.4. The lagrangian interaction in the $L_\mu - L_\tau$ model can be written as:

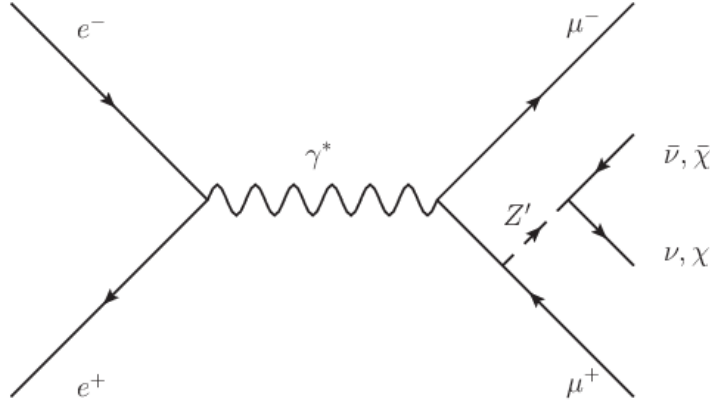


Figure 1.4: The Feynman diagram for the production of a light Z' in e^+e^- annihilations into a pair of muons, accompanied by the subsequent Z' decay to neutrinos ($\nu\bar{\nu}$) or DM candidates ($\chi\bar{\chi}$).

$$\mathcal{L} = \sum_l \theta g' \bar{l} \gamma^\mu Z'_\mu l ,$$

where $l = \mu, \tau, \nu_\mu^L, \nu_\tau^L$ and $\theta = -1$ if $l = \mu, \nu_\mu^L$ or $\theta = +1$ if $l = \tau, \nu_\tau^L$. The partial decay widths are given by [20]:

$$\Gamma(Z' \rightarrow l^+l^-) = \frac{(g')^2 M_{Z'}}{12\pi} \cdot \left(1 + \frac{2M_l^2}{M_{Z'}^2}\right) \cdot \sqrt{1 - \frac{4M_l^2}{M_{Z'}^2}} \cdot \theta(M_{Z'} - 2M_l) ,$$

$$\Gamma(Z' \rightarrow \nu_l \bar{\nu}_l) = \frac{(g')^2 M_{Z'}}{24\pi} .$$

The expected Branching Fractions (BF) of final states with neutrinos, according to the considered mass regime, are:

$$\begin{aligned} \text{BF}(Z' \rightarrow \nu\bar{\nu}) &= 1 & \text{for } M_{Z'} < 2M_\mu, \\ \text{BF}(Z' \rightarrow \nu\bar{\nu}) &\approx 1/2 & \text{for } 2M_\mu < M_{Z'} < 2M_\tau, \\ \text{BF}(Z' \rightarrow \nu\bar{\nu}) &\approx 1/3 & \text{for } M_{Z'} > 2M_\tau. \end{aligned}$$

It is assumed that, if DM candidates χ with mass $2M_\chi < M_{Z'}$ exist, then the Z' will decay to DM particles with $\text{BF}(Z' \rightarrow \chi\bar{\chi}) = 1$.

As far as the second theoretical framework is concerned, the Z' can couple to all leptons and charged Lepton Flavour Violation (LFV) is also embedded, resulting in enabled final states for which a small SM background is expected [6, 7]. We focus here only on the LFV $e - \mu$ coupling.

While the presence of LFV mediators can be constrained by measurements of the forward-backward asymmetry in $e^+e^- \rightarrow \mu^+\mu^-$ [21], we present here a direct, model-independent search of $e^+e^- \rightarrow e^\pm\mu^\mp Z'$, $Z' \rightarrow$ invisible. A possible Feynman diagram depicting the process of interest for this search in e^+e^- collisions is shown in Figure 1.5.

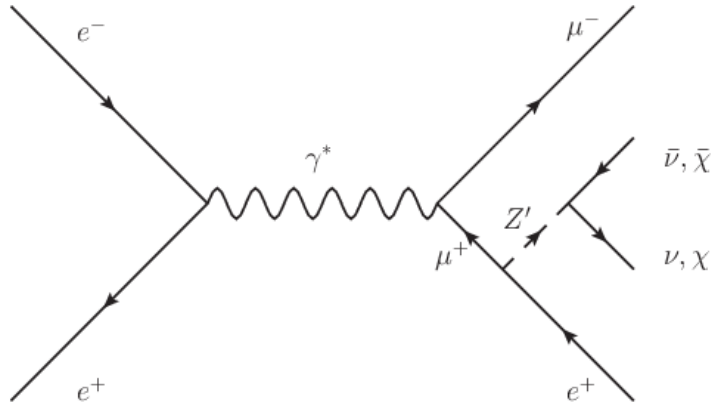


Figure 1.5: The Feynman diagram for the production of a light LFV Z' in e^+e^- annihilations into a pair of an electron and a muon, accompanied by the subsequent Z' decay to neutrinos ($\nu\bar{\nu}$) or DM candidates ($\chi\bar{\chi}$).

Chapter 2

The Belle II experiment

The Belle II experiment at the SuperKEKB e^+e^- collider represents the new generation of B -Factory, which is going to collect an integrated luminosity of 50 ab^{-1} at $\Upsilon(4S)$ resonance, with the goal to refine several measurements in heavy flavour sector of SM and searching for New Physics signatures. In this chapter, we give a detailed description of the SuperKEKB collider and of the Belle II detector.

2.1 SuperKEKB

The new generation of B -Factory is represented by SuperKEKB, the upgraded collider of KEKB, located at the KEK Laboratory in Tsukuba, Japan. The upgrade operations started in 2010. The main motivation for this substantial upgrade is to increase the instantaneous luminosity of the machine from $2.1 \cdot 10^{34} \text{ cm}^{-2}\text{s}^{-1}$ (KEKB) to $8 \cdot 10^{35} \text{ cm}^{-2}\text{s}^{-1}$, to reach the statistic needed for the physics goals of the Belle II experimental program. This luminosity increase is obtained by using a larger beam current and by a smaller beam dimension at the Interaction Point (IP), with the use of the nano-beam scheme, for which is crucial to keep the beam emittance as low as possible [10].

SuperKEKB is an e^+e^- asymmetric circular collider, with an energy of 7 GeV (4 GeV) for the electron (positron) beam. The resulting center-of-mass energy is $\sqrt{s} \approx \sqrt{4E_{e^+}E_{e^-}} = 10.58 \text{ GeV}$.

The electrons are produced in a pre-injector by a pulsed laser directed on a cold cathode target, then they are accelerated by a linear accelerator (LINAC) to 7 GeV and injected in the High Energy Ring (HER) of SuperKEKB. The positrons are produced by the collision of electrons with a tungsten target and then they are injected in a damping ring to reduce their emittance. When the positrons reach the required emittance they are accelerated to 4 GeV in the LINAC and then injected in the Low Energy Ring (LER).

The two beams collide at the IP with a large crossing angle and with the peculiar nano-beam scheme (described in the following section), one of the major upgrade of SuperKEKB intended to improve the luminosity of the collider. This new colliding scheme required a redesign of the final focus system.

The beam asymmetry produces a Lorentz boost between the frame of the center-of-mass of the colliding leptons and the detector rest frame (i.e. the laboratory frame) equal to

$\beta\gamma \approx 0.28$, equivalent to an average flight distance for the B mesons of $130 \mu\text{m}$. This distance is sufficient to track the displaced vertex of the B mesons, but is reduced with respect to KEKB ($\beta\gamma$ was 0.42). This is due to the exponential increase of the power absorption, which sets a limit to the energy of the HER. On the other hand the beam geometry at IP and the bunch shape, that need a strongly reduced dispersion of the bunches, set a lower limit to the LER energy: to obtain the same $\beta\gamma$ of KEKB the energy of the LER should be reduced to 3.5 GeV, but this implies higher beam losses due to Touscheck scattering, that are not sustainable for the luminosity requirements.

The luminosity requirement imposed several other modifications to the accelerator structure: the electron injection and positron target are modified, the damping ring, the radio-frequency system, the optics, the beam pipe and the vacuum system are renewed.

The data taking program of the SuperKEKB collider is subdivided in three main phases:

- Phase 1 (2016): a preliminary phase without final focus and without collisions, used to evaluate beam background with dedicated detectors [22] (the Belle II detector was moved out of the beam line);
- Phase 2 (2018): run with the final focus, but at low luminosity to calibrate and tune the accelerator and the detector response and with a partial Vertex Detector installed [23];
- Phase 3 (from 2019): run at full luminosity with the complete Belle II detector. Most of the data are going to be collected at the $\Upsilon(4S)$ resonance, but runs at different center-of-mass energies are foreseen.

2.1.1 The nano-beam scheme

The nano-beam scheme aims to reduce the beam size at IP in order to increase the luminosity. The luminosity of a collider is given by:

$$\mathcal{L} = \frac{\gamma_{\pm}}{2er_e} \left(1 + \frac{\sigma_y^*}{\sigma_x^*} \right) \frac{I_{\pm}\xi_{y\pm}}{\beta_{y\pm}^*} \cdot \frac{R_L}{R_{\xi_y}},$$

where γ is the relativistic Lorentz factor, e is the absolute value of the electron charge, r_e is the classical radius of electron, σ_x^* and σ_y^* are the widths of the bunch at IP on the transverse plane, I is the current of the beam, β_y^* is the vertical betatron function at the IP, ξ_y is the vertical beam-beam parameter, R_L and R_{ξ_y} are the reduction factors of luminosity and the vertical beam-beam parameter due to not-vanishing crossing angle and the \pm sign refers to the charge of the particles in the beam¹.

The idea of the nano-beam is to strongly reduce the vertical betatron function with the minimization of the longitudinal size of the beam overlap at IP (Figure 2.1). The size of the effective overlap region is $d \approx \sigma_y^*/\phi$, where 2ϕ is the crossing angle of the beams. For this reason, the crossing angle has been chosen $2\phi = 83 \text{ mrad}$ (about four times the KEKB crossing angle). In addition σ_y^* is reduced to the size of tens of nm to reach a beam size at IP of 50 nm (from order of 1 μm of KEKB). In conclusion, with this scheme the betatron

¹It is important to notice that the vertical beam-beam parameter ξ_y is proportional to the ratio I_{\mp}/γ_{\pm} , so the formula for the luminosity given here is not asymmetric if the two signs are swapped.

function β_y^* is reduced by a factor 20 with respect to KEKB and since $\sigma_y^* \ll \sigma_x^*$, $R_L/R_{\xi_y} \approx 1$ and $\xi_y^{\text{SuperKEKB}} \approx \xi_y^{\text{KEKB}}$, the current of the beams must be doubled to reach the required luminosity.

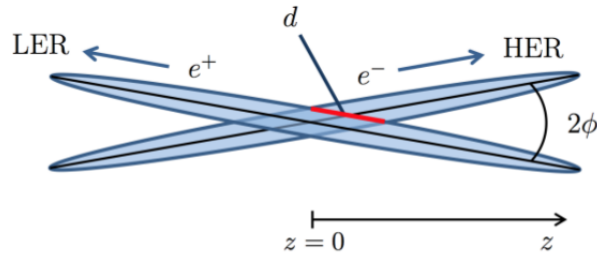


Figure 2.1: The geometry of the IP in the nano-beam scheme. The effective longitudinal overlap size d is highlighted in red.

The main SuperKEKB IP parameters are summarized in Table 2.1.

Table 2.1: SuperKEKB parameters compared to the KEKB parameters.

	KEKB (LER / HER)	SuperKEKB (LER / HER)
E (GeV)	3.5 / 8.0	4.0 / 7.0
2ϕ (mrad)	22	83
ξ_y	0.129 / 0.090	0.090 / 0.088
β_y^* (mm)	5.9 / 5.9	0.27 / 0.41
I (A)	1.64 / 1.19	3.60 / 2.62
σ_x^* (μm)	1.64 / 1.19	7.75 / 10.2
σ_y^* (nm)	1.64 / 1.19	59 / 59
\mathcal{L} ($10^{35} \text{ cm}^{-2} \text{ s}^{-1}$)	0.211	8

2.2 The Belle II detector

Belle II is the detector designed for the SuperKEKB collider, and it is a substantial upgrade of the Belle detector. It is a general purpose experiment, optimized for the reconstruction of $\Upsilon(4S) \rightarrow B\bar{B}$ events, with the capability to perform efficient tracking of charged particles, in particular in the low momentum range (down to 50 MeV/ c). In addition, a neutral identification system is present, based on precise γ detection, and a multi-detector Particle Identification (PID) system. Anyhow an efficient reconstruction of τ pairs and low multiplicity events is allowed too. Belle II integrates a high efficiency and low bias hardware and software trigger to cope with the high background conditions expected at SuperKEKB. The high-resolution momentum and vertex reconstruction allows precise time-dependent measurements. In addition, the detector hermeticity and the knowledge of the initial state allow to perform missing mass analysis and use recoil techniques. Because of the low momentum range studied by the experiment a crucial feature of the detector is the material budget, kept as low as possible.

A comprehensive description of the Belle II detector can be found in [24] and [25].

2.2.1 Detector overview

The detector has an approximate cylindrical symmetry around the z -axis (set along the bisector of the angle between the direction of the electron beam and the reverse direction of the positron beam), while it has a significant forward-backward asymmetry to improve the solid angle acceptance in the boost (forward) direction. The general structure of the detector is shown in Figure 2.2.

From the innermost to the outermost sub-detector system Belle II is composed by:

- Pixel Detector (PXD): 2 layers of pixel sensors (DEPLETED Field Effect Transistor technology);
- Silicon Vertex Detector (SVD): 4 layers of Double-Sided Silicon Strip sensors; the PXD and the SVD form the Vertex Detector (VXD);
- Central Drift Chamber (CDC): helium-ethane wire drift chamber, composed of 56 layers with stereo and longitudinal geometry;
- Particle Identification System (PID): a Time-Of-Propagation (TOP) counter with a quartz radiator for the barrel region with a Cherenkov quartz radiator, and an Aerogel Ring-Imaging Cherenkov (ARICH) detector, with an aerogel radiator for the forward endcap region;
- Electromagnetic Calorimeter (ECL): an homogeneous calorimeter composed of more than 8000 CsI(T) crystals that provide 16.1 radiation lengths X_0 ;
- Superconducting magnet: a NbTi/Cu magnet that provides a homogeneous magnetic field of 1.5 T parallel to the beam direction in the internal region;
- K_L and Muon Detector (KLM): alternated layers of Resistive Plate Chambers (RPCs) and iron plates in the outermost barrel region and scintillator strips in the innermost barrel region and in both endcaps; it provides about 4 interaction lengths, in order to detect the particles that escape from the internal region; the iron structure of the KLM detector is used as return yoke of the magnetic field.

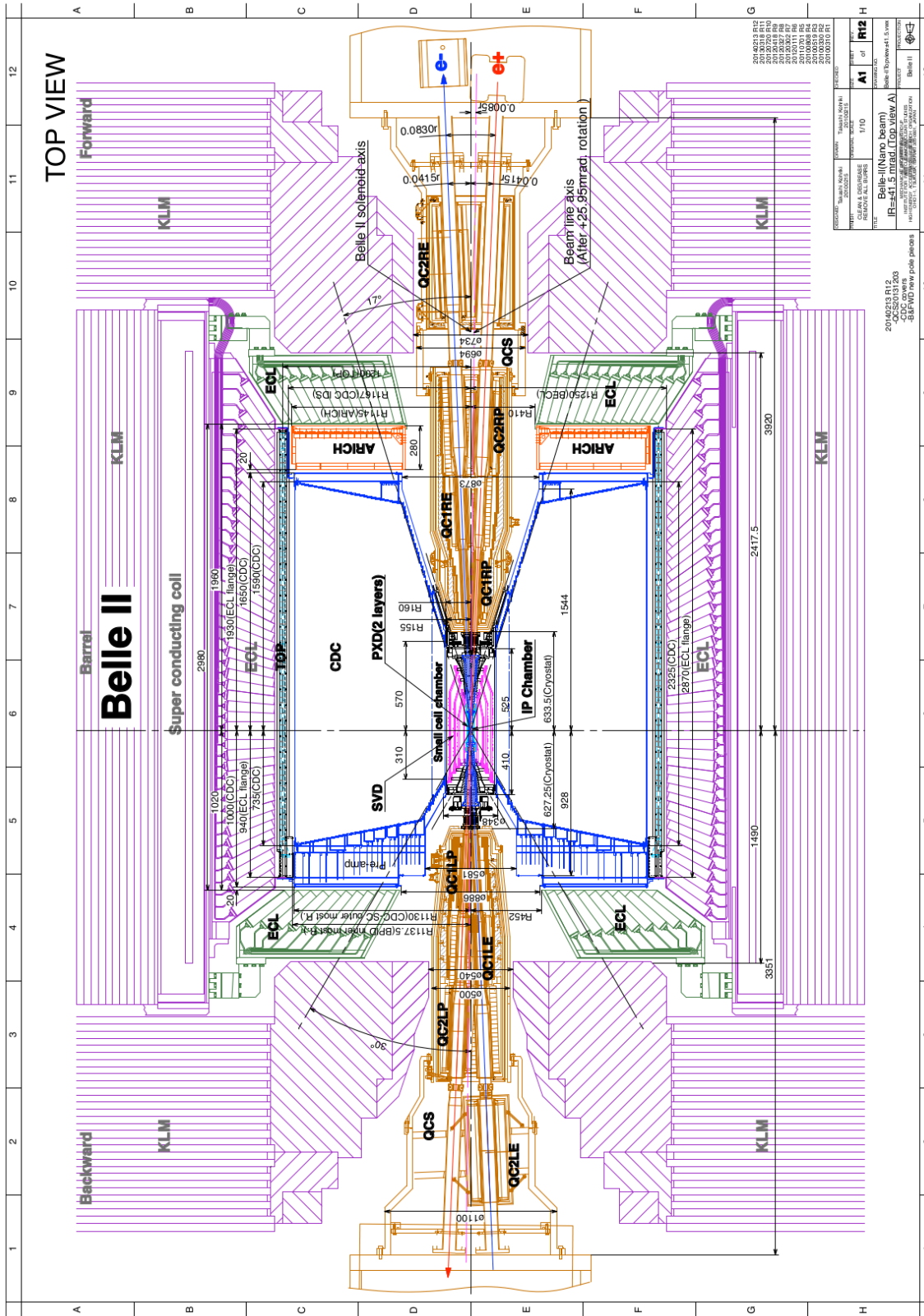


Figure 2.2: Top view of Belle II, with all the subdetectors highlighted, and the IP region.

2.3 Vertex Detector (VXD)

The VXD is the innermost sub-detector of Belle II. It is composed of two devices, the Pixel Detector (PXD) and the Silicon Vertex Detector (SVD), forming a 6-layer silicon vertex detector. It is a completely new device with respect to the SVD of Belle.

The PXD is composed of two layers of pixelated sensors with DEPFET (DEPLETED Field Effect Transistor) technology, to obtain a low material budget of $0.2X_0$ per layer in the detection region. The layers are placed at 14 mm and 22 mm from IP while the beam pipe radius is about 10 mm. The pixelated sensors have been chosen to sustain the higher hit rate due to the shorter distance from IP and the higher luminosity with respect to Belle. This solution allows keeping the occupancy of the detector at about 3% (where the occupancy is defined as the number of activated channels at the same time over the total number of channels). The amount of data provided by the PXD in a single event is nonetheless higher than the accepted Data Acquisition (DAQ) rate, therefore the charged tracks are reconstructed online using the SVD and CDC information and then extrapolated onto the PXD sensors during the High Level Trigger process. This extrapolation determines some Regions Of Interest (ROI) from which the PXD hits are selected for readout, allowing the system to remain within the DAQ bandwidth.

The SVD is composed of four layers of Double-Sided Silicon Strip Detector, placed at 38 mm, 80 mm, 115 mm, and 140 mm from IP. SVD uses several types of sensors, each with different shapes and strip pitch. An original feature of the SVD is the Origami chip-on-sensor concept, an innovative solution that uses a flexible fan-out to put all the readout chips on the same side of the modules in the detection region to reduce the connections and simplify the cooling system.

2.4 Central Drift Chamber (CDC)

The CDC is a wire drift chamber with three main functions in Belle II: first it is the main tracking device to precisely measure momenta, second it provides PID information by measuring the energy losses in the gas volume, third it is used in hardware and software trigger.

The chamber is composed of 8 superlayers formed by 6 layers of wires each, and an innermost superlayer formed by 8 layers of wires. The chamber is filled with a mixture of helium and ethane (50% He, 50% C₂H₆), and the entire CDC is closed by two carbon cylinder and 2 aluminium endplates. Two classes of wires are present: the field wires producing the accelerating electric field, and the sense wires collecting the released charge. The field wires are composed of aluminium and are thicker (126 μm of diameter) than the sense wires, which are made of gold-plated tungsten and have a diameter of 30 μm . The radial cell size is 10 mm for the innermost superlayer and 18.2 mm for the other superlayers. When a charged particle crosses the CDC ionize the gas mixture of the chamber producing electrons. The electrons are accelerated by the electric field and produce a charge avalanche that induces a signal on the sense wires, from which is possible to reconstruct the drift time and thus the initial particle position.

The front-end electronics is located near the backward endplate, and it uses an ASIC chip to amplify, shape and discriminate the signal. A TDC is used to measure the drift time and a FADC to measure the signal charge.

To obtain the z position information from the CDC, half of the superlayers have a stereo wire configuration. It means that the wires are not strictly parallel to the z -axis, but present a small angle on the r - ϕ plane. With the use of different inclinations it is possible to reconstruct the 3D position. There are 3 classes of classes of superlayer, one axial (“A”) and two stereo (“U”, “V”). The configuration of the 9 superlayers is “AUAVAUAVA”, chosen to optimize the trigger z resolution.

The innermost radius of CDC is 160 mm, larger than the Belle one (77 mm), because the higher expected background rates would make the chamber unusable at smaller radius. A complex endplate geometry is employed to ensure good angular coverage while limiting occupancy, especially from Bhabha scattering in the forward direction. The outermost radius is 1130 mm, larger than the Belle one (880 mm) because the PID barrel device of Belle II is more compact than in Belle. The angular acceptance is the same of VXD ($\theta \in [17^\circ, 150^\circ]$) to be able to merge all the tracks of two sub-detectors. The position resolution of CDC is about 100 μm , while the dE/dx resolution is about 12% for particles with $\theta \approx \frac{\pi}{2}$.

2.5 Particle Identification (PID)

The main devices for PID in Belle II located outside the CDC are the TOP in the barrel region and the ARICH in the forward endcap region. Both systems detect Cherenkov light, but the operating principles are substantially different, thus they are described separately. The idea of Cherenkov detectors is to measure the θ_C angle of photons emitted by relativistic charged particles crossing a radiator material, obtaining β of the particle with the relation $\cos\theta_C = 1/n\beta$, where n is the refractive index of the material. In Belle II, using the independent momentum measurement in the tracking system and the measurement of β combined to the energy loss measured in the CDC the mass of the particles is determined. A PID likelihood is defined with the use of the measured momentum of the track, and various charged particle hypotheses are tested with a “PID selector” that compares the likelihood ratio between various mass hypothesis. The tested particles are pions, kaons, electrons, muons, protons and deuterons.

2.5.1 Time-Of-Propagation counter (TOP)

The structure of the TOP is shown in Figure 2.3: a single TOP module is made of a quartz bar with a focusing mirror in the forward region and an array of photomultipliers (PMT) in the backward region.

The operating principle of the TOP detector is to obtain θ_C from the measurement of the time of arrival of the Cherenkov photons from the emission point as a function of the angle of the Cherenkov cone Φ on the plane of the bar. From the combined information of the arrival time t_{TOP} , Φ and position and direction of the main particle provided by tracking, it is possible to extract the θ_C information. The complete discussion is omitted here, for

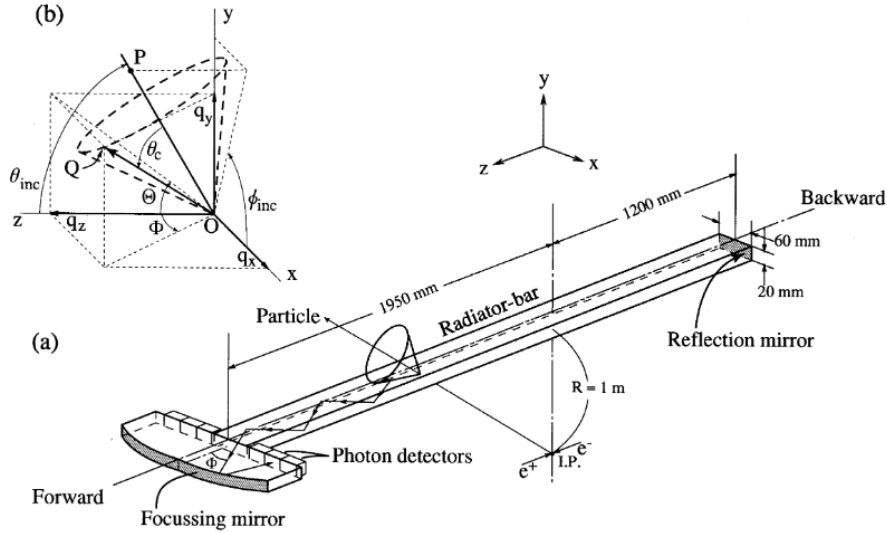


Figure 2.3: Scheme of a single module of the TOP detector. Note that the values in the figure refer to a prototype version of a TOP module and slightly differ to the actual ones.

details see [4].

In the TOP detector the emitted photons are reflected internally in the quartz bar and reach the focussing mirror in the forward region. The mirror is built to conserve the Φ angle information and to reflect the photons to a specific PMT channel that measure the t_{TOP} . Thus the Φ angle is evaluated depending on the PMT activated channel. The photons emitted in the backward directions are first reflected by a mirror at the end of the quartz bar and directed to the focussing mirror.

The entire TOP detector is made of 16 modules set around the CDC at 1.2 meter of radius from IP, with an angular acceptance of $\theta \in [31^\circ, 128^\circ]$. The bar quartz dimension is $0.45 \text{ m} \times 2 \text{ cm} \times 2.75 \text{ m}$. The TOP has a single photon time resolution of about 100 ps, achieved with 16 channel micro-channel plate PMTs. Instead the production time of the main particle is known with the precision of about 50 ps.

2.5.2 Aerogel Ring-Imaging Cherenkov detector (ARICH)

The ARICH is a proximity focusing Ring-Imaging detector, which uses as radiator two layers of aerogel. An expansion volume of 20 cm divides the radiator from a ring of hybrid avalanche photon detector (HAPD), and allows the Cherenkov photons to enlarge into rings.

The performance of RICH detectors depends on the number of detected photons N_γ and the single photon resolution on the Cherenkov angle σ_{θ_C} . N_γ increases with the thickness of the radiator and the resolution per track improves as $\sigma_{\theta_C}/\sqrt{N_\gamma}$, but σ_{θ_C} degrades due to the uncertainty of the emission point. In the Belle II ARICH a peculiar solution is adopted to optimize the performance: two layers of aerogel with different refractive indexes ($n = 1.045$ upstream and $n = 1.055$ downstream) and 2 cm thickness are used, so that the two produced rings are overlapped on the detection surface, giving the N_γ equivalent to a double radiator thickness.

The reached resolution is $\sigma_{\theta_C} \approx 13 \text{ mrad}$, optimized for charged tracks with momentum

larger than 3.5 GeV/ c , but the σ_{θ_C} doesn't show significative degradation also for lower momentum tracks. With $N_\gamma \approx 10$ per ring, the resolution of a single track is about $\sigma_{\theta_C} \approx 3$ mrad. The angular acceptance is $\theta \in [14^\circ, 30^\circ]$.

2.6 Electromagnetic Calorimeter (ECL)

The ECL has several central roles in Belle II. First, it detects photons with high efficiency and measures their energy and angle. Secondly, it identifies electron and contributes to the K_L detection with the KLM sub-detector. Third, it generates a hardware and software photon trigger. In addition, the ECL is used to monitor online and offline the luminosity of SuperKEKB.

The Belle II ECL uses the same crystals of Belle's calorimeter, but a complete upgrade of the readout electronics was needed to cope with the SuperKEKB increased luminosity. The calorimeter is subdivided into three regions, the barrel region, the forward and the backward region, and they collectively cover 90% of the solid angle in the center-of-mass system (with an angular acceptance of $\theta = [12.4^\circ, 155.1^\circ]$). The barrel region is extended for 3 meters and has an inner radius of 1.25 m. The annular endcap regions have the internal base at $z = 1.96$ m (forward) and $z = -1.02$ m (backward) from IP. There are two gaps of 1° between the barrel and the endcaps regions to allow the passage of the cables of internal sub-detectors.

The ECL is a homogeneous highly segmented calorimeter, composed by 8736 crystals of CSI(Tl) (caesium iodide thallium-doped). The crystals have a shape of a truncated pyramid with a length of 30 cm and a 6×6 cm² base, equivalent to $16.1 X_0$. The crystals are assembled in 8 cells separated by 0.5 mm thick aluminium septum walls and closed by two cylinders. Each cell provides the optimal operating environment for the crystals in term of humidity and temperature by a dry air flushing and a water cooling system.

At the external bases of the crystals 10×20 mm² photodiodes are glued with a 1-mm plexiglass plate collecting light from the scintillating material. Each photodiode has a LED to inject light pulses into the crystal volume to monitor the optical stability. The relatively long decay time of scintillations in CsI(T) (1 μ s), in the presence of elevated background level expected in Belle II, produces a not negligible overlapping of pulses from neighbouring background events. Therefore the new readout electronics samples the photodiodes' signals in 16 points and then fits the signal shape with a predefined proper function.

The energy resolution of ECL, from a prototype test, is given by:

$$\frac{\sigma_E}{E} = \sqrt{\left(\frac{0.066\%}{E}\right)^2 + \left(\frac{0.81\%}{\sqrt[4]{E}}\right)^2 + (1.34\%)^2},$$

where E is the energy in GeV. For instance it means $\sigma_E/E \approx 2\%$ at 100 MeV and $\sigma_E/E \approx 1.4\%$ at 4 GeV. In Belle the angular resolution of ECL is $\sigma_\theta \approx 13$ mrad at low energy and $\sigma_\theta \approx 3$ mrad at high energies, while the π^0 mass resolution is 4.5 MeV/ c^2 . Despite the higher background level, because of the new electronics, the performance are expected to be similar in Belle II.

2.7 Superconducting magnet

A superconducting coil produces a 1.5 T homogeneous magnetic field B parallel to the beam direction. The coil is made of NbTi/Cu, and the internal volume is a cylinder of a diameter of 3.4 m and a length of 4.4 m. It operates with a 4400 A current and a liquid helium cryogenic system. The iron structure of the KLM provides the return yoke of the magnetic field, therefore in the region of KLM outside the coil the direction of B (i.e. the curvature of the tracks) is inverted.

The magnetic field has been mapped with commercial Hall sensors with a precision of 0.1%. The inhomogeneities of the field are due mainly to edge effects and to the presence of final focus system magnets of SuperKEKB.

2.8 K_L and Muon Detector (KLM)

The KLM is located outside the superconducting coil, and it is composed of alternating iron plates and active material detectors. The barrel region covers the polar angle range from $\theta = 45^\circ$ to $\theta = 125^\circ$, and the endcaps extend the range from $\theta = 20^\circ$ to $\theta = 155^\circ$. In the barrel region there are 15 detector layers and iron plates, while in the forward endcap are present 14 detector layers and iron plates and in the backward endcap there are 12 detector layers and iron plates.

The iron plates are 4.7 cm thick each and serve as the magnetic flux return for the superconducting solenoid and providing 3.9 interaction lengths λ_0 in addition to the $0.8\lambda_0$ of the ECL, in which K_L can shower hadronically.

The task of the KLM detector is to identify the muon tracks by measuring their penetration depth in the iron and to reconstruct neutral long-lived kaons with the use of the combined information of ECL and the hadronic KLM showers.

The outermost barrel detector layers of KLM are Resistive Plate Chambers (RPC): a proportional gas chamber used in streamer mode with a dielectric plate between the electrodes to prevent the propagation of sparks and so increase the spatial resolution. The signal is read by metallic strips on one side of the chamber. Each KLM module is made of two coupled RPC, with independent power supply and orthogonal strips configuration.

Because the RPCs have a too long dead time to sustain the background rate expected in some regions of the detector, in the endcaps region and in the two innermost barrel layers of the KLM, the RPCs have been substituted with two orthogonal layers of scintillator strips coupled with silicon photomultiplier (SiPM).

The muons are identified starting from CDC tracks: each track is extrapolated to KLM region with a μ mass hypothesis, and if a KLM hit is present close to the extrapolation region it is assigned to that track. Then a predicted pattern is defined as the sequence of extrapolated hits, taking care of the interaction between the particle and the material, and an actual range is defined as the sequence of hits assigned to the extrapolated track. The difference between the predicted and actual patterns and the quality of the extrapolations are finally used in a likelihood ratio to test the μ hypothesis.

The muon detection efficiency plateaus is about 90% above 1 GeV/ c , with a hadron fake rate of about 1.3% due to pions that decay in flight in softer muons.

To reconstruct K_L , all the KLM hits within a 5° opening angle cone from IP are clustered. If the remaining neutral KLM clusters are aligned within a cone of 15° with an ECL cluster the two showers are associated. The information of the KLM cluster, the associated ECL clusters and the closest track are then passed as inputs to a Boosted Decision Tree (BDT) to determine the probability that the given KLM cluster is originated by a K_L .

The K_L detection efficiency rises linearly from 0 at 0 GeV/ c to a 80% plateau at 3 GeV/ c . The angular resolution is about 3° for KLM-only candidates. The scintillator strips coupled to the SiPMs offer an excellent time resolution of $\sigma_t \approx 0.7$ ns, that allows to measure also the time of flight of K_L .

2.9 Trigger

The bunch crossing frequency of SuperKEKB is about 250 MHz². Since the bunch crossing time is much faster than the detectors signal decay time for all practical purposes the beam can be considered continuous. Anyway, at full luminosity, the expected event rate is about 50 kHz, and over than 90% of these events are Bhabha scattering or $e^+e^- \rightarrow \gamma\gamma$.

A trigger system is therefore required to select events from beam background and identify interesting ones. Despite $B\bar{B}$ events are characterized by a higher charged track multiplicity with respect to others events, this variable can not be used in the trigger because τ and low multiplicity events would be discarded too. The required trigger must have instead an efficiency of about 100% for $B\bar{B}$ events and a high efficiency for τ and low multiplicity events too. Some efficiency degradations are allowed to suppress the Bhabha and $\gamma\gamma$ events. The trigger rate must stay below 30 kHz, the maximum acquisition frequency of DAQ, and the trigger must provide time information with a precision under 10 ns to exploit the potential of the Belle II sub-detectors. To cope with the high background and to the several physics scenarios the trigger system must be robust and flexible.

The Belle II trigger is subdivided in two main stages: a hardware or Level 1 trigger (L1) and a software or High Level Trigger (HLT). The first one removes most of the background events with the use of raw information from the faster sub-detectors, the second trigger refine the selection with a more exhaustive analysis.

2.9.1 Level 1 trigger (L1)

The L1 trigger analyse the signals from detectors with a FPGA structure that provides a configurable system (programmable devices). The L1 trigger uses various signal from sub-detectors at low resolution and implements multiple trigger lines. The main sub-detectors that contribute to L1 trigger are CDC and ECL, although TOP and KLM are also used. A Global Reconstruction Logic combines the information of various sub-detector to obtain the total trigger logic.

²The SuperKEKB radio-frequency is about 500 MHz, but currently one every two bunch is not filled, resulting in an effective bunch crossing time of 4 ns

The CDC provide provide two-dimensional and three-dimensional tracking information. The z -position of the main vertex of the events is a strong discriminant for background events (with vertices far away from the IP). The FPGA takes about $1 \mu\text{s}$ to reconstruct the z position of the vertex. The ECL provides a trigger signals mainly based on the total energy released in the calorimeter and on the number of the isolated shower that use the 3D clustering techniques. With this methods the L1 trigger is able to reject most of Bhabha and $\gamma\gamma$ backgrounds without a significant degradation of the efficiency for low multiplicity events. The L1 trigger is also able to identify Bhabha and $\gamma\gamma$ events to monitor online the luminosity of SuperKEKB.

The latency of the trigger is about $5 \mu\text{s}$ and the maximum trigger rate is 30 kHz as required, with an efficiency over 99.9% for $B\bar{B}$ and continuum events.

2.9.2 High Level Trigger (HLT)

The goal of the HLT is to reduce the 30 kHz event rate from the L1 trigger to a maximum storable rate of 10 kHz.

The HLT uses the full information of all sub-detectors except the PXD and performs a fast reconstruction: the events are completely reconstructed with the same software used in the offline analysis (except the PXD information). Then the trigger applies physics requirement to the reconstructed events and reduces to 10 kHz the event rate. It is important to note that during the Phase 2 run, the HLT was not turned on and no data reduction was thus applied.

After the HLT reduction, the tracks reconstructed with the SVD and the CDC in the fast reconstruction are extrapolated to the PXD layers and the ROI are evaluated, then the pixels inside the defined regions are read. In conclusion, the full events are build combining the fast reconstruction events with the PXD data before the definitive storage. Before the fast reconstruction and the ROI extrapolation, the full PXD data are stored inside a pipeline, which receives in input the PXD data from the events selected by L1 trigger. The length of this pipeline defines the latency constraint of HLT. The current latency of the HLT is some seconds, under the pipeline constraints.

Chapter 3

Analysis overview

In this chapter we give a brief overview of the analysis strategy. The details, not fundamental for the understanding of this overview, will be clarified in the next chapters.

3.1 Analysis overview

In this work we present a search for an invisibly decaying Z' dark boson in $e^+e^- \rightarrow \mu^+\mu^- +$ missing energy and in $e^+e^- \rightarrow e^\pm\mu^\mp +$ missing energy final states using the data collected in 2018 by the Belle II experiment. In the following chapters, the Z' produced in association with a $\mu^+\mu^-$ pair (as predicted by the $L_\mu - L_\tau$ model) is referred to as “standard Z' ”, while the Z' produced with a $e^\pm\mu^\mp$ pair is denoted as “LFV Z' ”.

The goal of the standard Z' analysis is to look for a narrow peak in the mass spectrum of the system recoiling against a $\mu^+\mu^-$ pair (invisible Z' signature). The four-momentum p_{rec} of the recoiling system is defined as:

$$p_{\text{rec}} = p_{e^+} + p_{e^-} - p_{\mu^+} - p_{\mu^-} ,$$

where p_{e^+} and p_{e^-} are the four-momenta of the colliding positrons and electrons and p_{μ^+} and p_{μ^-} are the four-momenta of the final state muons. For signal events, the four-momentum of the recoiling system coincides with the four-momentum of the Z' boson, so the invariant mass of the recoiling system peaks at the value of the Z' mass. In the following, the invariant mass of the recoiling system¹ is simply referred as “recoil mass” and denoted by M_{rec} , the mass of the Z' boson is denoted by $M_{Z'}$ and the $\mu^+\mu^-$ pair is called “dimuon”.

We expect as main backgrounds all the SM processes which give final states with a $\mu^+\mu^-$ pair and missing energy, namely:

- $e^+e^- \rightarrow \mu^+\mu^-(\gamma)^2$ with one or more photons lost due to inefficiency or acceptance;
- $e^+e^- \rightarrow \tau^+\tau^-(\gamma)$ with $\tau \rightarrow \mu\bar{\nu}_\mu\nu_\tau$ or $\tau \rightarrow \pi\nu_\tau$ (due to a non optimal particle identification);

¹It is important to note that the invariant mass squared of the recoiling system M_{rec}^2 can be negative due to the detector resolution. If M_{rec}^2 is negative, then invariant mass of the recoiling system is defined as $-\sqrt{|M_{\text{rec}}^2|}$ to keep records of the sign.

²Here and in the following, the notation (γ) denotes radiative events, in which photons in the final state can be produced via radiative effects.

- $e^+e^- \rightarrow e^+e^-\mu^+\mu^-$ with electrons and positrons usually produced outside the detector acceptance.

We select events with two opposite-charged tracks identified as muons and no reconstructed photons above a minimum energy, especially in the direction opposite to the dimuon momentum. We also require the transverse momentum of the dimuon system to be above a given threshold, as this selection is very effective against $\mu^+\mu^-(\gamma)$ and $e^+e^-\mu^+\mu^-$ backgrounds. We then perform an additional selection, referred as “ τ suppression”, to further suppress the $\tau^+\tau^-(\gamma)$ background, which is found to be dominant for most of the mass range. After having applied all the previous selections, we evaluate the signal and the background efficiency from Monte Carlo (MC) simulations as a function of the recoil mass.

Since we opted for a blind analysis³, we optimize our selections using only simulated samples and control samples, rather than looking at collision data.

We check the MC predictions with an extensive use of control samples, from which we infer correction factors and related systematic uncertainties to both the background and the signal efficiency.

After the permission from the Belle II collaboration to look at the collisions data (unblinding procedure), we compute 90% confidence level (CL) upper limits to the Z' production cross section as a function of the recoil mass by applying a Bayesian counting technique.

As for the LFV Z' the same considerations hold (with the obvious change of the particle identification request which requires an electron paired to an opposite-charged muon). Due to the non-availability of a robust signal generator, the same selections as in the standard Z' case are applied and 90% CL upper limits are interpreted in terms of efficiency times cross section.

³A blind analysis is a measurement which is optimized without looking at the answer. Blind analyses are the optimal way to reduce or eliminate experimenter’s bias, the unintended biasing of a result in a particular direction.

Chapter 4

Data sets and event selection

In this chapter we give a description of the data sets we used to perform the analysis. Moreover, we describe the selections applied to select in our data sets the standard and LFV Z' candidates that will undergo through further steps of the analysis flow. We apply two levels of selections: the first, a loose selection is described in Section 4.2, and it is applied directly on the Belle II data sets in order to reduce the size of the analyzed samples; the second selection (described in the subsequent sections), is tighter and it is optimized to discriminate the signal candidates from the background.

It is important to note that, due to the asymmetric energies and acollinear orbits of the electron and positron beams, the coordinate system of the laboratory (LAB) frame is significantly different from that of the CM frame. In particular, in the laboratory frame the z axis is along the bisector of the angle between the direction of the electron beam and the reverse direction of the positron beam, while in the CM frame the z axis is along the direction of the electron beam. Specifically, the z axis in the CM frame points to the same direction as the unit vector $(0.1505, 0, 0.9886)$ in the LAB frame.

4.1 Used data sets

All the results presented in this work are based on the data collected by Belle II during the 2018 commissioning run (from April to July), referred as Phase 2 data set. As already mentioned in Section 2.1, during the Phase 2 run the accelerator luminosity was lower than the design one and the VXD was not fully installed.

We analyzed all the Phase 2 runs, corresponding to an integrated luminosity $\int L dt = 479.8 \text{ pb}^{-1}$ measured with Bhabha events ($\int L dt = 494.9 \text{ pb}^{-1}$ with $\gamma\gamma$ events)¹. Because of the trigger configuration and the data quality selections used for the analysis, the effective available integrated luminosity is reduced to 276 pb^{-1} (see Section 4.3.1 and Section 7.1.1).

We used MC samples with Phase 2 geometry and beam background for studies related to the standard Z' events. We generated 16 samples of 20000 events for Z' masses from $0.5 \text{ GeV}/c^2$ up to $8 \text{ GeV}/c^2$, with a mass step size of $0.5 \text{ GeV}/c^2$. Such samples were produced by using the `release-02-00-01` release of the Belle II Analysis Software Framework (`basf2`) software [26] and the `MadGraph` generator [27]. Assuming the $L_\mu - L_\tau$ model, the predicted

¹The luminosity quoted here refers to a previous reprocessed data set then the final one, used also in [11]

cross section for the signal process is quadratic in the coupling constant g' . The numerical values of the simulated signal cross section as a function of $M_{Z'}$, assuming a coupling constant of $g' = 0.01$, are shown in Figure 4.1; it should be noticed that the cross section vanishes approaching the center-of-mass (CM) energy $\sqrt{s} \approx 10.58$ GeV.

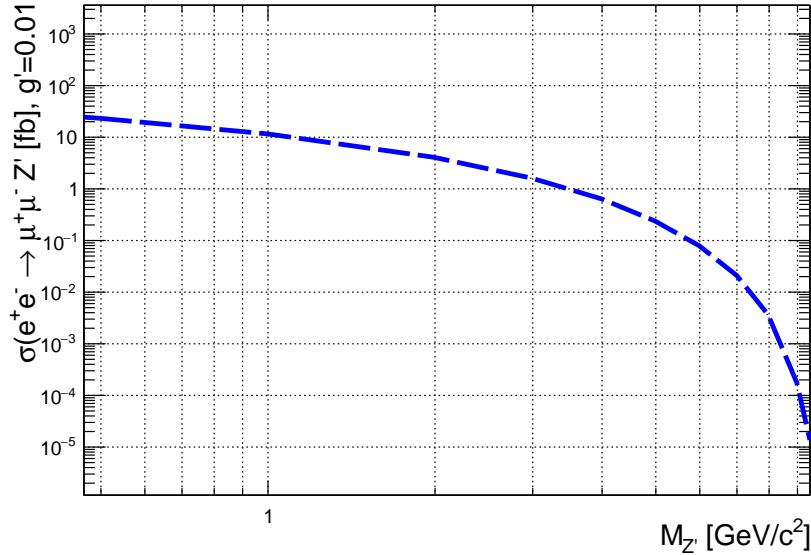


Figure 4.1: Numerical cross section values for standard Z' events obtained with MadGraph generator. For Z' masses approaching the CM energy \sqrt{s} , the cross section vanishes, limiting our sensitivity for $M_{Z'} > 8$ GeV/ c^2 .

We used MC samples with Phase 2 geometry and beam background listed in Table 4.1 for background studies. The number of generated events, the equivalent integrated luminosity and the MC generator used for each sample are specified in the same table. Such samples are used for both standard and LFV Z' searches.

Table 4.1: Phase 2 MC samples used for background studies with the number of generated events N_{evts} , the equivalent integrated luminosity $\int Ldt$ and the MC generator used.

Process	N_{evts} [10^6]	$\int Ldt$ [fb^{-1}]	MC generator
$e^+e^- \rightarrow \mu^+\mu^-(\gamma)$	65	56.621	KKMC [28]
$e^+e^- \rightarrow \tau^+\tau^-(\gamma)$	36.8	40.044	KKMC [28] + TAUOLA [29]
$e^+e^- \rightarrow e^+e^-\mu^+\mu^-$	140	7.406	AAFH [30]
$e^+e^- \rightarrow \pi^+\pi^-\gamma$	210	1372.539	PHOKHARA [31]
$e^+e^- \rightarrow e^+e^-$	60	0.198	BabaYaga@NLO [32]
$e^+e^- \rightarrow e^+e^-e^+e^-$	260.6	6.562	AAFH [30]

The detector geometry and the interactions of the final state particles with the material are simulated using GEANT4 [33] and basf2.

4.2 Basic selections

4.2.1 Standard Z'

We reconstruct an event by requiring two opposite-charged tracks measured by the CDC and coming from the IP. In particular, we require that a track satisfies the following criteria, denoted as “cleaned tracks” selection in the following²:

- $|d_0| < 0.5$ cm;
- $|z_0| < 2.0$ cm;
- at least 1 hit in the CDC.

We identify the tracks as muons by applying a loose ECL-based selection. We require that the ECL cluster associated to the track has an energy lower than 0.75 GeV. We also require that the ratio between the energy of the associated ECL cluster and the momentum of the track is lower than 0.5. These two requirements are necessary in order to reject the electron candidates from our sample.

Since the KLM was still in a commissioning phase during the 2018 data taking, it wasn't possible to use it to further select the muon candidates and distinguish them from pions.

The selected tracks are then combined to form a dimuon candidate and the event is accepted only if the total number of cleaned tracks in the event is equal to 2 or 3.

Additionally, we reconstruct the so-called Rest Of Event (ROE) with the respect to our dimuon candidate. In Belle II, the ROE with respect to a given particle candidate is defined as the set of tracks and ECL clusters that are not used to reconstruct the particle. In our case, the ROE is defined as the set of tracks and ECL clusters not associated to the muons used to build the dimuon candidate. In order to clean the ROE from the beam background, a track in the ROE is required to have at least 1 hit in the CDC, while an ECL cluster in the ROE is required to be clusterized assuming a photon hypothesis and to have an energy larger than 100 MeV.

Then, we reconstruct the recoil system against the dimuon candidate, being the Z' candidate for that event.

As last step, we also save the kinematic information of the photon closest to the recoil momentum, the kinematic information of the most energetic photon in the event and the information of the most plausible π^0 candidate in the event.

4.2.2 LFV Z'

For LFV Z' we apply a similar selection as the one presented in the previous subsection.

The same event reconstruction is applied as far as the cleaned tracks selection is concerned.

²Given the Point Of Closest Approach (POCA) of a track to the IP, we define d_0 the transverse projection, in the $r - \phi$ plane, of the POCA, while we define z_0 the longitudinal projection of the POCA. In Belle II, the quantity d_0 is signed, and its sign is used to distinguish the positive-charged tracks from the negative-charged ones.

For the PID, we require one track to be identified as a muon, as in the standard Z' case, and a second track to be identified as an electron according to the following ECL-based selection: the ECL cluster associated to the track must have an energy larger than 1 GeV; the ratio between the energy of the associated ECL cluster and the momentum of the track must be within 0.7 and 1.3.

Then the electron-muon candidate is obtained by combining the electron and the muon tracks (with opposite charge) and the reconstruction flow continues exactly as for the standard Z' case, with the ROE and the recoil reconstruction.

In both cases, the selected candidates undergo a further and tighter selection as described in the following sections.

4.3 Further selections

4.3.1 Standard Z'

To further reject the background candidates, we apply a tighter selection. Each reconstructed candidate has to satisfy the following criteria:

1. the number of cleaned tracks must be exactly 2 and the opening angle between the two muon candidates in the transverse $r - \phi$ plane ($\Delta\phi$) must exceed 90° , in order to emulate the functionality of the low-multiplicity CDC trigger (trigger logic `ffo`³) that is not properly simulated in MC; we also require $\Delta\phi < 172^\circ$, in order to follow the prescriptions in [34], for which the systematic effects are evaluated;
2. the polar angle of the muons θ_μ must be within a restricted barrel ECL angular acceptance for a good cluster-matching efficiency and for a good control of the systematics ($\theta_\mu \in [37^\circ, 120^\circ]$);
3. the recoil momentum must point to the barrel ECL acceptance region ($\theta_{\text{rec}} \in [33^\circ, 128^\circ]$) in order to exclude inefficient regions where photons can pass undetected and mimic the signature of an invisibly decaying Z' ; this selection is applied only for recoil masses below $3 \text{ GeV}/c^2$, as for larger masses the photon hypothesis is very unlikely;
4. a tighter ECL-based PID selection: the ECL cluster associated to the track must have an energy within 0.15 GeV and 0.4 GeV; the ratio between the energy of the associated ECL cluster and the momentum of the track must be lower than 0.4^4 ;
5. all events with a reconstructed photon within a 15° cone around the recoil momentum direction in the CM frame are discarded;
6. a) the ROE must have no additional charged tracks measured by the CDC;
b) as most of the background comes from τ pair production (see below) and π^0 are

³The `ffo` trigger logic selects events with at least two tracks with $\Delta\phi$ larger than 90° and with energy depositions in ECL incompatible with a Bhabha final state.

⁴Since the KLM is not involved, in this analysis, to identify the muons, we expect to have a large number of pions misidentified as muons.

among the most common τ decay products, we setup a π^0 veto; all the photons in the ROE having an energy larger than 75 MeV are used to reconstruct the decay $\pi^0 \rightarrow \gamma\gamma$, then we select only 1 π^0 candidate per event by choosing the one with the invariant mass closest to the nominal π^0 mass; the event is finally discarded if the mass of the candidate is in the range $125 < M_{\pi^0} < 145$ MeV/ c^2 and the total energy of the ECL clusters in the ROE (extra energy in the ECL) exceeds 0.2 GeV (see Figure 4.2);

c) the extra energy in the ECL is anyway required to be less than 0.4 GeV.

7. the transverse momentum of the dimuon candidate in the LAB frame satisfies $p_{\mu\mu}^T > p_{\text{cut}}^T$, where p_{cut}^T is a linearly decreasing function with the recoil mass and its value is 1.03 GeV/ c at a recoil mass of 0.5 GeV/ c^2 and 0.43 GeV/ c at a recoil mass of 9 GeV/ c^2 ; this cut is anyway superseded by other selections described here below.

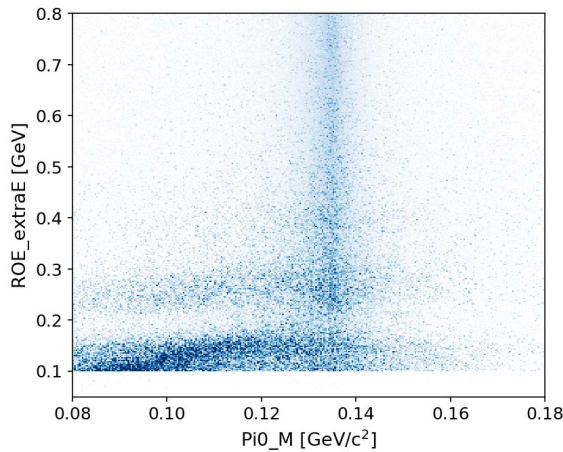


Figure 4.2: Extra energy in the ECL as a function of the candidate π^0 mass in background simulated events.

The signal efficiency for each generated Z' mass hypothesis, computed as the ratio between selected and generated events and also multiplied by the measured trigger efficiency (79%), as a function of the analysis cuts listed above, is shown in Figure 4.3.

The number of surviving background events after the analysis cut number (listed above) and the background spectrum achieved after all the described selections as a function of the recoil mass are shown in Figure 4.4. All the backgrounds are normalized to an integrated luminosity of 276 pb $^{-1}$, and then scaled by the 79% trigger efficiency factor.

τ pair events ($\tau^+\tau^-(\gamma)$) are the main source of background for a large part of the available phase space, while radiative dimuon events ($\mu^+\mu^-(\gamma)$) start to be relevant at low recoil masses and four lepton final state events ($e^+e^-\mu^+\mu^-$) dominate above 7 GeV/ c^2 . The other sources of background are found to be negligible.

4.3.2 LFV Z'

As already mentioned in Section 3.1, for the LFV Z' we applied almost the same selections as in the standard Z' . Only the selections 1. and 4. listed in Section 4.3.1 are changed to:

- 1 the number of cleaned tracks must be exactly 2 and CL cluster associated to the

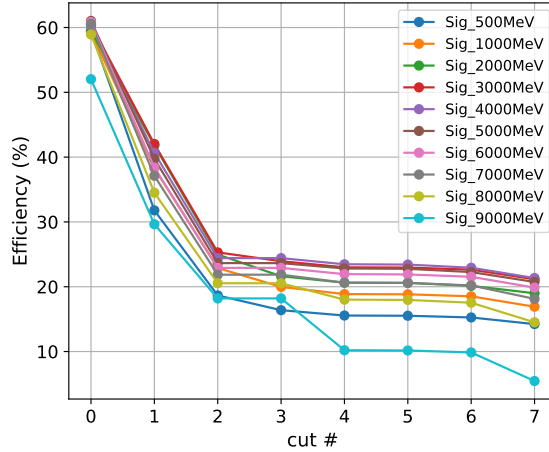


Figure 4.3: Signal efficiencies for different Z' masses as a function of the cut number. The efficiencies are multiplied by the measured trigger efficiency (79%). Different colors refer to different Z' masses.

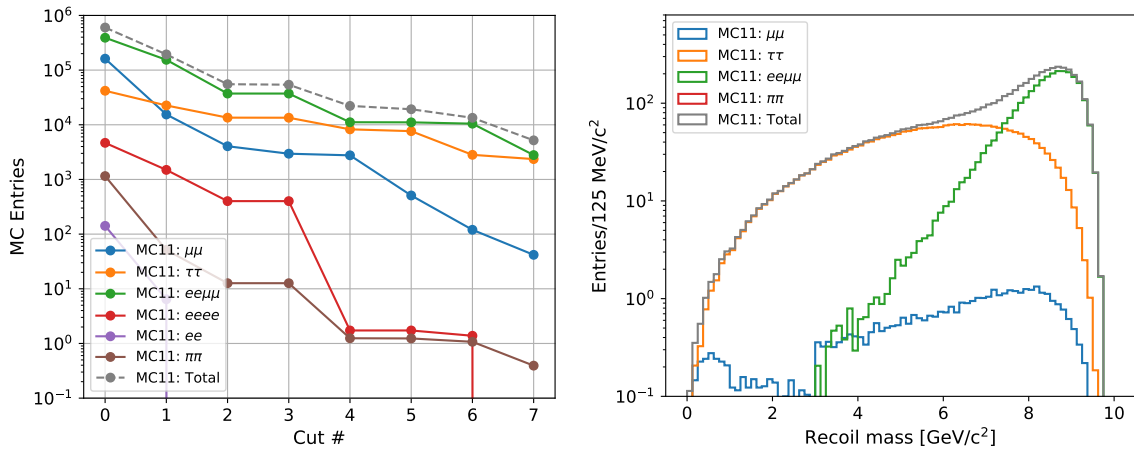


Figure 4.4: Surviving background events as a function of the cut number (left) and recoil mass (right). Background samples are normalized to an integrated luminosity of 276 pb^{-1} and scaled by a trigger efficiency of 79%.

electron track is required to exceed 1.5 GeV, in order to emulate the functionality of the ECL trigger (trigger logic `hie`⁵, whose measured efficiency is 96%) [34];

4 a tighter ECL-based selection also for the electron candidate: the ratio between the energy of the associated ECL cluster and the momentum of the track must be within 0.8 and 1.2.

All the other selections are left unchanged, with the obvious replacement of the subscript “ μ ” with “ e ” where appropriate ($\theta_e, p_{e\mu}^T$).

We show in Figure 4.5 the number of background events after the analysis cut number and the background spectrum achieved after all the described selections, as a function of the recoil mass. All the background sources are normalized to the same integrated luminosity as in the standard Z' analysis (276 pb^{-1}), but with a trigger efficiency of 96%.

⁵The `hie` trigger logic selects events with a total energy deposition in the barrel and part of the endcap ECL larger than approximately 1 GeV and with topologies incompatible with a Bhabha final state.

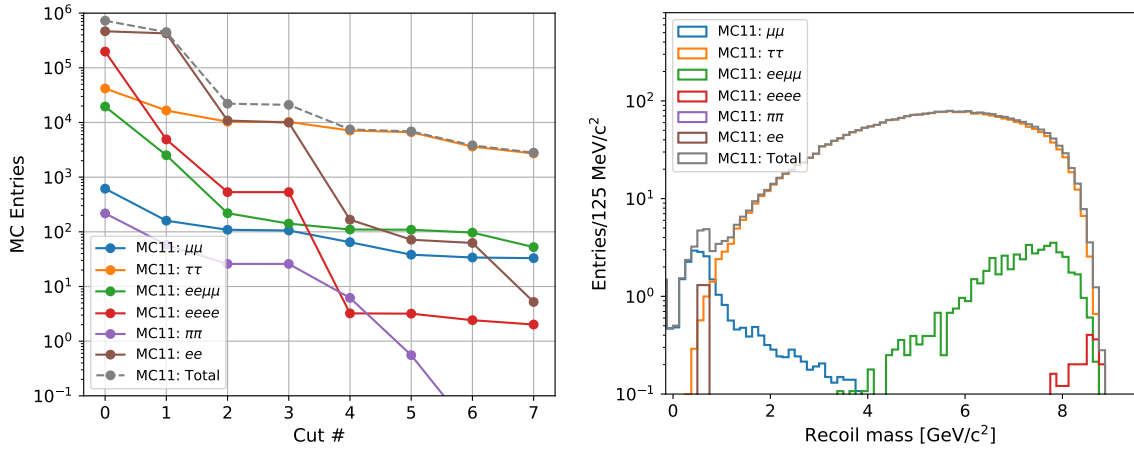


Figure 4.5: Surviving background events as a function of the cut number (left) and recoil mass (right). Background samples are normalized to an integrated luminosity of 276 pb^{-1} and scaled by a trigger efficiency of 96%.

τ pair events ($\tau^+\tau^-(\gamma)$) are largely the main source of background for most of the available phase space, with the exception of a small region at low recoil masses, where radiative dimuon events ($\mu^+\mu^-(\gamma)$) give some contribution.

Since we do not have any reliable LFV Z' signal simulation, no signal efficiency due to these selections is thus quoted.

Chapter 5

Recoil mass distribution and resolution

In order to search for the standard Z' and in case put upper limits on the production cross section we use a counting technique: the number of events in windows of the recoil mass are compared with the background expectations. In this chapter we show the studies performed on the signal standard Z' samples in order to determine, first, the recoil mass resolution as a function of the recoil mass and, furthermore, the optimal widths of the recoil mass windows.

5.1 Recoil mass distribution

To find the resolution of the peak for various mass points, we perform an unbinned maximum likelihood fit (using `Roofit` [35]) of the recoil mass distributions of the signal samples generated for different Z' masses.

We use a Crystal Ball (CB) [36] function to describe the rightmost tail of the recoil mass distribution which is due to the effect of the ISR. A CB function, with parameters μ (mean), σ (width), α and n , can be written as:

$$CB(x; \mu, \sigma, \alpha, n) = N \cdot \begin{cases} e^{-\frac{(x-\mu)^2}{2\sigma^2}} & \text{for } \frac{x-\mu}{\sigma} > -\alpha \\ A \cdot \left(B - \frac{x-\mu}{\sigma}\right)^{-n} & \text{for } \frac{x-\mu}{\sigma} \leq -\alpha \end{cases}$$
$$A(\alpha, n) = \left(\frac{n}{|\alpha|}\right)^n \cdot e^{-\frac{|\alpha|^2}{2}},$$
$$B(\alpha, n) = \frac{n}{|\alpha|} - |\alpha|,$$

where N is a normalization factor. Moreover, a Gaussian is added in order to fully describe the remaining part of the distribution. The resulting Probability Density Function (PDF) consists of five parameters, as we set the mean of both CB and Gaussian to a fixed value: σ_{CB} and σ_{Gauss} , being the width of the CB and the Gaussian respectively; α and n , being the remaining CB parameters; f , the CB fraction with respect to the normalized sum of both.

The recoil mass distribution for every generated signal sample as well as the corresponding

fitted PDF model distribution can be seen in Figure 5.1. As we observe negative values for the recoil mass in case of a mass hypothesis $M_{Z'} = 0.5$ GeV, we decide to plot M_{rec}^2 and perform the fit algorithm on this variable.

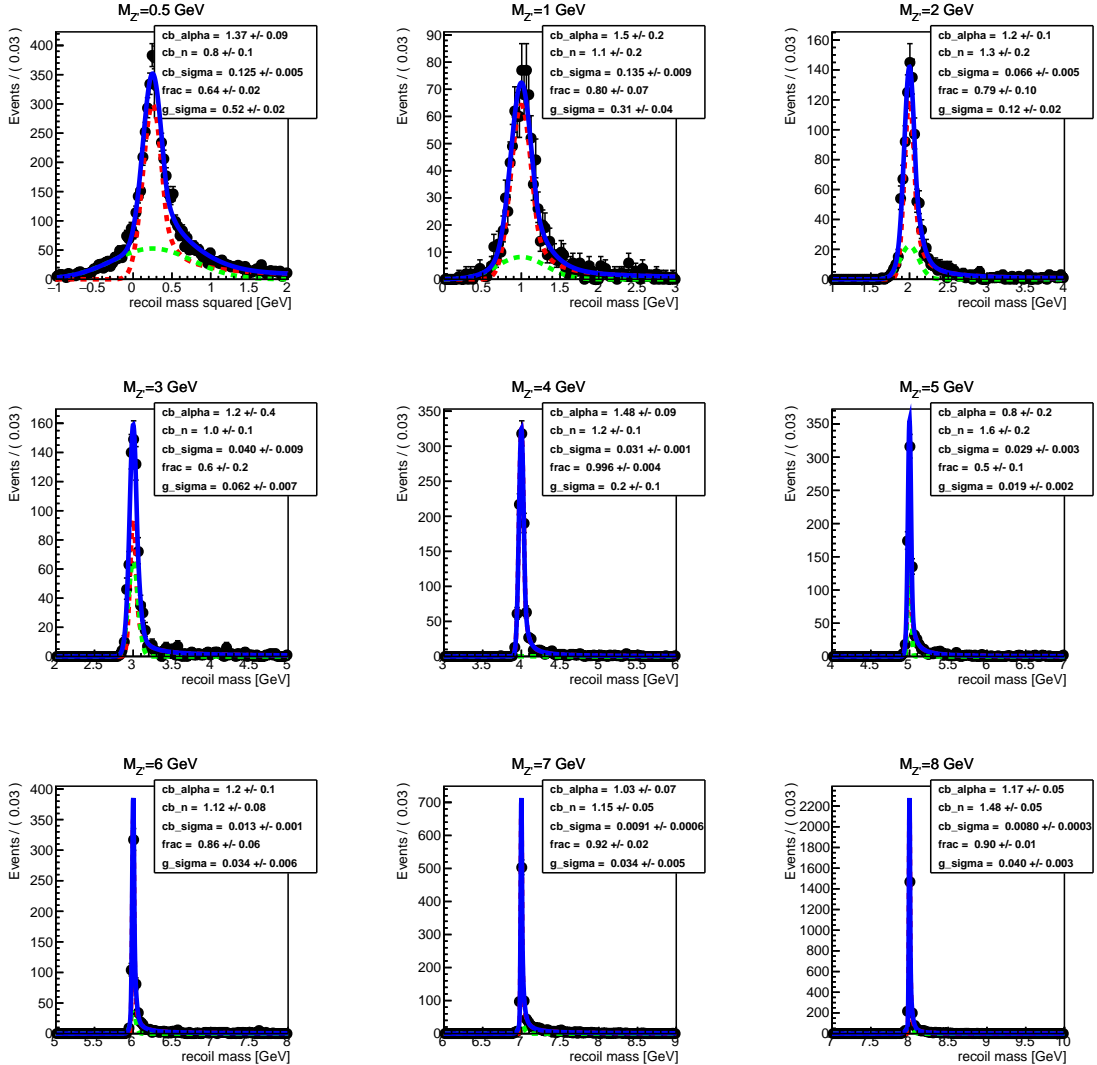


Figure 5.1: Recoil mass and fitted PDF model distribution (blue line) for some of the generated standard Z' samples. The contribution of the CB and the Gaussian is shown with a red and green dotted line respectively. The resulting fit parameters are shown in the top right corner of each graph.

In general we observe good fit results, concluding that the chosen PDF model is able to describe properly the recoil mass distribution.

In order to validate the fit, we performed a toy study with 1000 samples of 10000 events each. The events in each of the toy sample were generated according to the resulting PDF model parameters of the fit. We then looked at the parameter distributions of the toy samples. As example, the mean, error and pull distribution of σ_{CB} and σ_{Gauss} for $M_{Z'} = 5$ GeV are shown in Figure 5.2. The pull distributions are fitted with a Gaussian. Since the mean and the width of the fitted Gaussian agree, respectively, with 0 and 1 for both of the PDF parameters σ_{CB} and σ_{Gauss} , we were able to validate the fit algorithm and the chosen

PDF model.

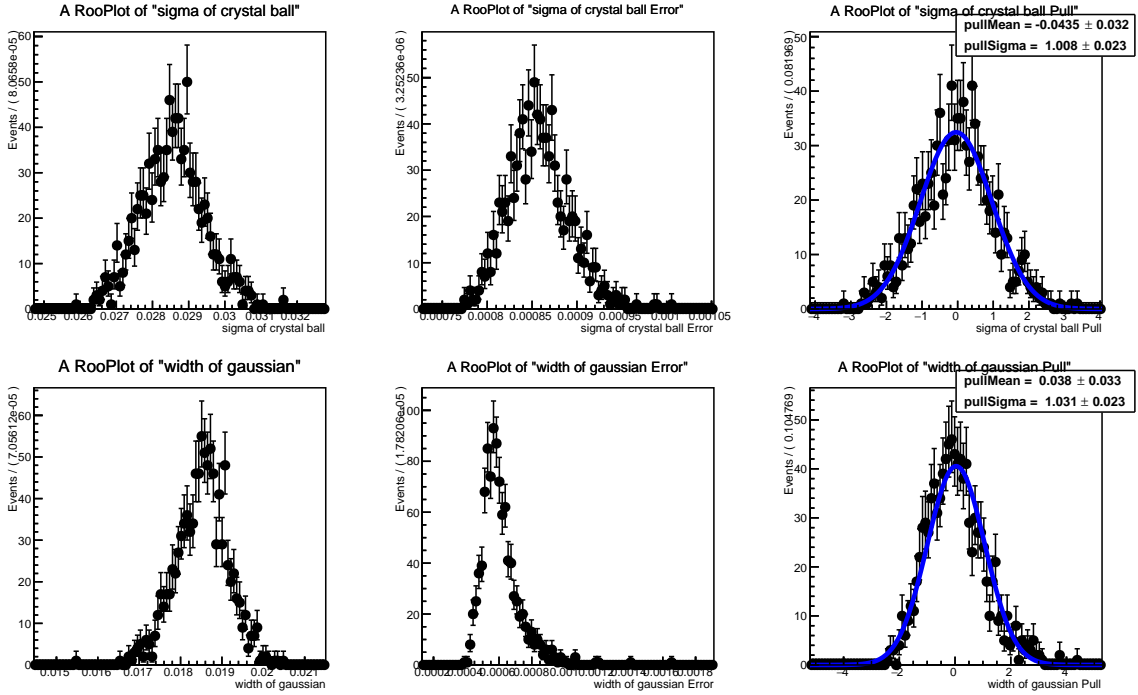


Figure 5.2: Validation plots of σ_{CB} (top) and σ_{Gauss} (bottom) for $M_{Z'} = 5$ GeV. The pull distribution (rightmost graph) for both parameters is fitted with a Gaussian (blue line). The fit results of the pull distribution are shown in the top right corner of the graph, and they agree with the hypothesis of a Gaussian distribution having mean $\mu = 0$ and width $\sigma = 1$.

We furthermore observe similar results for all the standard Z' generated mass points.

5.2 Recoil mass resolution

For the definition of the recoil mass windows, we need to calculate the width of each recoil mass distribution (corresponding to our recoil mass resolution). We define it as the weighted width σ_w of σ_{CB} and σ_{Gauss} , taking correctly into account the different contributions of CB and Gaussian in the chosen PDF. To do that we use the following equation:

$$\sigma_w = \sqrt{f \times \sigma_{\text{CB}}^2 + (1 - f) \times \sigma_{\text{Gauss}}^2}, \quad (5.1)$$

using for σ_{CB} , σ_{Gauss} and f the fit results shown in Figure 5.1. The resulting weighted widths for every generated Z' mass point are shown in Figure 5.3.

5.2.1 Validation using Phase 2 data

We checked on Phase 2 data the dimuon recoil mass resolution and then compared with the one from MC simulation, by selecting a clean sample of $\mu^+\mu^-\gamma$ events. In order to do that, the selections 1, 2, 3, 4, 6 described in Section 4.3.1 were applied on data and MC samples, while selection 5 was reversed, by requiring the presence of a photon around a 12° cone in the CM frame within the recoil momentum direction (the ROE in selection 6 is defined with

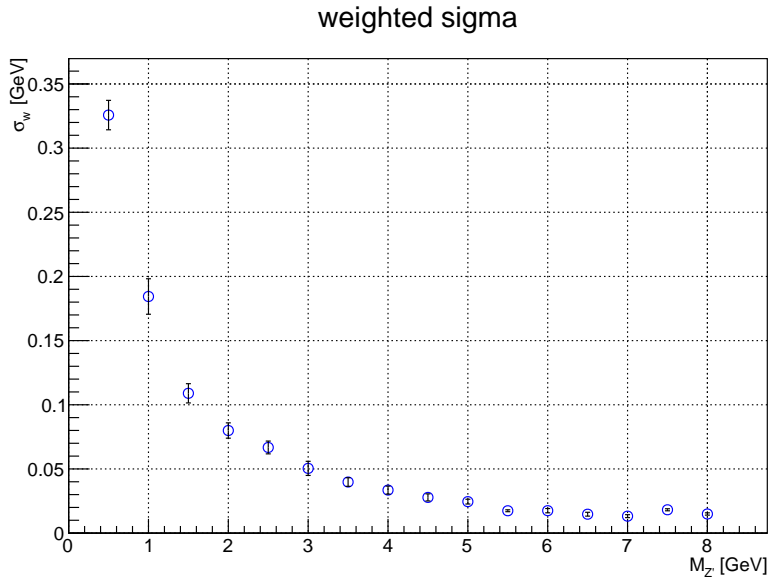


Figure 5.3: Width of each recoil mass distribution (as defined in Eq. 5.1) as a function of the mass of the generated Z' samples.

respect to the $\mu^+\mu^-\gamma$ system). In addition, we required that the sum of the energies of the two muons and of the photon lies between 10 and 12 GeV (to be compared with the sum of the beam energies of 11 GeV) and that there are no additional detected photons in the event with an energy larger than 100 MeV.

We weighted the bidimensional muon momentum distribution of $\mu^+\mu^-\gamma$ events in $0.5 \text{ GeV}/c \times 0.5 \text{ GeV}/c$ bins in both data and MC to reproduce analogous distributions for $\mu^+\mu^-Z'$ events at different Z' masses. The procedure works well only for low Z' masses, as, for larger masses, it is harder and harder to match the muon momentum distributions of $\mu\mu Z'$ with $\mu\mu\gamma$ ones, due to obvious kinematical reasons (see Figure 5.4).

The weighted recoil mass distributions are expected to be centered at zero: the difference in width between data and MC can be used as a correction factor to the measured recoil mass resolution. We fitted the recoil mass distributions with the sum of a CB and a Gaussian function.

Correction factors, defined as the ratio of the values of the weighted widths extracted from the fit to data (σ_w^{data}) and MC (σ_w^{MC}) recoil mass distributions are shown in Table 5.1. As they are smaller or compatible with 1, we conclude that the detector resolution is well described in our detector MC simulations (or we may neglect the differences when the correction factor is smaller than 1).

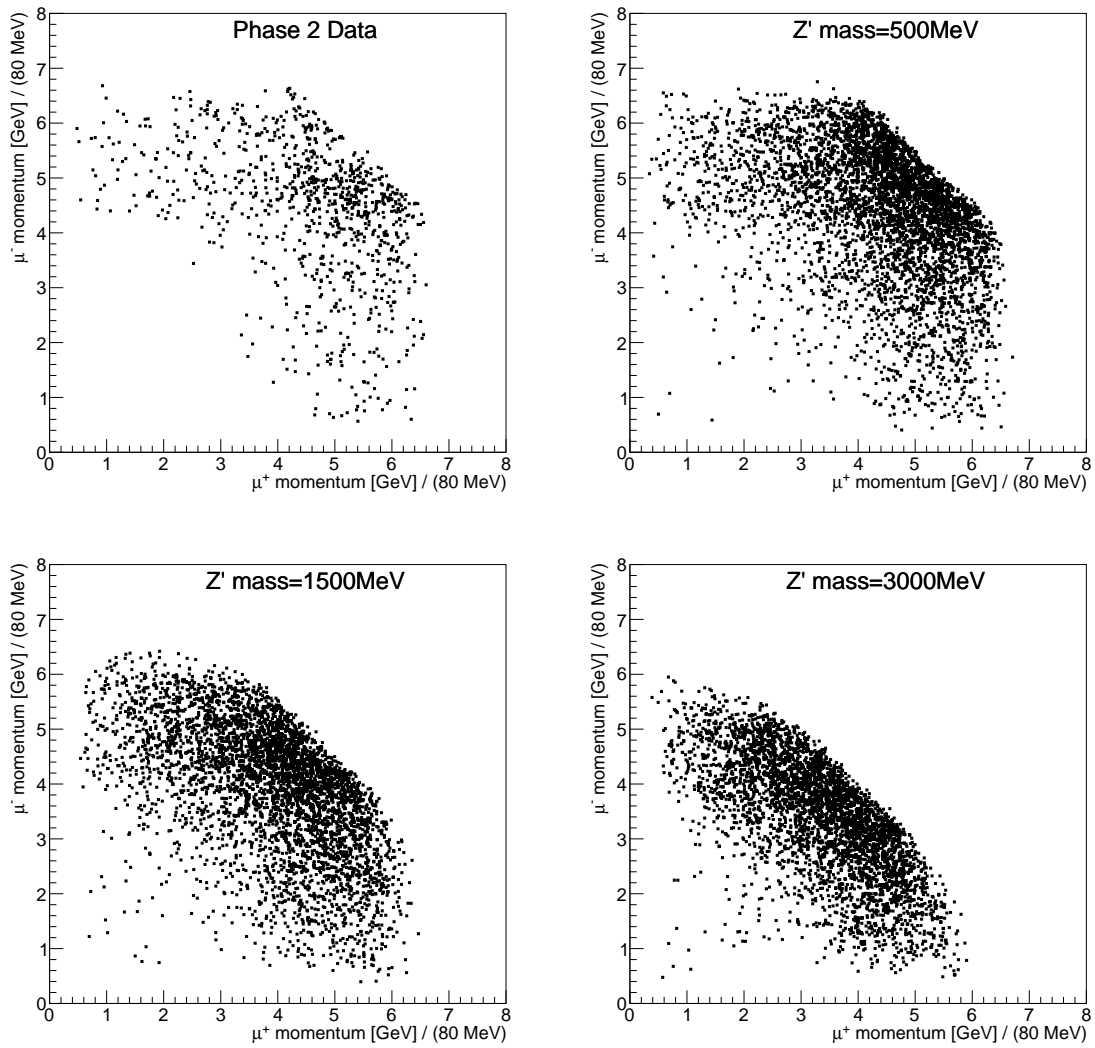


Figure 5.4: Distributions of muon momentum in Phase 2 data for $\mu^+\mu^-\gamma$ events (top left), and in MC samples for $\mu^-\mu^-Z'$ events for different Z' masses: 0.5 GeV/c^2 (top right), 1.5 GeV/c^2 (bottom left), 3.0 GeV/c^2 (bottom right). The binning used in this plots is different from the one used for the study.

Table 5.1: Correction factors, defined as the ratio between σ_w^{data} and σ_w^{MC} are given as a function of the Z' mass used to reweight the $\mu\mu\gamma$ sample.

$M_{Z'}$ [GeV/ c^2]	$\sigma_w^{\text{data}}/\sigma_w^{\text{MC}}$
0.5	0.883 ± 0.074
1.0	0.794 ± 0.084
1.5	0.938 ± 0.084
2.0	1.089 ± 0.105
2.5	1.048 ± 0.087
3.0	0.997 ± 0.081

Chapter 6

The τ suppression strategy and its optimization

For both the standard and LFV Z' we observe that the largest fraction of the background composition is due to τ pair events in most of the recoil mass spectrum. In this Chapter we discuss about the strategy, called “ τ suppression”, adopted in our analysis in order to heavily suppress this background source.

6.1 τ suppression and optimization for standard Z'

We studied several discriminating variables at the various recoil masses and, for each mass value, we considered only events within the corresponding mass window, defined as $\pm\sigma_w$ (see Section 5.2) around the generated mass value. More details are given in the following Section 6.3.

The guiding principle in discriminating signal from background was that the Z' production is a Final State Radiation (FSR) process from a muon leg (see Figure 1.4), while the invisible momentum in τ pair events, which can mimic the presence of a Z' , comes from the neutrinos from τ decays on both legs.

We found that the best variables to discriminate signal from background are the transverse component of the recoil momentum (the Z' momentum in the signal case) with respect to the maximum ($p_{rec}^{T,lmax}$) and minimum ($p_{rec}^{T,lmin}$) momentum muon directions and the transverse momentum of the dimuon pair ($p_{\mu\mu}^T$). All these variables are computed in the CM frame. We opted to avoid the usage of further variables and multivariate analysis at this very initial stage of the experiment life.

Bidimensional distributions of $p_{rec}^{T,lmax}$ versus $p_{rec}^{T,lmin}$ and distributions of $p_{\mu\mu}^T$ for three sample mass windows (centered at 2, 5 and 7 GeV/ c^2 respectively) are shown in Figure 6.1, 6.2, 6.3 for signal and background.

We searched for an optimal separating line (two parameters) in the $p_{rec}^{T,lmax} - p_{rec}^{T,lmin}$ plane and an optimal cut on the $p_{\mu\mu}^T$ distribution ($p_{\mu\mu}^T > p_{cut}^T$) by independently varying the three parameters (the separating line and the cut on $p_{\mu\mu}^T$) at the same time and by numerically looking for maximal values of the Punzi Figure of Merit (FOM_{Punzi}) [37] which takes into account the signal efficiency ϵ_{sig} , the number of surviving background events N_{bkg} and the

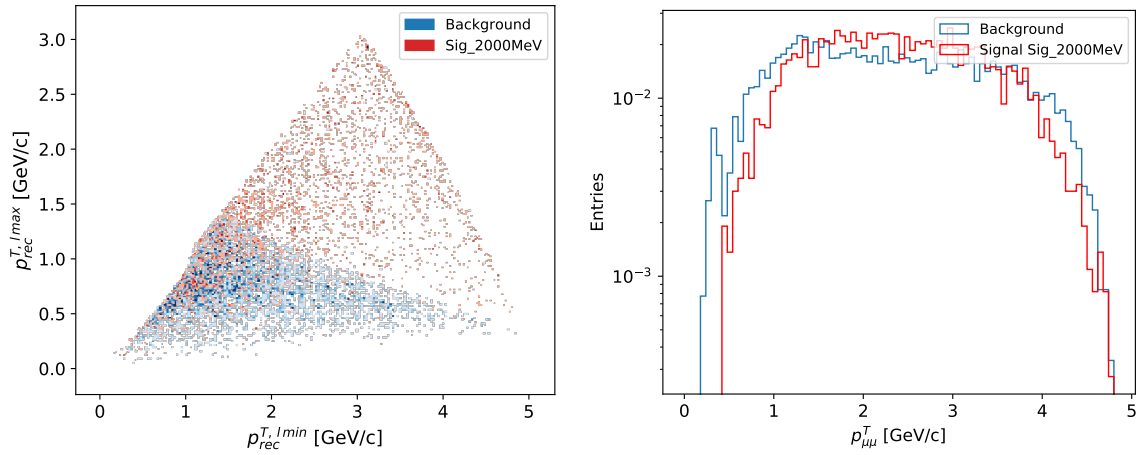


Figure 6.1: $p_{rec}^{T,max}$ vs. $p_{rec}^{T,min}$ (left) and $p_{\mu\mu}^T$ (right) distributions for $M_{Z'}=2$ GeV/c^2 signal (red) and for background (blue).

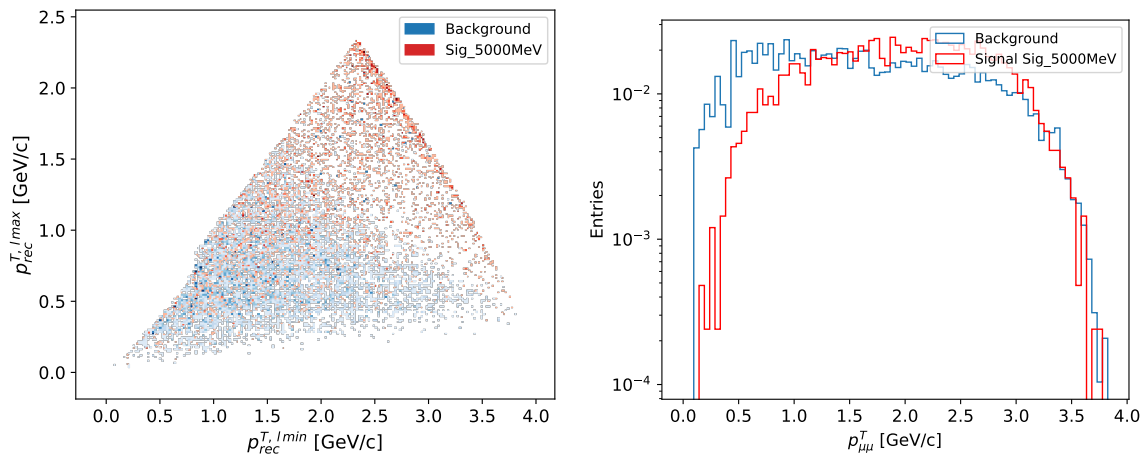


Figure 6.2: $p_{rec}^{T,max}$ vs. $p_{rec}^{T,min}$ (left) and $p_{\mu\mu}^T$ (right) distributions for $M_{Z'}=5$ GeV/c^2 signal (red) and for background (blue).

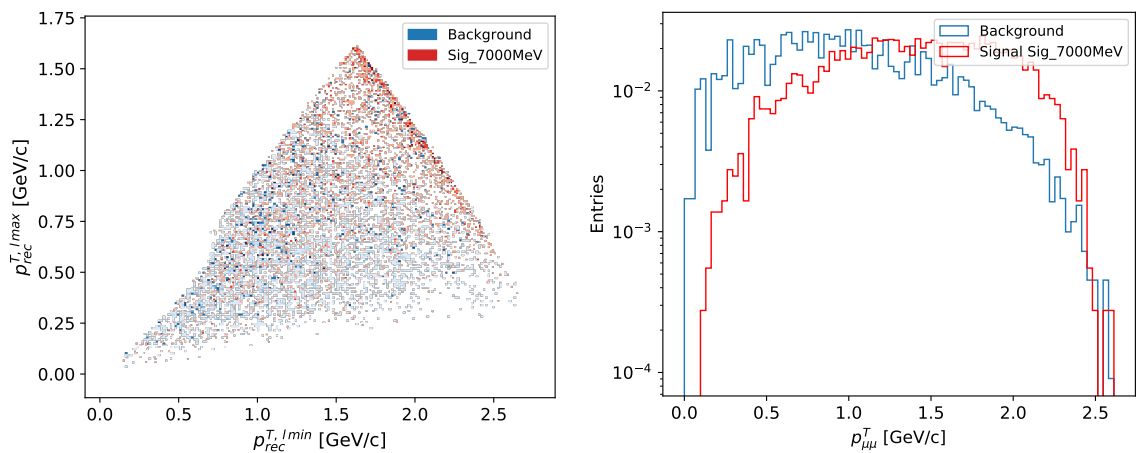


Figure 6.3: $p_{rec}^{T,max}$ vs. $p_{rec}^{T,min}$ (left) and $p_{\mu\mu}^T$ (right) distributions for $M_{Z'}=7$ GeV/c^2 signal (red) and for background (blue).

desired CL (in terms of number of sigmas a corresponding to two-sided Gaussian tests at

the given CL) for an exclusion:

$$\text{FOM}_{\text{Punzi}} = \frac{\epsilon_{\text{sig}}}{a/2 + \sqrt{N_{\text{bkg}}}} . \quad (6.1)$$

We chose a 90% CL, corresponding to $a = 1.64$.

For the 2, 5 and 7 GeV/ c^2 sample masses, we show in Figure 6.4, the bidimensional $p_{\text{rec}}^{T,lmax} - p_{\text{rec}}^{T,lmin}$ distributions after the optimal $p_{\mu\mu}^T$ cut, with the optimal separating line superimposed. We retain the events above the optimal line and discarded those below.

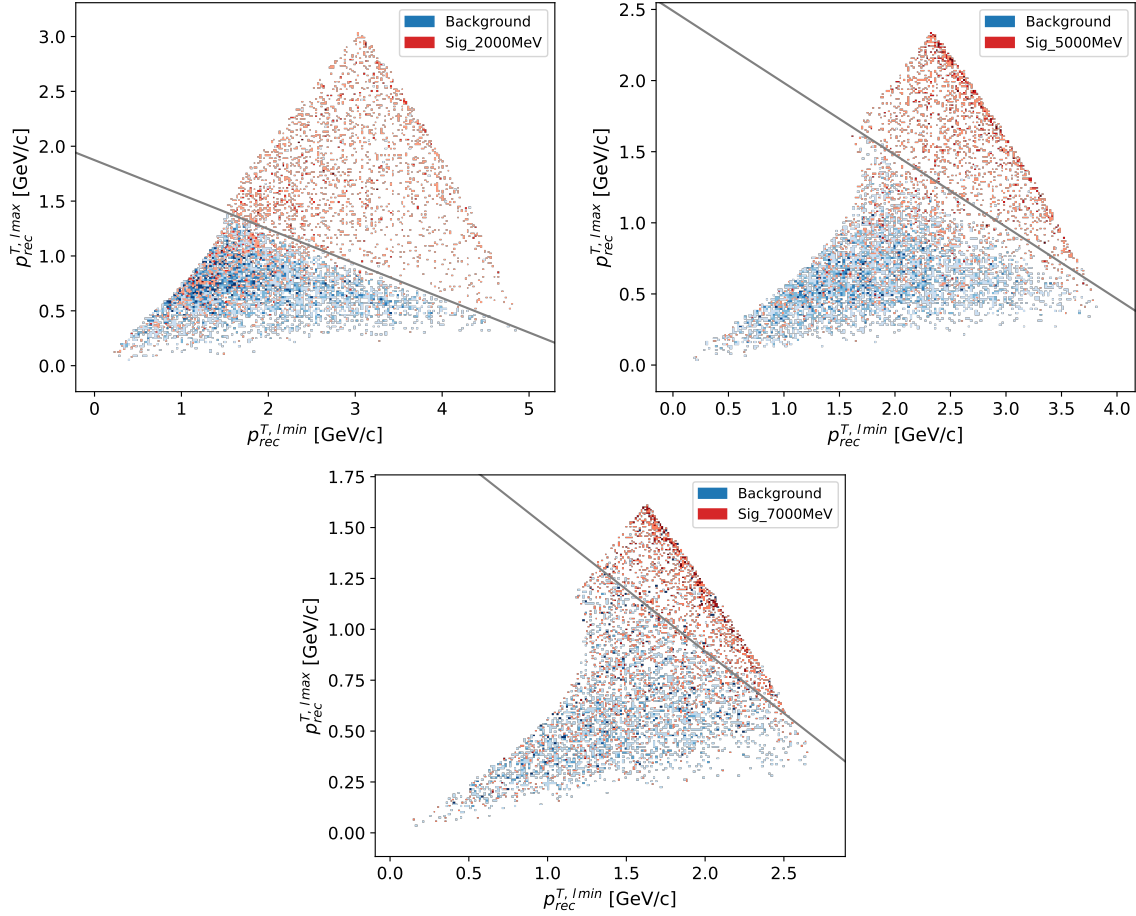


Figure 6.4: $p_{\text{rec}}^{T,lmax}$ vs. $p_{\text{rec}}^{T,lmin}$ distributions after the optimal $p_{\mu\mu}^T$ cut for $M_{Z'} = 2, 5, 7$ GeV/ c^2 signal (left, middle and right respectively, red) and for background (blue). The optimal separating line is superimposed.

The optimization was performed only for the recoil mass values corresponding to the generated signal samples (Section 4.1). In order to get values of these parameters for a generic recoil mass we fitted independently the two parameters of the optimal separating line and the values of the $p_{\mu\mu}^T$ cut (neglecting mutual correlations arising from the optimization procedure) using a linear spline technique as a function of the recoil mass. Figure 6.5 shows the $p_{\mu\mu}^T$ cuts determined by the optimization procedure, together with the interpolated values from the linear spline technique.

In Figure 6.6 we show the signal efficiency as a function of the recoil mass, while in Figure 6.7 we show the surviving background spectrum after the τ suppression procedure

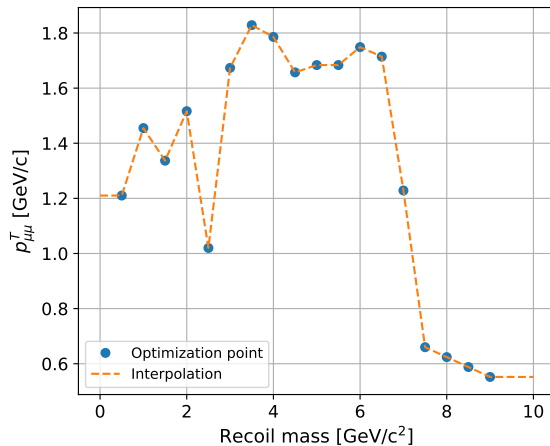


Figure 6.5: Optimal $p_{\mu\mu}^T$ cuts as a function of the recoil mass. The interpolated values (linear spline) are also shown.

and the background rejection factor achieved by the τ suppression procedure only, still as a function of the recoil mass. For masses above $7 \text{ GeV}/c^2$ signal and background overlaps heavily in the $p_{rec}^{T,max} - p_{rec}^{T,min}$ plane and the optimization procedure stops finding effective separating lines. This is clearly seen in Figures 6.6 and 6.7 with both signal efficiency and background suddenly increasing for recoil masses larger than $7 \text{ GeV}/c^2$. The loss of rejection power for masses above $7 \text{ GeV}/c^2$ is thus due to kinematics reasons related to the change of the dominant background source (now being $e^+e^-\mu^+\mu^-$ events), against which the procedure is less effective.

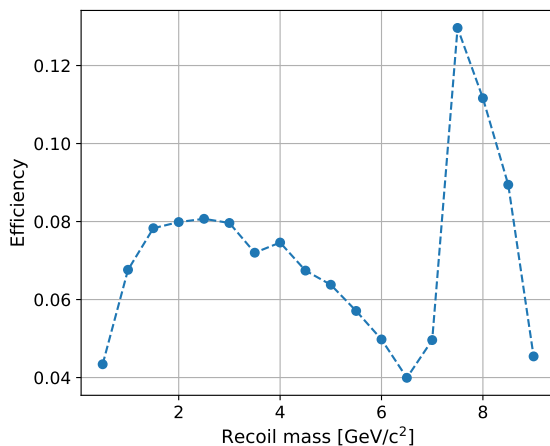


Figure 6.6: Signal efficiency after all the analysis cuts as a function of the recoil mass. The efficiencies are multiplied by the measured trigger efficiency (79%).

At this level of the analysis, the background originating from τ pair events is composed by only 15% of events in which both τ 's decay leptonically in muons: all the remaining fraction is dominated by τ decaying to pions. This shows a potentially big margin of improvement of this analysis when a better, KLM based, muon identification selection will be available.

We run the full analysis chain on all the signal and the background samples. Recoil mass bins of the generated signal samples, signal efficiencies and number of background events surviving the selections are shown in Table 6.1. Errors therein are MC statistical

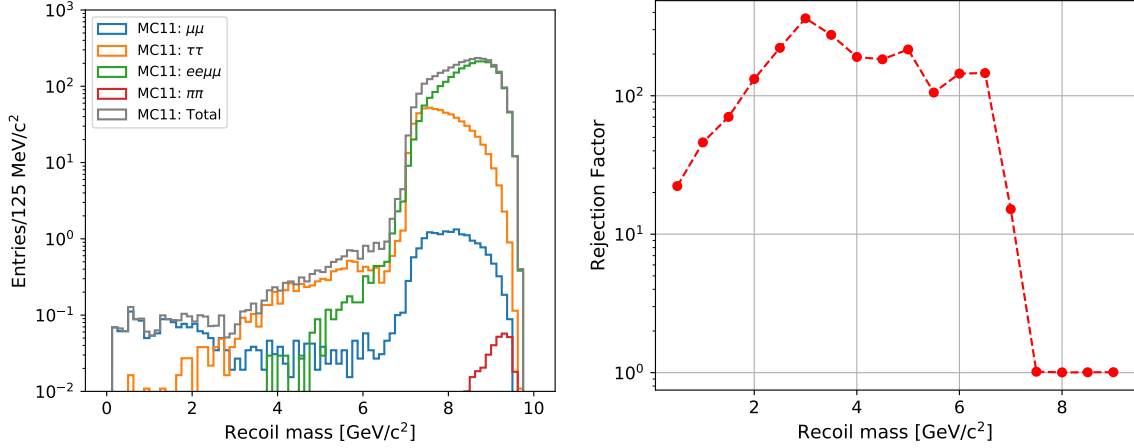


Figure 6.7: Number of surviving background events after the τ suppression procedure (left) and background rejection factor for the τ suppression procedure only (right) as a function of the recoil mass. Background samples are normalized to an integrated luminosity of 276 pb^{-1} and scaled by a trigger efficiency of 79%.

uncertainties only. It is important that for the analysis we need the signal efficiencies and the number of background events for the entire recoil mass spectrum and not only for the bins around the generated signal samples: these values will be given in Table 6.3.

Table 6.1: Recoil mass bins, signal efficiencies and number of background events after all the analysis selections for each generated Z' mass. Background normalized to an integrated luminosity of 276 pb^{-1} . Errors on efficiency and background events are MC statistical uncertainties only. Signal efficiencies and background include the 79% trigger efficiency.

$M_{Z'}$ [GeV/ c^2]	Mass window [GeV/ c^2]	Efficiency [%]	Background events
0.5	-0.15 - 1.15	4.34 ± 0.12	0.67 ± 0.05
1.0	0.63 - 1.37	6.76 ± 0.15	0.42 ± 0.04
1.5	1.28 - 1.72	7.82 ± 0.16	0.33 ± 0.04
2.0	1.84 - 2.16	7.98 ± 0.16	0.21 ± 0.03
2.5	2.37 - 2.63	8.06 ± 0.16	0.15 ± 0.03
3.0	2.90 - 3.10	7.96 ± 0.16	0.10 ± 0.02
3.5	3.42 - 3.58	7.20 ± 0.16	0.14 ± 0.03
4.0	3.93 - 4.07	7.46 ± 0.16	0.21 ± 0.04
4.5	4.44 - 4.56	6.74 ± 0.15	0.22 ± 0.03
5.0	4.95 - 5.05	6.37 ± 0.15	0.19 ± 0.03
5.5	5.47 - 5.53	5.70 ± 0.14	0.31 ± 0.06
6.0	5.97 - 6.03	4.97 ± 0.13	0.26 ± 0.05
6.5	6.47 - 6.53	3.99 ± 0.12	0.25 ± 0.06
7.0	6.97 - 7.03	4.96 ± 0.13	2.65 ± 0.23
7.5	7.46 - 7.54	12.96 ± 0.20	69.26 ± 1.13
8.0	7.97 - 8.03	11.16 ± 0.19	81.07 ± 1.36

6.2 τ suppression application to the LFV Z'

As already mentioned, we don't have a reliable LFV Z' signal simulation. Since any dedicated optimization for the LFV case is not possible, we applied exactly the same τ suppression procedure for the standard Z' to the surviving background events after all the selections listed in Section 4.3.2.

In Figure 6.8 we show, for the background samples centered around recoil masses of 2, 5 and 7 GeV/c^2 , the bidimensional $p_{rec}^{T,lmax} - p_{rec}^{T,lmin}$ distributions of the surviving events after the $p_{e\mu}^T$ cut, with the separating line from the standard Z' optimization superimposed.

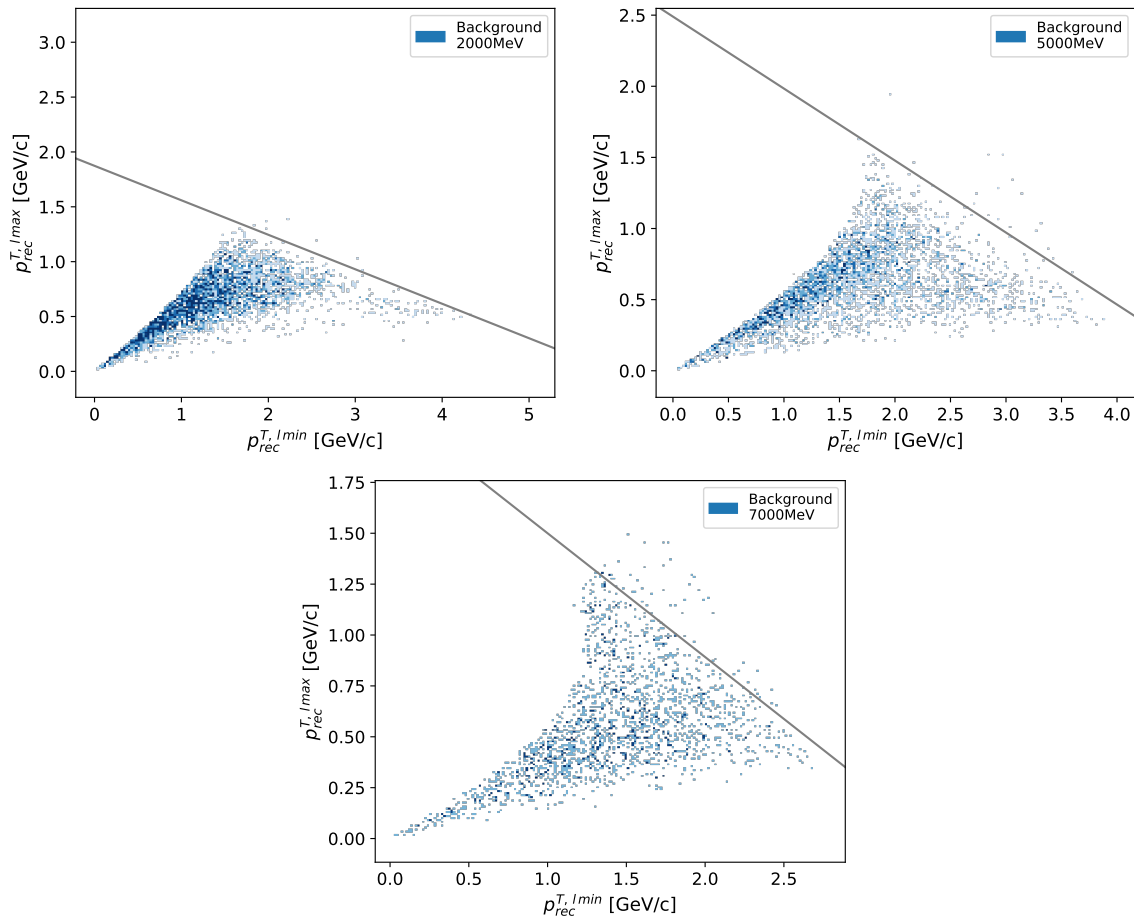


Figure 6.8: $p_{rec}^{T,lmax}$ vs $p_{rec}^{T,lmin}$ distributions after the $p_{e\mu}^T$ cut for background centered around recoil masses of 2, 5, 7 GeV/c^2 (left, middle and right respectively). The separating line from the standard Z' optimization is superimposed.

In Figure 6.9 we show the surviving background spectrum and the background rejection factor achieved by the τ suppression procedure only, as a function of the recoil mass. The main source of background is given by τ pair events, where one τ decays leptonically in an electron and the other τ decays to pion (and the pion is misidentified as a muon).

We run the full analysis chain on all the the background samples by grouping events in the same recoil mass bins as in Section 6.1. This is shown in Table 6.2. Errors therein are MC statistical uncertainties only. As for the the standard Z' , for the analysis we need the signal efficiencies and the number of background events for the entire recoil mass spectrum: these values will be given in Table 6.4.

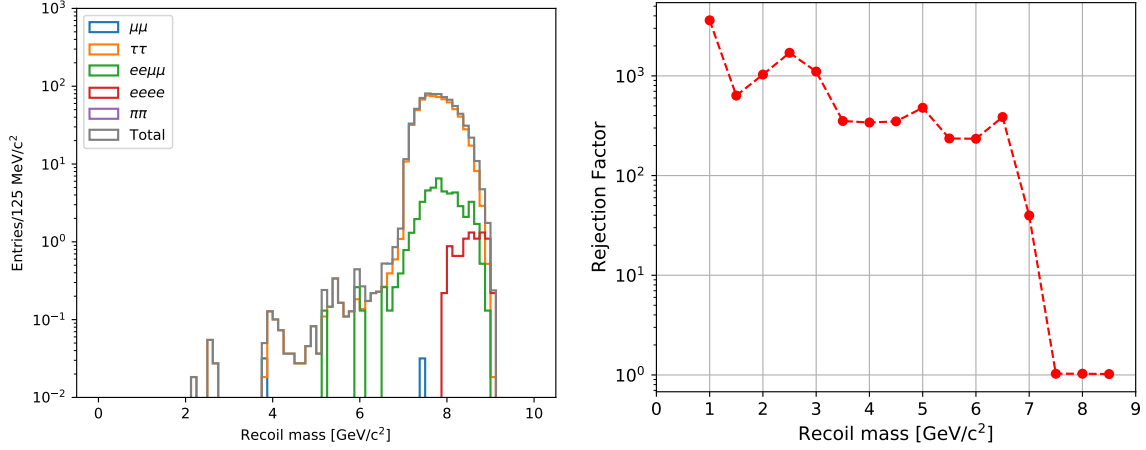


Figure 6.9: Number of surviving background events (left) and background rejection factor for the τ suppression procedure only (right) as a function of the recoil mass. Background samples are normalized to an integrated luminosity of 276 pb^{-1} and scaled by a trigger efficiency of 96%. The value of the background rejection at $0.5 \text{ GeV}/c^2$ could not be computed because no background events survived the selection

Table 6.2: Recoil mass bins and number of background events after all the analysis selections. Background normalized to an integrated luminosity of 276 pb^{-1} . Errors on background events are MC statistical uncertainties only. Signal efficiencies and background include the 96% trigger efficiency.

$M_{Z'}$ [GeV/c^2]	Mass range [GeV/c^2]	Background events
0.5	-0.15 - 1.15	0.00 ± 0.00
1.0	0.63 - 1.37	0.01 ± 0.01
1.5	1.28 - 1.72	0.04 ± 0.02
2.0	1.84 - 2.16	0.03 ± 0.01
2.5	2.37 - 2.63	0.03 ± 0.01
3.0	2.90 - 3.10	0.05 ± 0.02
3.5	3.42 - 3.58	0.16 ± 0.03
4.0	3.93 - 4.07	0.17 ± 0.03
4.5	4.44 - 4.56	0.17 ± 0.03
5.0	4.95 - 5.05	0.12 ± 0.03
5.5	5.47 - 5.53	0.18 ± 0.03
6.0	5.97 - 6.03	0.18 ± 0.06
6.5	6.47 - 6.53	0.09 ± 0.04
7.0	6.97 - 7.03	0.69 ± 0.07
7.5	7.46 - 7.54	29.02 ± 0.48
8.0	7.97 - 8.03	14.72 ± 0.36

6.3 Definition of the recoil mass windows

We defined a recoil mass window for each generated standard Z' mass, centered at the nominal mass and with a width, defined in term of multiples of the recoil mass resolution σ_w (see Section 5.2), such that it maximizes a $\text{FOM}_{\text{Punzi}}$ (Equation 6.1) over the entire recoil mass spectrum after the τ suppression procedure. The optimal value turned out to be a

width of $\pm 2\sigma_w$: this is shown in Figure 6.10.

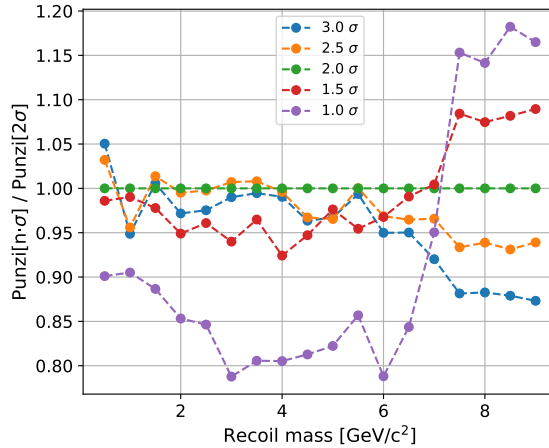


Figure 6.10: Ratio of the $\text{FOM}_{\text{P}_{\text{unzi}}}$ at the end of the analysis computed for different recoil mass window widths with respect to that computed for a mass window of $\pm 2\sigma$.

The recoil mass window widths vary from $1300 \text{ MeV}/c^2$ at $M_{Z'} = 0.5 \text{ GeV}/c^2$ to $53 \text{ MeV}/c^2$ at $M_{Z'} = 7 \text{ GeV}/c^2$, due to the different recoil mass resolution.

The signal inefficiency due to the mass window definition (signal events outside the window) is mostly caused by the Initial State Radiation (ISR) tail and it is found to be between 30% and 40%. This is already taken into account during the optimization process.

We adopted the same recoil mass windows also for the LFV Z' search.

6.4 Expected signal efficiencies and background yields over the entire recoil mass spectrum

The bin choice used in Table 6.1 and in Table 6.2 corresponds to the pattern of generated Z' masses and is not suited for an analysis on real data, as it doesn't cover all the possible recoil mass values. A new choice with contiguous mass intervals was thus made, based again on the results discussed in Section 5.2

Recoil mass bin widths and signal efficiencies are interpolated at the center of each bin (see Figure 5.3 and Figure 6.6, respectively) and the background yields are then recomputed. This is shown in Table 6.3 for the standard Z' search and in Table 6.4 for the LFV case. The statistical analysis (see Section 8) is then performed using these values, scaled by a factor 0.65 for the standard Z' and by a factor 0.9 for the LFV Z' (see Section 7.3).

Table 6.3: Signal efficiencies and number of background events after all the analysis selections in contiguous recoil mass bins for the standard Z' search. Background normalized to an integrated luminosity of 276 pb^{-1} . Errors on efficiency and background events are MC statistical uncertainties only. Signal efficiencies and background include the 79% trigger efficiency.

$M_{Z'}$ [GeV/ c^2]	Mass range [GeV/ c^2]	Efficiency [%]	Background events
0.50	-0.15 - 1.15	4.34 ± 0.13	0.67 ± 0.05
1.39	1.15 - 1.63	7.60 ± 0.16	0.33 ± 0.04
1.81	1.63 - 1.98	7.93 ± 0.17	0.26 ± 0.03
2.13	1.98 - 2.29	8.01 ± 0.17	0.22 ± 0.03
2.42	2.29 - 2.56	8.06 ± 0.17	0.19 ± 0.03
2.68	2.56 - 2.81	8.03 ± 0.17	0.14 ± 0.03
2.91	2.81 - 3.02	7.98 ± 0.17	0.12 ± 0.02
3.11	3.02 - 3.21	7.79 ± 0.17	0.11 ± 0.02
3.29	3.21 - 3.38	7.51 ± 0.16	0.17 ± 0.03
3.46	3.38 - 3.54	7.26 ± 0.16	0.16 ± 0.03
3.62	3.54 - 3.69	7.26 ± 0.16	0.16 ± 0.03
3.77	3.69 - 3.84	7.34 ± 0.16	0.21 ± 0.03
3.91	3.84 - 3.98	7.41 ± 0.16	0.26 ± 0.05
4.04	3.98 - 4.11	7.40 ± 0.16	0.23 ± 0.04
4.17	4.11 - 4.24	7.21 ± 0.16	0.24 ± 0.04
4.29	4.24 - 4.36	7.04 ± 0.16	0.25 ± 0.04
4.41	4.36 - 4.47	6.87 ± 0.16	0.26 ± 0.04
4.52	4.47 - 4.58	6.72 ± 0.16	0.28 ± 0.05
4.63	4.58 - 4.69	6.65 ± 0.16	0.22 ± 0.03
4.74	4.69 - 4.79	6.57 ± 0.15	0.29 ± 0.04
4.85	4.79 - 4.90	6.49 ± 0.15	0.28 ± 0.05
4.95	4.90 - 5.00	6.42 ± 0.15	0.32 ± 0.06
5.05	5.00 - 5.09	6.32 ± 0.15	0.26 ± 0.04
5.14	5.09 - 5.18	6.19 ± 0.15	0.41 ± 0.08
5.23	5.18 - 5.27	6.08 ± 0.15	0.23 ± 0.04
5.31	5.27 - 5.35	5.97 ± 0.15	0.27 ± 0.04
5.38	5.35 - 5.42	5.86 ± 0.15	0.36 ± 0.06
5.46	5.42 - 5.49	5.76 ± 0.15	0.31 ± 0.06
5.53	5.49 - 5.56	5.67 ± 0.14	0.32 ± 0.06

Continued on next page

Table 6.3: continued from previous page

$M_{Z'}$ [GeV/ c^2]	Mass range [GeV/ c^2]	Efficiency [%]	Background events
5.60	5.56 - 5.63	5.57 ± 0.14	0.29 ± 0.05
5.66	5.63 - 5.70	5.47 ± 0.14	0.34 ± 0.06
5.73	5.70 - 5.76	5.37 ± 0.14	0.45 ± 0.08
5.80	5.76 - 5.83	5.27 ± 0.14	0.35 ± 0.06
5.87	5.83 - 5.90	5.17 ± 0.14	0.39 ± 0.06
5.94	5.90 - 5.97	5.07 ± 0.14	0.31 ± 0.06
6.01	5.97 - 6.04	4.96 ± 0.14	0.30 ± 0.05
6.08	6.04 - 6.11	4.83 ± 0.13	0.58 ± 0.10
6.15	6.11 - 6.18	4.69 ± 0.13	0.30 ± 0.07
6.21	6.18 - 6.25	4.56 ± 0.13	0.41 ± 0.08
6.28	6.25 - 6.31	4.43 ± 0.13	0.37 ± 0.07
6.34	6.31 - 6.38	4.30 ± 0.13	0.53 ± 0.10
6.41	6.38 - 6.44	4.17 ± 0.12	0.38 ± 0.09
6.47	6.44 - 6.50	4.05 ± 0.12	0.35 ± 0.08
6.53	6.50 - 6.56	4.05 ± 0.12	0.29 ± 0.07
6.58	6.56 - 6.61	4.16 ± 0.12	0.55 ± 0.10
6.64	6.61 - 6.67	4.27 ± 0.13	0.57 ± 0.10
6.69	6.67 - 6.72	4.37 ± 0.13	0.83 ± 0.13
6.75	6.72 - 6.77	4.47 ± 0.13	1.32 ± 0.18
6.80	6.77 - 6.83	4.57 ± 0.13	1.18 ± 0.15
6.85	6.83 - 6.88	4.67 ± 0.13	1.47 ± 0.18
6.90	6.88 - 6.93	4.77 ± 0.13	1.81 ± 0.20
6.95	6.93 - 6.98	4.87 ± 0.13	1.85 ± 0.20
7.01	6.98 - 7.03	5.06 ± 0.14	3.08 ± 0.24
7.06	7.03 - 7.09	5.92 ± 0.14	9.34 ± 0.37
7.12	7.09 - 7.14	6.81 ± 0.15	17.47 ± 0.50
7.17	7.14 - 7.20	7.75 ± 0.16	23.43 ± 0.57
7.24	7.20 - 7.27	8.74 ± 0.17	32.93 ± 0.71
7.30	7.27 - 7.33	9.77 ± 0.18	41.23 ± 0.81
7.37	7.33 - 7.40	10.86 ± 0.19	50.41 ± 0.91
7.44	7.40 - 7.47	11.98 ± 0.20	62.98 ± 1.06
7.51	7.47 - 7.55	12.92 ± 0.21	69.32 ± 1.13

Continued on next page

Table 6.3: continued from previous page

$M_{Z'}$ [GeV/ c^2]	Mass range [GeV/ c^2]	Efficiency [%]	Background events
7.58	7.55 - 7.62	12.66 ± 0.20	73.16 ± 1.19
7.66	7.62 - 7.69	12.40 ± 0.20	76.22 ± 1.24
7.73	7.69 - 7.76	12.15 ± 0.20	76.07 ± 1.25
7.79	7.76 - 7.83	11.91 ± 0.20	79.03 ± 1.30
7.86	7.83 - 7.89	11.67 ± 0.20	80.55 ± 1.33
7.92	7.89 - 7.95	11.44 ± 0.20	77.66 ± 1.32
7.98	7.95 - 8.01	11.22 ± 0.19	80.99 ± 1.36
8.04	8.01 - 8.07	10.97 ± 0.19	83.10 ± 1.39

Table 6.4: Number of background events after all the analysis selections in contiguous recoil mass bins for the LFV Z' search. Background normalized to an integrated luminosity of 276 pb^{-1} . Errors on efficiency and background events are MC statistical uncertainties only. Signal efficiencies and background include the 96% trigger efficiency.

$M_{Z'}$ [GeV/ c^2]	Mass range [GeV/ c^2]	Background events
0.50	-0.15 - 1.15	0.00 ± 0.00
1.39	1.15 - 1.63	0.02 ± 0.01
1.81	1.63 - 1.98	0.03 ± 0.01
2.13	1.98 - 2.29	0.04 ± 0.02
2.42	2.29 - 2.56	0.01 ± 0.01
2.68	2.56 - 2.81	0.05 ± 0.02
2.91	2.81 - 3.02	0.03 ± 0.01
3.11	3.02 - 3.21	0.07 ± 0.02
3.29	3.21 - 3.38	0.08 ± 0.02
3.46	3.38 - 3.54	0.17 ± 0.03
3.62	3.54 - 3.69	0.11 ± 0.03
3.77	3.69 - 3.84	0.09 ± 0.02
3.91	3.84 - 3.98	0.13 ± 0.03
4.04	3.98 - 4.11	0.18 ± 0.03
4.17	4.11 - 4.24	0.09 ± 0.02
4.29	4.24 - 4.36	0.16 ± 0.03
4.41	4.36 - 4.47	0.13 ± 0.03
4.52	4.47 - 4.58	0.19 ± 0.04
4.63	4.58 - 4.69	0.09 ± 0.02
4.74	4.69 - 4.79	0.15 ± 0.05
4.85	4.79 - 4.90	0.12 ± 0.03
4.95	4.90 - 5.00	0.15 ± 0.03
5.05	5.00 - 5.09	0.07 ± 0.02
5.14	5.09 - 5.18	0.17 ± 0.05
5.23	5.18 - 5.27	0.16 ± 0.03
5.31	5.27 - 5.35	0.20 ± 0.04
5.38	5.35 - 5.42	0.15 ± 0.03
5.46	5.42 - 5.49	0.19 ± 0.04
5.53	5.49 - 5.56	0.16 ± 0.03
5.60	5.56 - 5.63	0.21 ± 0.05

Continued on next page

Table 6.4: continued from previous page

$M_{Z'}$ [GeV/ c^2]	Mass range [GeV/ c^2]	Background events
5.66	5.63 - 5.70	0.19 ± 0.05
5.73	5.70 - 5.76	0.20 ± 0.06
5.80	5.76 - 5.83	0.11 ± 0.03
5.87	5.83 - 5.90	0.17 ± 0.05
5.94	5.90 - 5.97	0.27 ± 0.07
6.01	5.97 - 6.04	0.14 ± 0.04
6.08	6.04 - 6.11	0.15 ± 0.04
6.15	6.11 - 6.18	0.13 ± 0.03
6.21	6.18 - 6.25	0.17 ± 0.05
6.28	6.25 - 6.31	0.11 ± 0.04
6.34	6.31 - 6.38	0.17 ± 0.03
6.41	6.38 - 6.44	0.06 ± 0.02
6.47	6.44 - 6.50	0.09 ± 0.04
6.53	6.50 - 6.56	0.11 ± 0.04
6.58	6.56 - 6.61	0.12 ± 0.04
6.64	6.61 - 6.67	0.17 ± 0.05
6.69	6.67 - 6.72	0.19 ± 0.04
6.75	6.72 - 6.77	0.23 ± 0.06
6.80	6.77 - 6.83	0.38 ± 0.07
6.85	6.83 - 6.88	0.34 ± 0.07
6.90	6.88 - 6.93	0.51 ± 0.09
6.95	6.93 - 6.98	0.50 ± 0.09
7.01	6.98 - 7.03	0.94 ± 0.09
7.06	7.03 - 7.09	5.45 ± 0.22
7.12	7.09 - 7.14	9.25 ± 0.27
7.17	7.14 - 7.20	13.13 ± 0.31
7.24	7.20 - 7.27	18.54 ± 0.39
7.30	7.27 - 7.33	21.54 ± 0.43
7.37	7.33 - 7.40	25.00 ± 0.45
7.44	7.40 - 7.47	28.38 ± 0.49
7.51	7.47 - 7.55	29.09 ± 0.47
7.58	7.55 - 7.62	29.22 ± 0.51

Continued on next page

Table 6.4: continued from previous page

$M_{Z'}$ [GeV/ c^2]	Mass range [GeV/ c^2]	Background events
7.66	7.62 - 7.69	26.60 ± 0.47
7.73	7.69 - 7.76	25.13 ± 0.48
7.79	7.76 - 7.83	21.96 ± 0.44
7.86	7.83 - 7.89	19.57 ± 0.43
7.92	7.89 - 7.95	17.34 ± 0.39
7.98	7.95 - 8.01	15.26 ± 0.37
8.04	8.01 - 8.07	13.95 ± 0.36

Chapter 7

Systematic uncertainties and data validation

In this chapter we discuss about the systematic uncertainties related to trigger, tracking and PID. Then, we discuss about a general validation of our MC simulated samples, comparing them with selected signal-free samples.

7.1 Systematic uncertainties

All the studies shown in this section refers to both the standard Z' and the LFV one, unless clearly stated.

7.1.1 Uncertainty related to trigger

This work relies on the trigger logics developed to select low-multiplicity events, in particular the CDC trigger logic (called **ffo**) and the ECL one (called **hie**). We remind here that the **ffo** trigger logic selects events with at least two tracks with an opening angle in the transverse $r - \phi$ plane ($\Delta\phi$) larger than 90° and with energy depositions in ECL incompatible with a Bhabha final state¹, while the **hie** logic selects events with a total energy deposition in the barrel and part of the endcap ECL larger than approximately 1 GeV and with topologies incompatible with a Bhabha final state.

The efficiency of the **ffo** trigger is measured by selecting $e^+e^- \rightarrow e^+e^-$ events (ee sample) having a total energy deposition in the ECL larger then 1.5 GeV [34]. The efficiency is measured as the ratio between the number of events triggered simultaneously by both CDC and ECL and the number of events triggered by the ECL. The trigger efficiency is found to vary with runs: to cope with that, for this work we only used runs where the CDC

¹In the trigger logic, an event is compatible with a Bhabha final state when two ECL clusters satisfy the following criteria:

- $\Sigma\theta \in [165^\circ, 190^\circ]$;
- $|\Delta\phi| \in [160^\circ, 200^\circ]$;
- $E_1 > 3 \text{ GeV} \wedge E_2 > 3 \text{ GeV} \wedge (E_1 > 4.5 \text{ GeV} \vee E_2 > 4.5 \text{ GeV})$;

where $\Sigma\theta$ is the sum of the polar angles of the two clusters, $\Delta\phi$ is the difference between the ϕ angles and E_1, E_2 are the energies of the two clusters. All these quantities are computed in the CM frame.

trigger efficiency was larger than 50%. The final trigger efficiency is defined as average of efficiencies measured in the selected runs weighted with the luminosity of the corresponding run. The trigger efficiency is found to be $79.0 \pm 0.1\%$, for a total integrated luminosity of 276 pb^{-1} (see Figure 7.1).

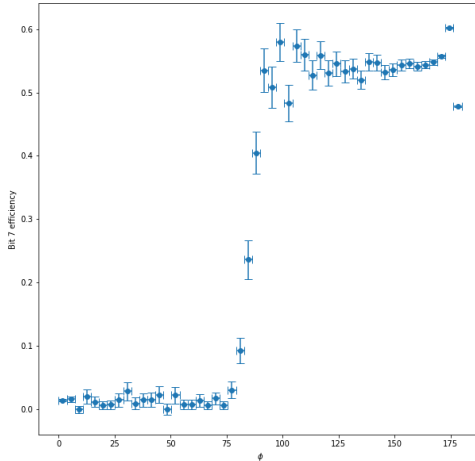


Figure 7.1: Measured efficiency of the CDC trigger logic `ffo` as a function of $\Delta\phi$.

By varying the requirements used to select the ee sample (polar angle θ of the tracks, number of hits in the CDC, etc.), we found that the total systematic uncertainty to be assigned to the measurement of the `ffo` trigger efficiency is 6%.

The measurement of the `hie` trigger efficiency is discussed in Section 7.2.4.

7.1.2 Uncertainty related to tracking

The tracking efficiency is measured on both Phase 2 data and MC simulated samples by using radiative Bhabha events ($ee\gamma$) and a tag-and-probe method [38]. In particular, using the kinematics of one of the two tracks and of the radiated photon (tag), it is possible to find expected position of the other track (probe).

While for MC simulated sample the tracking efficiency is about 100%, the efficiency measured by using Phase 2 data is $\approx 95\%$ (see Figure 7.2). The efficiency is to be intended per track: it implies that we expect a discrepancy of $\approx 10\%$ per event between data and MC. This large discrepancy can be explained as the sum of several effects: a tracking algorithm not well optimized to operate with a partial VXD detector; beam background in the CDC larger than expected. These effects are highly mitigated in newer versions of the tracking algorithm, used since the 2019 data taking phase (Phase 3).

By varying the requirements used to select the $ee\gamma$ sample, we found that the total systematic uncertainty to be assigned to the measurement of the tracking efficiency is 4% (2% per track).

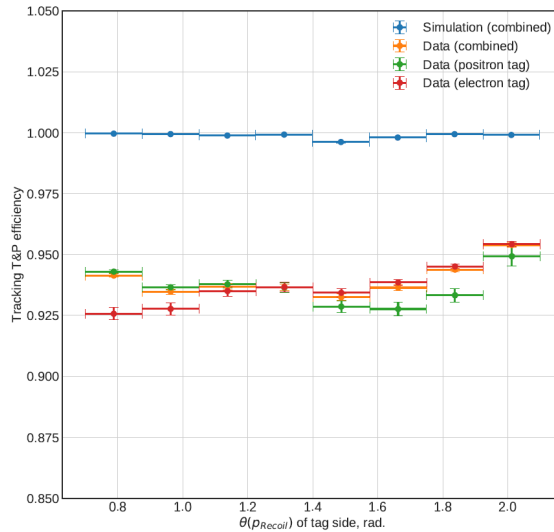


Figure 7.2: Measured tracking efficiency as a function of the predicted polar angle θ in MC simulated samples (blue), combined Phase 2 data (orange). In Phase 2 data, no significant discrepancies are found if positrons (green) or electrons (red) are considered.

7.1.3 Uncertainty related to PID

The ECL-based PID efficiency of the muons is measured on both Phase 2 data and MC simulated samples by using radiative dimuon events ($\mu\mu\gamma$) and using the KLM subdetector to self-tag a track as a muon [39]. Because of the instability of the KLM subdetector during the Phase 2 commissioning run, this study was performed on a small Phase 2 data set and it is assumed to be valid for the entire Phase 2 run, given the stable performance of the ECL subdetector.

The selection of the $\mu\mu\gamma$ sample is done in a similar way as described in Section 7.2.2. No relevant discrepancies between data and MC are found, since the same efficiency is found in both cases.

Varying the requirements used to select the $\mu\mu\gamma$ sample, we found that the total systematic uncertainty to be assigned to the measurement of the PID efficiency of the muons is 4% (2% per track).

The ECL-based PID efficiency is also measured for electrons and positrons by using a clean sample of eee events. No relevant discrepancies between data and MC were found, assigning a systematic uncertainty of the PID efficiency of the electrons and positron is 2% per track.

7.2 Validation of MC simulated samples on data

The goals of the validation procedure are: to obtain an estimate of the background based on real data and compare it with the one evaluated in the MC simulations; to check the effect of the individual analysis selections without unblinding the data sample 3.

Three different procedures, each corresponding to a differently selected sample, are devised:

- ee sample: beside the Bhabha and eee backgrounds, this sample is dominated by $\tau\tau(\gamma)$

events, with both τ 's decaying to electrons, whose kinematics is almost identical to one of the the dominant Z' analysis background ($\tau\tau(\gamma)$ events, with both τ 's decaying to muons); all the analysis selections, with the exception of the PID ones, and including the τ suppression procedure, can thus be checked. Requiring two identified electrons avoids any unblinding issue;

- $\mu\mu\gamma$ (and $e\mu\gamma$, $ee\gamma$) samples: this sample is particularly useful to check the low recoil mass region, being dominantly composed by the ISR QED $\mu\mu\gamma$ process (the $e\mu\gamma$ and $ee\gamma$ samples are used to cross check the $\mu\mu\gamma$ one). The presence of a photon with a reconstructed energy above 1 GeV (or 1.5 GeV) decreases the signal efficiency by $\approx \alpha_{QED}$, thus avoiding any unblinding issue;
- $\mu\mu$ (and $e\mu$) samples after the application of a partially reversed τ suppression procedure: this technique allows to strongly suppress hypothetical signal contributions, thus leaving a signal-free sample, very similar to the Z' analysis one before the τ suppression procedure, thus avoiding any unblinding issue;

We performed extensive comparisons between data and MC on the most important analysis variables. Beside looking at the overall number of events in data and MC, we checked, for each validation sample, those same information in three, different, large recoil mass regions, as they correspond, for events with two identified muons, to different sources of contributing background:

- $-2 < M_{\text{rec}} < 3 \text{ GeV}/c^2$, dominated by $\mu\mu(\gamma)$ events;
- $3 < M_{\text{rec}} < 6 \text{ GeV}/c^2$, dominated by $\tau\tau(\gamma)$ events;
- $6 < M_{\text{rec}} < 11 \text{ GeV}/c^2$, dominated by $ee\mu\mu$ events.

The same recoil mass regions are used to check also the background contributing to the LFV Z' search.

Unless differently (and clearly) stated, we generally selected data events with the CDC `ffo` trigger fired, whose efficiency, evaluated to be 79% in Bhabha events, was used to scale the MC expectations. Samples with electrons or photons with a reconstructed energy above 1 GeV can be triggered by the ECL `hie` trigger logic too, thus providing the possibility of further interesting checks (including alternative measurements of the `ffo` trigger efficiency).

7.2.1 Data validation with ee sample

In order to select an ee sample, all the selections described in Section 4.3.1 are applied on data and MC, with the exception of the ones requiring a ECL-based muon selection (selection 4), which is replaced requiring a ratio between the energy of the associated ECL cluster and the momentum of the track (E/p) to be $0.8 < E/p < 1.2$.

Recoil mass distributions for data and MC after all the previous selections (and before the τ suppression procedure) are shown in Figure 7.3: the agreement is very good, with a ratio between data and MC of $\approx 0.97 \pm 0.01$ overall the mass spectrum.

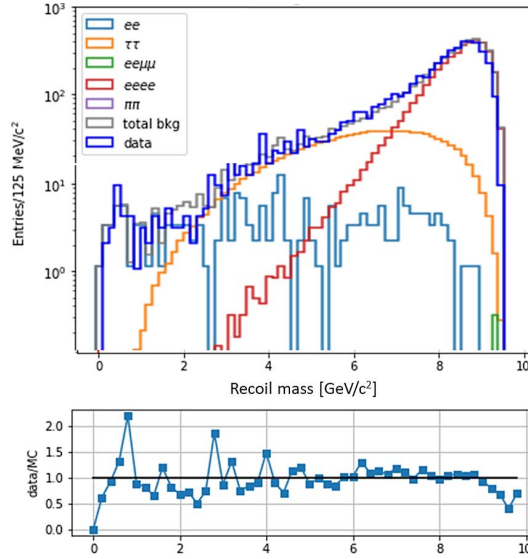


Figure 7.3: Recoil mass distribution of data and MC (on top) and ratio between data and MC (on bottom) for the ee sample before having applied the τ suppression. MC samples are normalized to an integrated luminosity of 276 pb^{-1} and scaled by a trigger efficiency of 79%.

After the application of the τ suppression procedure, 20 events are found in data in the first two large recoil mass regions, while 18.4 are expected in MC. These numbers can be interpreted as a validation of the τ suppression procedure with a statistical uncertainty of $\approx 22\%$. In our upper limit calculations, we use this 22% uncertainty as a statistical uncertainty on the background level knowledge coming from the τ suppression procedure only for both the standard and the LFV Z' searches.

7.2.2 Data validation with $\mu\mu\gamma$ (and $e\mu\gamma$, $ee\gamma$) sample

In order to select a clean $\mu\mu\gamma$ sample, we applied on both data and MC the selections described in Section 4.3 but with some modifications. We required the presence in the barrel ECL of a photon with a reconstructed energy E_γ larger than 1 GeV. Furthermore, the selection 5 was dropped and, in selection 6, the requirement to have an extra energy in the ECL $E_{\text{ECL}}^{\text{extra}}$ smaller than 0.4 GeV was replaced by the requirement $E_{\text{ECL}}^{\text{extra}} - E_\gamma < 0.4 \text{ GeV}$. All the other selections were not modified.

The contributing sources of background are the same as in the standard Z' analysis, but one has to take into account that the generator AAFH used to simulate the $ee\mu\mu$ background does not include the generation of ISR or FSR photons in the final state. To reduce its importance, a further cut was introduced on the direct dimuon mass: $M_{\mu\mu} > 3 \text{ GeV}/c^2$. The $ee\mu\mu$ contribution is anyway relevant, especially for high recoil masses $M_{\text{rec}} > 6 \text{ GeV}/c^2$. Recoil variables are always referred with respect to the dimuon system, regardless the presence of a reconstructed photon.

Data and MC distributions are compared after the generic selections (before applying the τ suppression procedure). This is shown in Figure 7.4, as a function of the squared recoil mass, for the three large recoil mass regions.

Discrepancies of the order of 30% are visible, with data consistently below the MC expect-

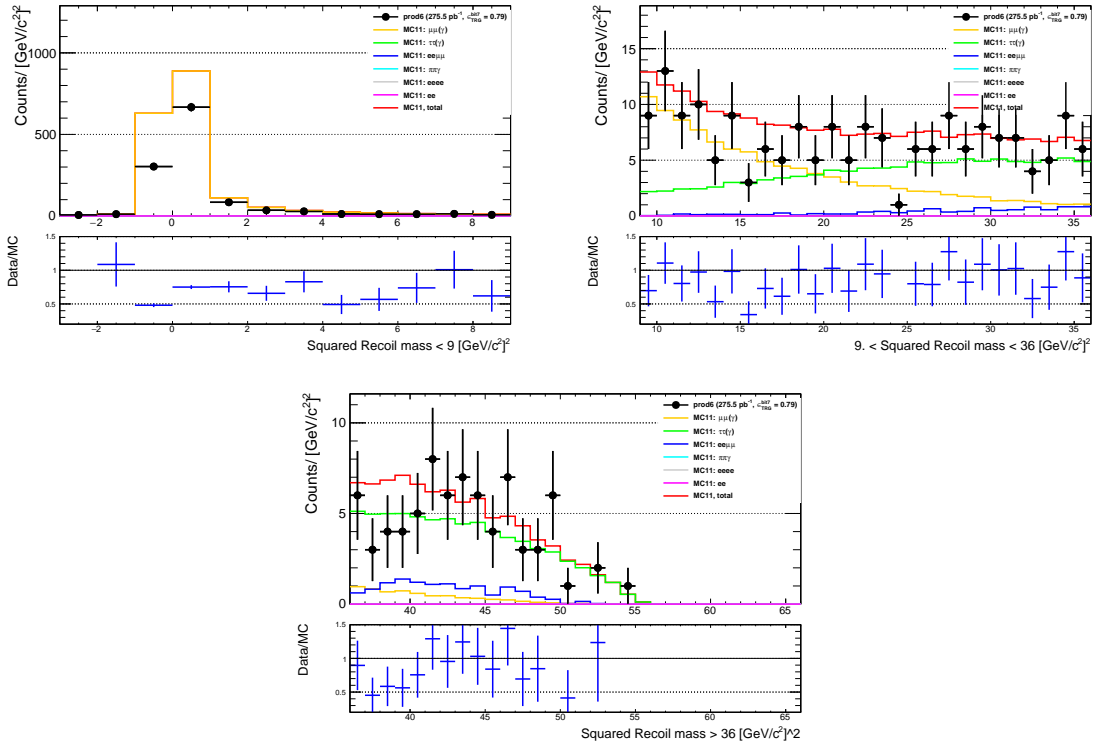


Figure 7.4: Squared recoil mass distribution for the $\mu\mu\gamma$ validation sample in the three large recoil mass regions. MC samples are normalized to an integrated luminosity of 276 pb^{-1} and scaled by a trigger efficiency of 79%.

tations (see also Tables 7.1 and 7.2). This is particularly evident, for statistical reasons, in the first large recoil mass window, largely dominated by the radiative $\mu\mu\gamma$ QED background. It was thus checked if the discrepancy might be originated by the $\mu\mu(\gamma)$ generator. A special sample of $\mu\mu(\gamma)$ generator was produced using *BabaYaga@NLO* and analyzed through the same chain: differences at about 1% level were found with respect to the standard *KKMC* generated sample, confirming the discrepancy of about 30% with respect to data.

A smaller discrepancy, of the order of 10%, are instead found in the $e\mu\gamma$ sample.

We then studied the effect of the individual selections. This is shown in Figure 7.5, which summarizes the ratio between data and MC as a function of the applied selection. In the plot shown in the figure, the 79% efficiency correction due to the trigger was applied only at the moment in which the requirement of having the `ffo` logic fired was made (fourth point in the plot, denoted with “`bit7==1`”): before that, a 100% trigger efficiency was assumed (which is probably an overestimate, since the presence of the photon satisfies the requirement to have the trigger logic “`hie`” fired, that has an efficiency of 96%).

We show in Figures 7.6, 7.7, 7.8, 7.9, 7.10, 7.11 and 7.12 the distributions of the relevant variables used in (or important for) the analysis.

No evident indication of a possible source of discrepancy comes out: most of the ratio between data and MC looks reasonably flat within the statistical fluctuations, with the exception of the ratio as a function of the azimuthal angle ϕ of the muons (see Figure 7.7). We know that the `ffo` trigger logic in Phase 2 data produces strong ϕ dependencies due to hardware issues.

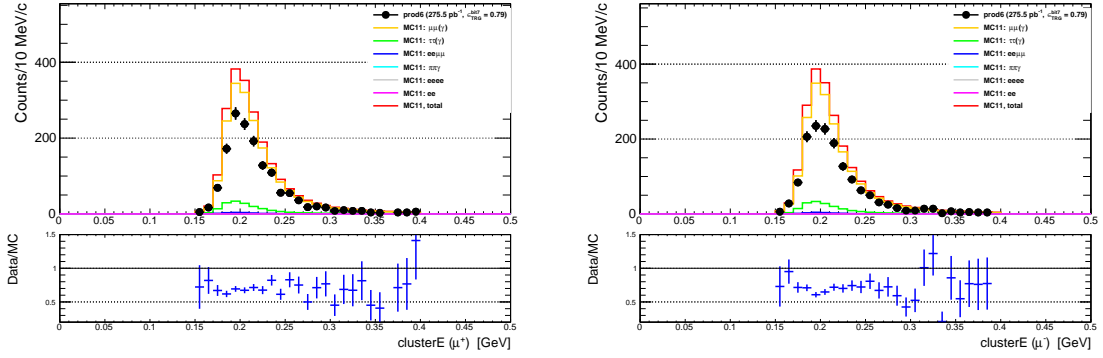


Figure 7.8: Energy of the associated ECL cluster of the two muons in the $\mu\mu\gamma$ validation sample: positive charge (left), negative charge (right). MC samples are normalized to an integrated luminosity of 276 pb^{-1} and scaled by a trigger efficiency of 79%.

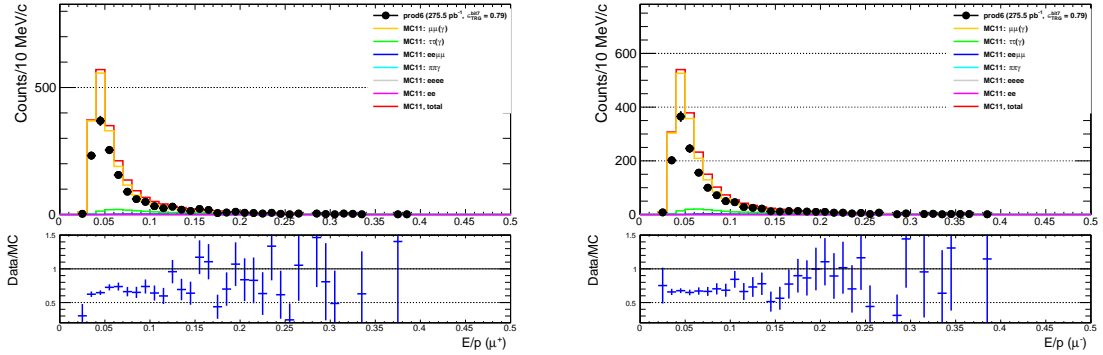


Figure 7.9: Ratio between the energy of the associated ECL cluster and the momentum of the track of the two muons in the $\mu\mu\gamma$ validation sample: positive charge (left), negative charge (right). MC samples are normalized to an integrated luminosity of 276 pb^{-1} and scaled by a trigger efficiency of 79%.

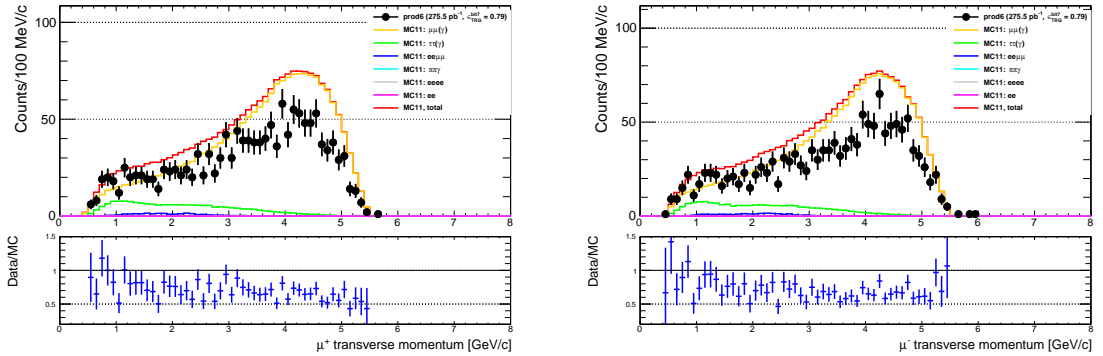


Figure 7.10: Transverse momentum of the two muons in the $\mu\mu\gamma$ validation sample: positive charge (left), negative charge (right). MC samples are normalized to an integrated luminosity of 276 pb^{-1} and scaled by a trigger efficiency of 79%.

Section 7.2.4. The entire validation with the $\mu\mu\gamma$ sample can be repeated by requiring only the `hie` trigger logic to be fired. The result, assuming an overestimated 100% efficiency for `hie`, is in agreement with that obtained with the `ffo` trigger (see Tables 7.1 and 7.2).

We then studied the $e\mu\gamma$ and $ee\gamma$ final states, using both the `ffo` and `hie` trigger logics. The $e\mu\gamma$ sample contain much less $\mu\mu$ and ee background, due to the PID requirement, and it

found to be negligible.

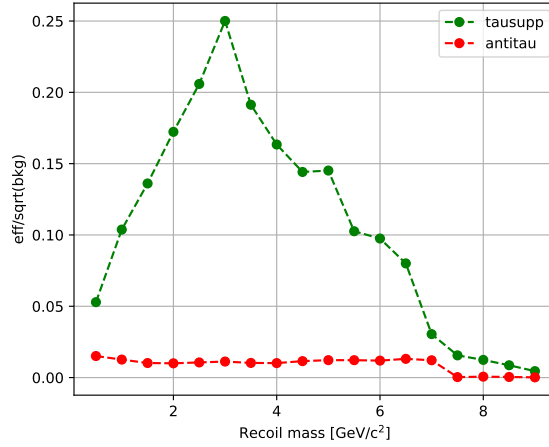


Figure 7.13: Punzi FOM as a function of the recoil mass for the analysis with the τ suppression applied (green) and with the partially reversed τ suppression applied (red).

After having applied the partially reversed τ suppression, the results of the ratio between data and MC is the full recoil mass spectrum are 0.64 ± 0.02 and 0.90 ± 0.02 for $\mu\mu$ and $e\mu$ samples respectively. They are shown for the $\mu\mu$ sample in Figure 7.14, as a function of the squared recoil mass, for the three large recoil mass regions.

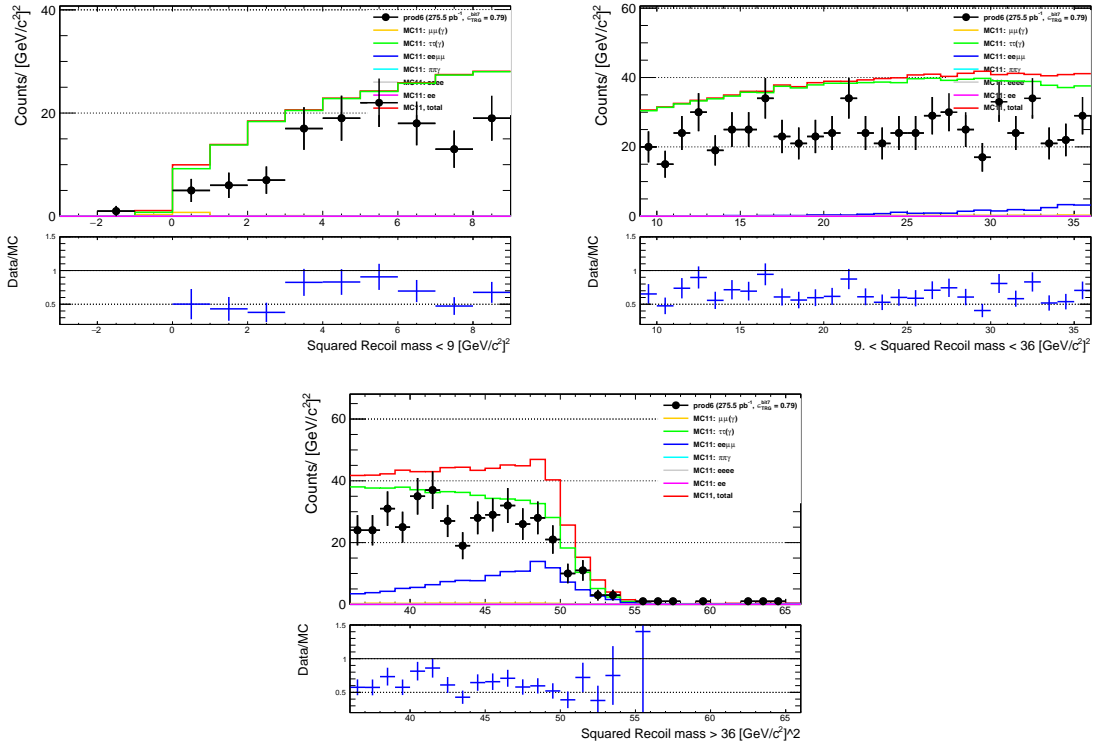


Figure 7.14: Squared recoil mass distribution for the $\mu\mu$ validation sample with a partially reversed τ suppression procedure in the three large recoil mass regions. MC samples are normalized to an integrated luminosity of 276 pb^{-1} and scaled by a trigger efficiency of 79%.

These results fully confirm the discrepancies between data and MC observed with the $\mu\mu\gamma$ and $e\mu\gamma$ samples (see also Tables 7.1 and 7.2).

In analogy with the $\mu\mu\gamma$ case, we show in Figures 7.15, 7.16, 7.17, 7.18, 7.19, 7.20, 7.21 the distributions of the relevant variables used in (or important for) the analysis.

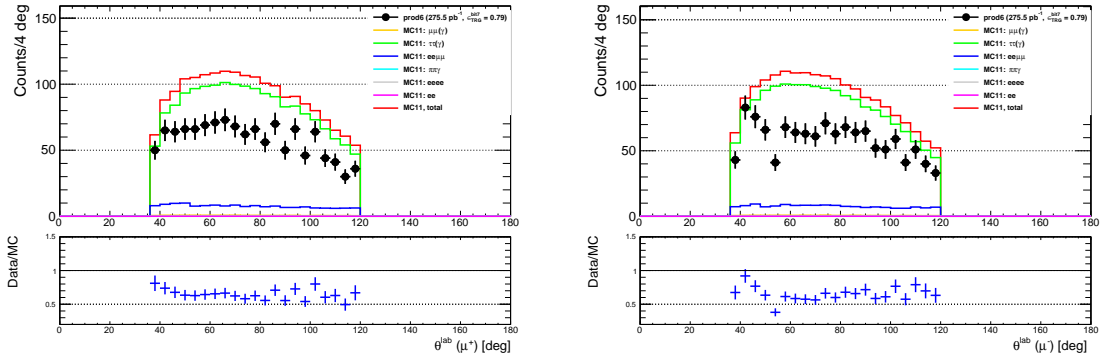


Figure 7.15: Polar angle θ in the LAB frame of the two muons in the $\mu\mu$ validation sample with a partially reversed τ suppression procedure: positive charge (left), negative charge (right). MC samples are normalized to an integrated luminosity of 276 pb^{-1} and scaled by a trigger efficiency of 79%.

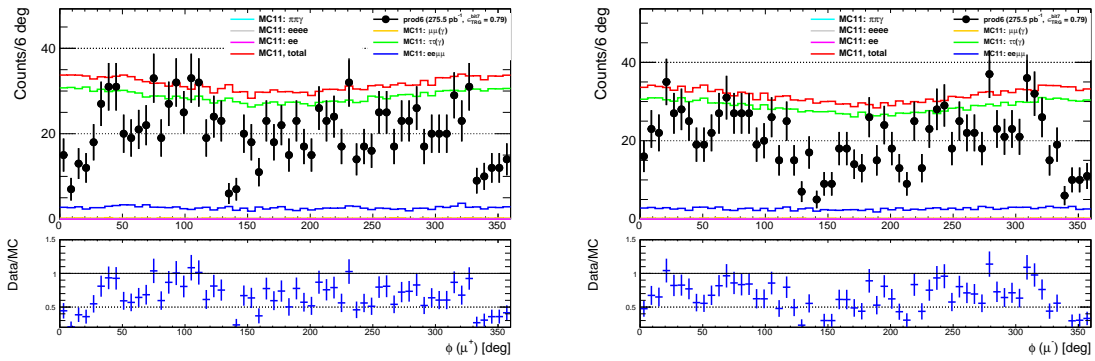


Figure 7.16: Azimuthal angle ϕ in the LAB frame of the two muons in the $\mu\mu$ validation sample with a partially reversed τ suppression procedure: positive charge (left), negative charge (right). MC samples are normalized to an integrated luminosity of 276 pb^{-1} and scaled by a trigger efficiency of 79%.

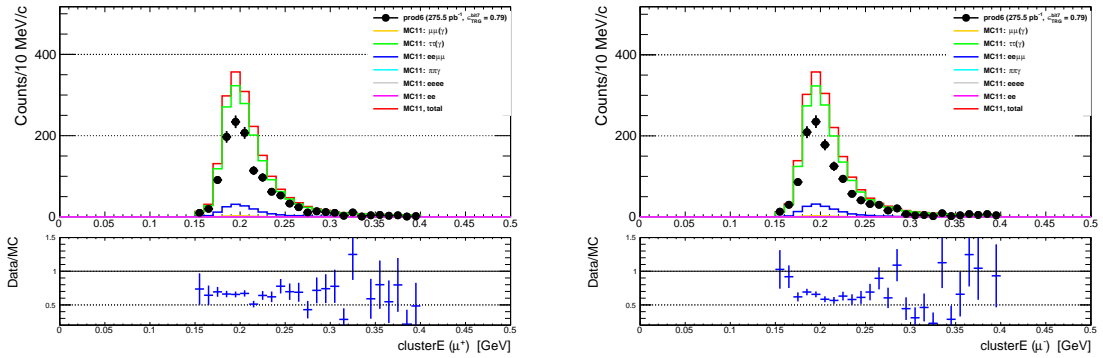


Figure 7.17: Energy of the associated ECL cluster of the two muons in the $\mu\mu$ validation sample with a partially reversed τ suppression procedure: positive charge (left), negative charge (right). MC samples are normalized to an integrated luminosity of 276 pb^{-1} and scaled by a trigger efficiency of 79%.

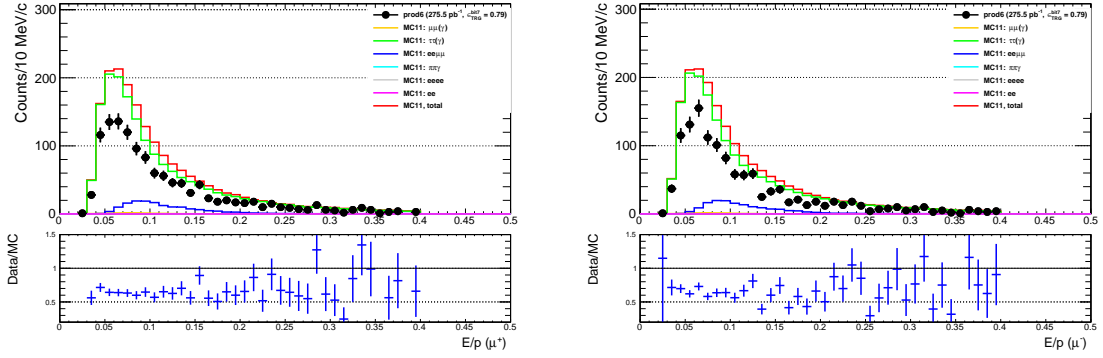


Figure 7.18: Ratio between the energy of the associated ECL cluster and the momentum of the track of the two muons in the $\mu\mu$ validation sample with a partially reversed τ suppression procedure: positive charge (left), negative charge (right). MC samples are normalized to an integrated luminosity of 276 pb^{-1} and scaled by a trigger efficiency of 79%.

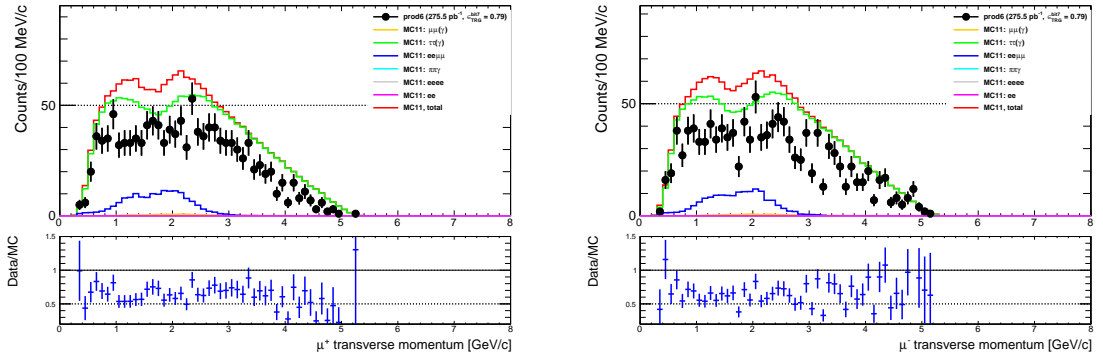


Figure 7.19: Transverse momentum of the two muons in the $\mu\mu$ validation sample with a partially reversed τ suppression procedure: positive charge (left), negative charge (right). MC samples are normalized to an integrated luminosity of 276 pb^{-1} and scaled by a trigger efficiency of 79%.

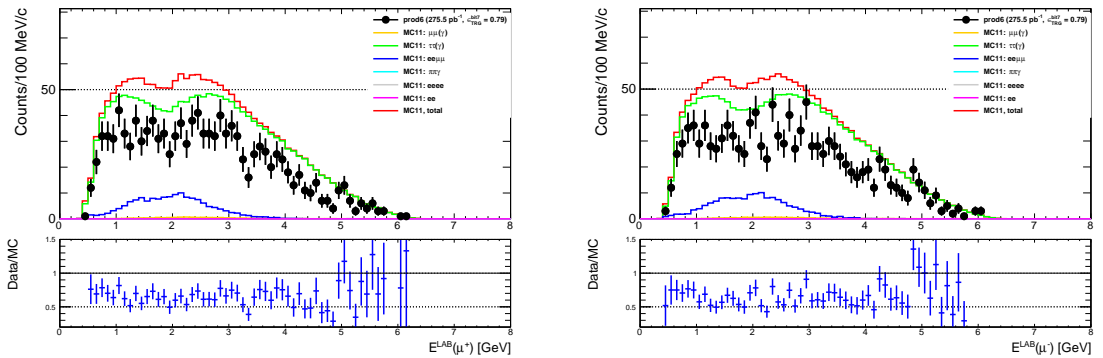


Figure 7.20: Energy in the LAB frame of the two muons in the $\mu\mu$ validation sample with a partially reversed τ suppression procedure: positive charge (left), negative charge (right). MC samples are normalized to an integrated luminosity of 276 pb^{-1} and scaled by a trigger efficiency of 79%.

No evident indication of a possible source of discrepancy comes out: most of the distributions look reasonably flat within the statistical fluctuations, with the exception of the ratio as a function of the azimuthal angle ϕ of the muons (see Figure 7.16), as already noticed in the $\mu\mu\gamma$ sample.

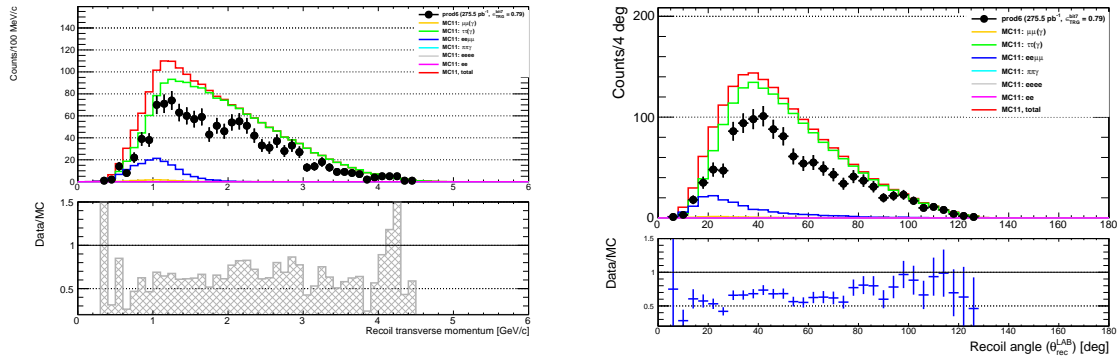


Figure 7.21: Transverse momentum (left) and polar angle (right) of the system recoiling against the two muons in the $\mu\mu$ validation sample with a partially reversed τ suppression procedure. MC samples are normalized to an integrated luminosity of 276 pb^{-1} and scaled by a trigger efficiency of 79%.

7.2.4 Trigger validation

A possible cause of the observed discrepancies between data and MC could be the CDC trigger logic `ffo`, which had hardware issues during the Phase 2 data taking. Its efficiency is measured to be 79% in [34] with Bhabha events, using the ECL `hie` trigger logic as a reference (see Section 7.1.1).

A pure $\mu\mu$ event, due to the small energy depositions in the ECL, can not be triggered by the `hie` logic, making impossible the measurement of the `ffo` logic. On the other hand, $\mu\mu\gamma$ events (see Section 7.2.2) with photon energies above 1 GeV are able to fire the ECL trigger, and thus allow the CDC trigger efficiency measurement.

The $\mu\mu\gamma$ sample is selected as described in Section 7.2.2. Furthermore, the `hie` trigger logic is required to be fired. The efficiency of the `ffo` trigger logic ϵ_{ffo} is defined as the number of times in which `ffo` and `hie` are both fired, divided by the number of times in which `hie` is fired. The result of this measurement is $\epsilon_{\text{ffo}} = 0.747 \pm 0.007$, to be compared with 79% evaluated in [34].

The strong azimuthal non uniformities, induced by the `ffo` trigger, are then investigated (see for example Figure 7.7 and Figure 7.16). The trigger efficiency ϵ_{ffo} is measured as a function of the minimum (Φ_{min}) and maximum (Φ_{max}) track azimuth angle in the event: these measurements are shown in Figure 7.22.

We selected the regions in Φ_{min} and Φ_{max} of better trigger efficiencies were selected: $\Phi_{\text{min}} < -1$ and $0.5 < \Phi_{\text{max}} < 2$. Only events with identified muon tracks in these ranges are then accepted. The trigger efficiency ϵ_{ffo} raised to ≈ 0.88 .

Repeating all the validation analysis with this angular selection (and using the corresponding trigger efficiency $\epsilon_{\text{ffo}} = 88\%$ for normalization) finally gave the same discrepancies between data and MC as in Tables 7.1 and 7.2.

Changing the energy threshold for the reconstructed photon from 1 GeV to 1.5 GeV did not produce any relevant change in the final results.

The trigger efficiency ϵ_{ffo} is also measured in $e\mu$ events, by requiring the presence of an electron with an energy larger than 1 GeV: very similar results, both in terms of efficiency and final discrepancy between data and MC, is found.

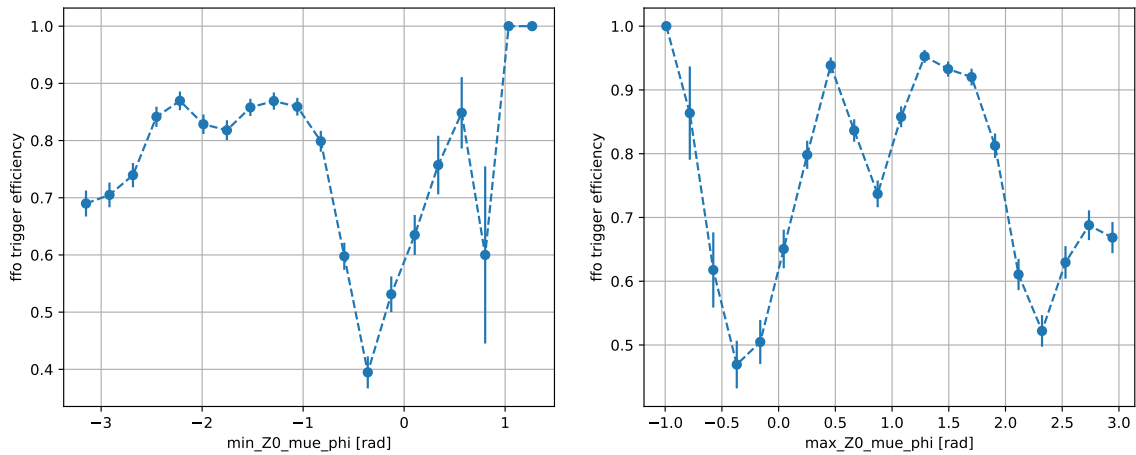


Figure 7.22: Trigger efficiency ϵ_{ffo} as a function of the minimum track azimuth angle Φ_{min} and of the maximum (left) track azimuth angle Φ_{max} (right) in $\mu\mu\gamma$ events.

By using the same technique, the efficiency of the **hie** trigger logic was measured, having as a reference the **ffo** trigger logic, in the $\mu\mu\gamma$ sample and in the $e\mu$ sample. Photon and electron reconstructed energies are required to be above 1.5 GeV in the two cases. The efficiency is measured to be $\epsilon_{\text{hie}} = 0.96 \pm 0.01$.

7.2.5 Data validation summary

All the numbers reported in the previous sections are summarized in Tables 7.1 and 7.2. The results look coherent and point to a discrepancy between data and MC of $\approx -35\%$ for $\mu\mu$ events and of $\approx -10\%$ for $e\mu$ events.

The -10% discrepancy in $e\mu$ events may be explained with tracking inefficiency (that is not properly simulated in Phase 2 MC), as evaluated in Section 7.1.2. There seems thus to be a -25% unexplained deficit in $\mu\mu$ events, which must be managed both in the background estimate and in the systematic uncertainty evaluation.

Table 7.1: First summary of the validation checks for the ratio between data and MC on the various samples. The second row shows the trigger logic used for the check. The ratios are shown for the three large recoil mass regions and for the entire recoil mass spectrum.

Region [GeV/c^2]	$\mu\mu\gamma$		$e\mu\gamma$	
	ffo	hie	ffo	hie
-2 \div 3	0.65 \pm 0.02	0.67 \pm 0.02	0.8 \pm 0.3	1.3 \pm 0.3
3 \div 6	0.84 \pm 0.07	0.76 \pm 0.07	0.9 \pm 0.1	0.95 \pm 0.13
6 \div 11	0.9 \pm 0.1	0.72 \pm 0.13	0.9 \pm 0.2	0.93 \pm 0.15
Overall	0.68 \pm 0.02	0.68 \pm 0.02	0.92 \pm 0.09	0.96 \pm 0.10

Table 7.2: Second summary of the validation checks for the ratio between data and MC on the various samples. The second row shows the trigger logic used for the check. The ratios are shown for the three large recoil mass regions and for the entire recoil mass spectrum.

Region [GeV/ c^2]	$ee\gamma$		$\mu\mu + \text{anti } \tau$	$e\mu + \text{anti } \tau$
	ffo	hie	ffo	ffo
-2 \div 3	0.88 \pm 0.01	0.99 \pm 0.01	0.66 \pm 0.06	0.94 \pm 0.07
3 \div 6	1.10 \pm 0.10	1.14 \pm 0.01	0.65 \pm 0.02	0.89 \pm 0.03
6 \div 11	2.13 \pm 0.12	1.3 \pm 0.1	0.63 \pm 0.03	0.89 \pm 0.03
Overall	0.90 \pm 0.01	0.99 \pm 0.01	0.64 \pm 0.02	0.90 \pm 0.02

7.3 Summary of the systematic uncertainties

The main systematic uncertainties affecting the measurement presented here are summarized in Table 7.3.

Regarding the measured the discrepancy in both the $\mu\mu$ (-35%) and $e\mu$ (-10%) samples, we opted for the following strategy: we assign an uncertainty of 2% to the background yields in both cases, according to the statistical precision of the measurement of the background level before the τ suppression (as discussed in Section 7.2.3); we assign an uncertainty of 22% to the signal yields in both cases (as discussed in Section 7.2.1) due to the τ suppression; we assign an uncertainty of 12.5% (half of the fully unexplained discrepancy) to the signal efficiency (only for the $\mu\mu$ sample) because of the measured discrepancy; we apply a scaling factor to the signal efficiencies and the expected background yields according to the measured discrepancy (65% for the $\mu\mu$ sample, Table 6.3, and 10% for the ee sample, Table 6.4).

We assigned an additional uncertainty of 1.5% due to the luminosity measurement.

Table 7.3: Systematic uncertainties affecting the $\mu\mu$ and $e\mu$ samples. Where not specified, they apply to both signal and background.

Source	$\mu\mu$	$e\mu$
Trigger efficiency ($\sigma_{\text{trig.}}$)	6%	1%
Tracking efficiency ($\sigma_{\text{track.}}$)	4%	4%
PID efficiency (σ_{PID})	4%	4%
Luminosity (σ_L)	1.5%	1.5%
τ suppression (background) (σ_τ)	22%	22%
Background before τ suppression (σ_{bkg})	2%	2%
Discrepancy in $\mu\mu$ yield (signal) ($\sigma_{\text{disc.}}$)	12.5%	-

Chapter 8

Statistical interpretation

In order to obtain 90% CL upper limits to the cross section (or to the efficiency times cross section for the LFV Z'), we perform a statistical analysis of our data using a Bayesian approach. In this chapter we briefly introduce the Bayesian approach for the computation of upper limits and the model used to compute them.

8.1 The Bayesian approach

The Bayesian approach is based on the Bayes' theorem:

$$p(\lambda|D) = \frac{p(D|\lambda)p_0(\lambda)}{\int p(D|\lambda)p_0(\lambda)d\lambda} .$$

It means that the probability of having a parameter λ given the data set D $p(\lambda|D)$, the *posterior* probability, is proportional to the probability of having a data set given the parameter $p(D|\lambda)$, also known as the *likelihood*, times the initial probability for the parameter $p_0(\lambda)$, the *prior* probability¹. The denominator on the right hand side of the equation, the *evidence*, is just the integral of the numerator over the allowed region of the parameter λ and it ensures that the posterior probability is normalized. The formula can also be interpreted as a learning rule: the knowledge about the parameters of a model (or the model itself) before the experiment, the prior, is updated using the probability of the new data for different values of the parameters, resulting in posterior knowledge.

Setting limits on parameters is straightforward, and just requires the integration of the posterior probability. For example, setting a 90% upper limit on the parameter λ would require solving:

$$0.9 = \int_{-\infty}^{\lambda^{90}} p(\lambda|D)d\lambda ,$$

for λ^{90} .

To compute the posterior probability and then set the upper limits, we used the Bayesian Analysis Toolkit (BAT), a software package designed to solve Bayesian statistical problems with the use of Markov Chain MC [40].

¹In this context, the term probability is used for both probability and probability density.

8.2 The model

The following equation is used to describe our model:

$$N_{\text{obs}} = \sigma \cdot L \cdot \epsilon + B ,$$

where N_{obs} is the observed number of events, L is the integrated luminosity, ϵ is the signal efficiency (scaled down by 65% for the $\mu\mu$ final state and by 10% for the $e\mu$ final state, see Section 7.3), B is the expected number of background events (scaled down by the same value used for the signal efficiency) and σ is the cross section (the parameter for which we want to compute the upper limit).

The uncertainties are taken into account in the definition of the likelihood $p(D|\lambda)$:

$$p(D|\lambda) = p\left(N_{\text{obs}} \mid \sigma \cdot L \cdot \epsilon \cdot (1 + \delta_{\text{sig}}) \cdot (1 + \sigma_{\text{disc.}}) + B \cdot (1 + \delta_{\text{bkg}}) \cdot (1 + \sigma_{\tau})\right) .$$

δ_{sig} and δ_{bkg} are the uncertainties related, respectively, to the signal and to the background, defined as

$$\begin{aligned} \delta_{\text{sig}}^2 &= \sigma_{\text{trig.}}^2 + \sigma_{\text{track.}}^2 + \sigma_{\text{PID}}^2 + \sigma_L^2 , \\ \delta_{\text{bkg}}^2 &= \delta_{\text{sig}}^2 + \sigma_{\text{bkg}}^2 , \end{aligned}$$

where the same notation introduced in Table 7.3. $\sigma_{\text{disc.}}$ and σ_{τ} are also defined in the same table. As prior probabilities associated to the parameters δ_{sig} , δ_{bkg} , $\sigma_{\text{disc.}}$ and σ_{τ} we use Gaussian distributions having mean equal to 0 and width equal to values reported in Table 7.3 and computed with the previous equations.

For the likelihood we use a Poisson distribution. For the prior probability associated to the parameter σ we use a uniform distribution between 0 fb and a proper upper limit (defined as a function of ϵ and B). For the prior probability associated to the parameter B we use a Poisson distribution. Then, we fixed the parameters L and ϵ to their values (since the uncertainty on L is already taken into account in δ_{sig} and the uncertainty on ϵ is negligible).

The upper limits to the cross section are then computed for each recoil mass bin.

Almost the same considerations hold also for the LFV Z' search. In this case, $\sigma \cdot \epsilon$ is treated as a single parameter, for which a prior probability uniform between 0 fb and a proper upper limit (defined as a function of B) is assigned.

8.3 Checking the background only hypothesis

Before computing the upper limits, we check the background only hypothesis, to look for possible anomalies in Phase 2 data. It was not possible to use the Bayes factor due to some technical issues, so we opted for the usage of the p-value², defined as the probability to get a result greater or equal than the observed one, taking into account both statistical and systematic uncertainties.

²It is important to note that it is not unusual to use p-values to look for anomalies in data and then use the Bayesian approach to set the upper limits (see, for example, [41]).

Using the same notation introduced in the previous section, we define $\delta = \delta_{\text{bkg}}$, $\delta_{\text{min}} = -5\delta$ (or -1 if $-5\delta < -1$) and $\delta_{\text{max}} = 5\delta$. We then introduce the following function:

$$f(N_{\text{obs}}, x) = \text{Poisson}(N_{\text{obs}}; B \cdot (1 + x)) \cdot \text{Gaus}(x; 0, \delta) ,$$

and the following integral:

$$I(N_{\text{obs}}) = \int_{\delta_{\text{min}}}^{\delta_{\text{max}}} f(N_{\text{obs}}, x) dx ,$$

in order to take into account the measured uncertainties that affect the expected number of background events.

The p-value is then defined as following:

$$\text{p-value} = 1 - \sum_{j=0}^{N_{\text{obs}}-1} I(j) ,$$

and it is computed for each recoil mass bin.

If no anomaly is observed (being the p-value below 0.003, that is the 3σ equivalent level) in a given bin, then the upper limit is computed for that bin.

Chapter 9

Results, prospects and summary

After getting the authorisation from the Belle II collaboration to “unblind” the $\mu\mu$ and $e\mu$ samples (see Section 3.1), we looked at the Phase 2 collisions data: the results are presented in this chapter. We then briefly report the prospects for this measurement on Phase 3 data.

9.1 Results

9.1.1 Standard Z'

First, we checked the recoil mass spectrum of the $\mu\mu$ sample on Phase 2 data before the application of the τ suppression procedure. The MC simulated samples are normalized to an integrated luminosity of 276 pb^{-1} and then scaled for the trigger efficiency (79%, see Section 7.1.1) and for the measured discrepancy (65%, see Table 7.2.5). The recoil mass spectrum is shown in Figure 9.1: the agreement between data and MC looks satisfactory over the entire spectrum.

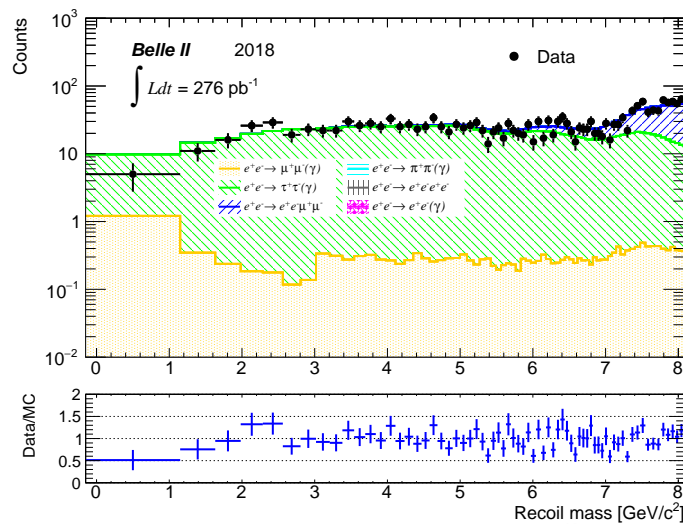


Figure 9.1: Recoil mass spectrum of the $\mu\mu$ sample before the τ suppression procedure. MC samples are normalized to an integrated luminosity of 276 pb^{-1} and scaled by a trigger efficiency of 79% and by an additional factor of 65%. The ratio between data and MC is also shown in the inset.

Then we applied the τ suppression procedure on both data and MC. We used the numbers of expected background events shown in Table 6.3 after having applied a scaling factor of 65%. The recoil mass spectrum after the τ suppression procedure is shown in Figure 9.2.

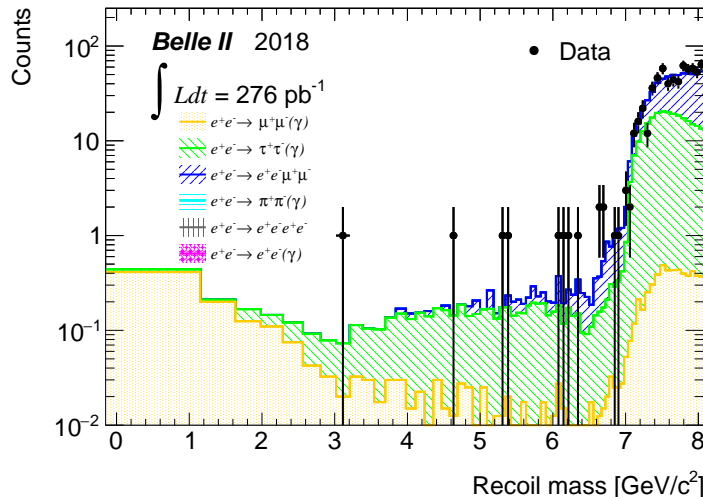


Figure 9.2: Recoil mass spectrum of the $\mu\mu$ sample after the τ suppression procedure. MC samples are normalized to an integrated luminosity of 276 pb^{-1} and scaled by a trigger efficiency of 79% and by an additional factor of 65%.

We first checked the background only hypothesis to look for possible anomalies in Phase 2 data (see Section 8.3). In Figure 9.3 we show the p-values as a function of the recoil mass: no outstanding anomaly is observed, with all the results standing well below the 3σ equivalent level.

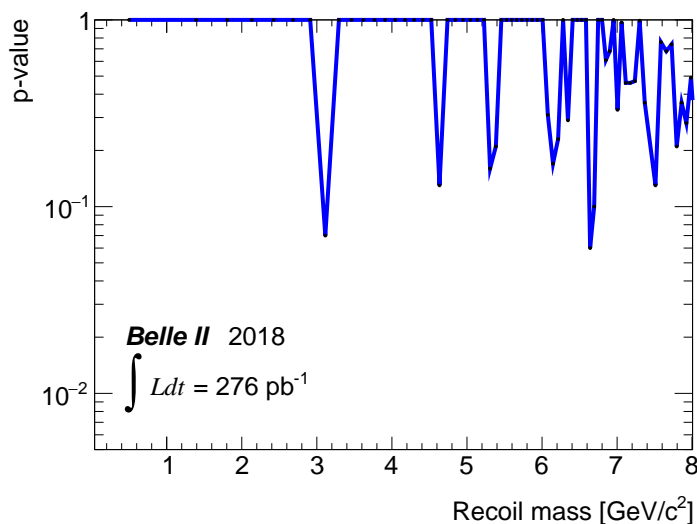


Figure 9.3: p-values as a function of the recoil mass for the $\mu\mu$ sample after the τ suppression procedure.

Since we found no anomalies, we then computed the 90% CL upper limits (as described in Chapter 8) to the cross section $\sigma[e^+e^- \rightarrow \mu^+\mu^-Z'(\rightarrow \text{invisible})]$: the results are shown in Figure 9.4 as a function of the recoil mass.

Cross section results are then translated in terms of 90% CL upper limits on the coupling

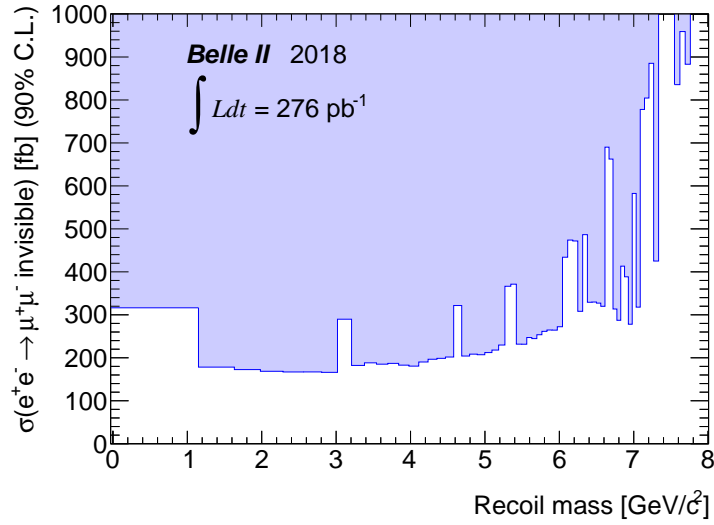


Figure 9.4: 90% CL upper limits to $\sigma[e^+e^- \rightarrow \mu^+\mu^- Z'(\rightarrow \text{invisible})]$ as a function of the recoil mass.

constant g' . These are shown in Figure 9.5 as a function of the recoil mass (denoted as $M_{Z'}$ in the plot), where only values $g' \leq 1$ are considered.

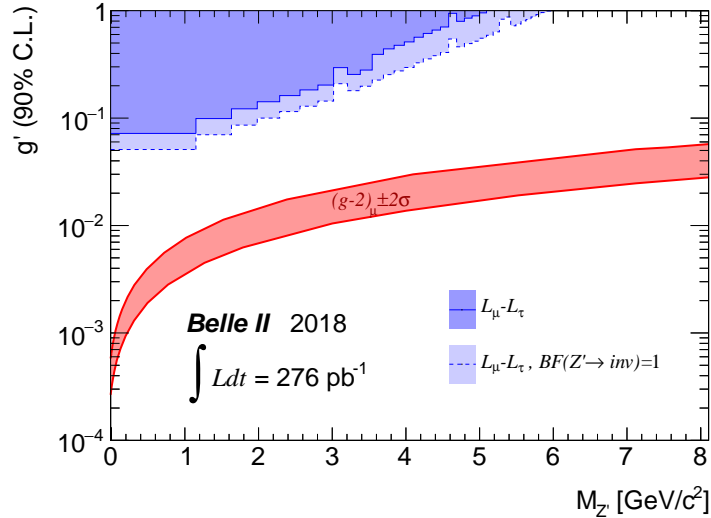


Figure 9.5: 90% CL upper limits to g' . The solid line assumes the $L_\mu - L_\tau$ predicted BF for $Z' \rightarrow \text{invisible}$ while the dashed line assumes $\text{BF}(Z' \rightarrow \text{invisible})=1$. The red band shows the region that could explain the anomalous muon magnetic moment $(g-2)_\mu \pm 2\sigma$ [4, 9].

9.1.2 LFV Z'

Similarly to as described in the previous section for the standard Z' , we first checked the recoil mass spectrum of the $e\mu$ sample on Phase 2 data before the application of the τ suppression procedure. The MC simulated samples are normalized to an integrated luminosity of 276 pb^{-1} and then scaled for the trigger efficiency (96%, see Section 7.1.1) and for the measured discrepancy (90%, see Table 7.2.5). The recoil mass spectrum is shown in Figure 9.6: the agreement between data and MC looks satisfactory over the entire spectrum.

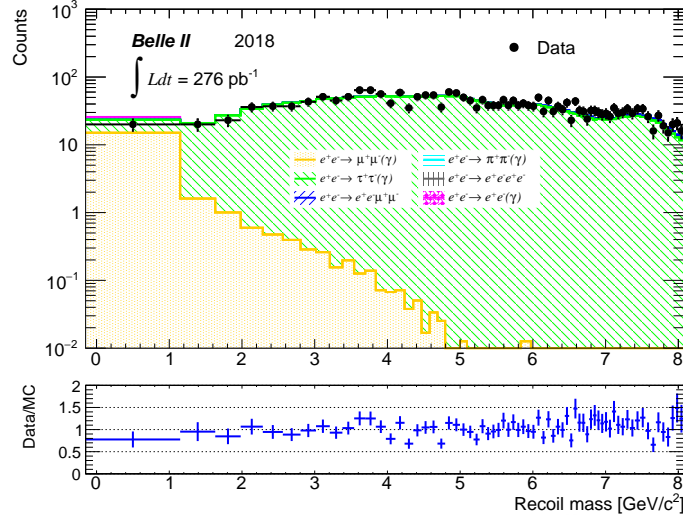


Figure 9.6: Recoil mass spectrum of the $e\mu$ sample before the τ suppression procedure. MC samples are normalized to an integrated luminosity of 276 pb^{-1} and scaled by a trigger efficiency of 96% and by an additional factor of 90%. The ratio between data and MC is also shown in the inset.

Then we applied the τ suppression procedure on both data and MC. We used the numbers of expected background events shown in Table 6.4 after having applied a scaling factor of 90%. The recoil mass spectrum after the τ suppression procedure is shown in Figure 9.7.

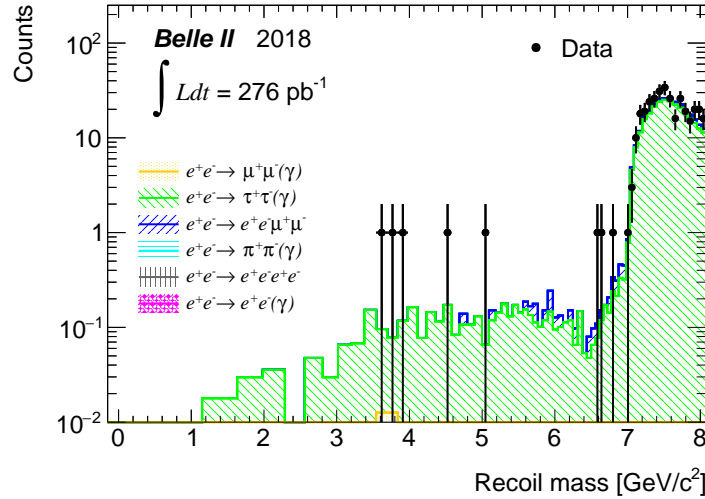


Figure 9.7: Recoil mass spectrum of the $e\mu$ sample after the τ suppression procedure. MC samples are normalized to an integrated luminosity of 276 pb^{-1} and scaled by a trigger efficiency of 96% and by an additional factor of 90%.

We first checked the background only hypothesis, to look for possible anomalies in Phase 2 data, by computing the p-values. In Figure 9.8 we show the p-values as a function of the recoil mass: no outstanding anomaly is observed, with all the results standing well below the 3σ equivalent level.

Since we found no anomalies, we then computed the 90% CL upper limits to the parameter efficiency times cross section $\epsilon \cdot \sigma[e^+e^- \rightarrow e^\pm\mu^\mp Z'(\rightarrow \text{invisible})]$: the results are shown

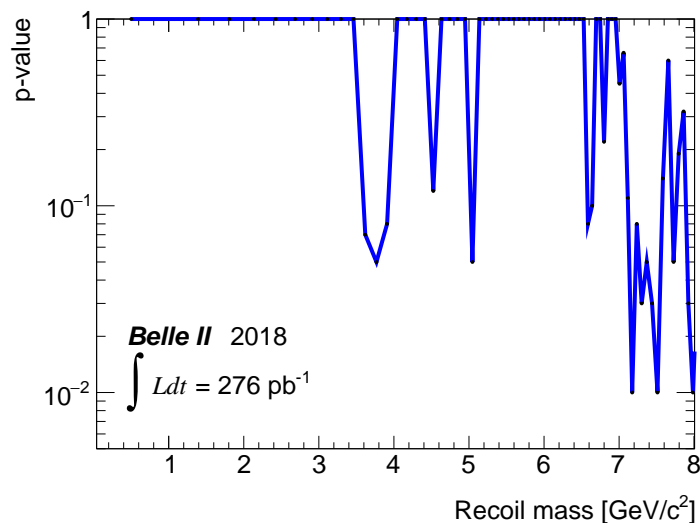


Figure 9.8: p-values as a function of the recoil mass for the $e\mu$ sample after the τ suppression procedure.

in Figure 9.9 as a function of the recoil mass.

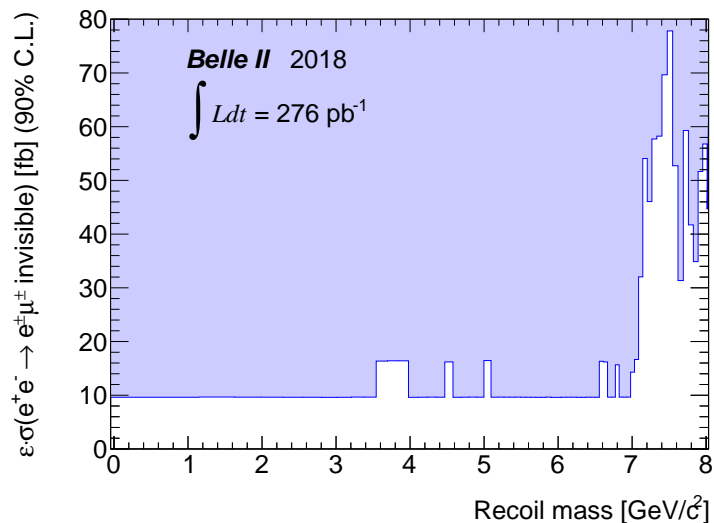


Figure 9.9: 90% CL upper limits to efficiency times cross section $\epsilon \times \sigma[e^+e^- \rightarrow e^\pm \mu^\mp Z'(\rightarrow \text{invisible})]$ as a function of the recoil mass.

As already mentioned in Section 3.1, due to the lack of a solid model for the LFV Z' , the obtained results are not further translated in upper limits to a coupling constant.

9.2 Prospects

It is currently under study the possibility to repeat this analysis using the data collected by the Belle II experiment since 2019 (Phase 3). There are three major aspects that can lead major improvements to the analysis:

- in 2019, Belle II collected about 10 fb^{-1} of collisions data (see Figure 9.10), a data set 40 times larger than the one used for the analysis presented in this work, with

improvements in overall performance;

- between Phase 2 and Phase 3 the firmware issues that affected the KLM detector were solved, improving the capability of Belle II to correctly identify the muons and heavily decreasing the pion contamination due to an ECL-based selection;
- between Phase 2 and Phase 3, the full VXD was installed, improving significantly the tracking performance and, as a direct consequence, the recoil mass resolution.

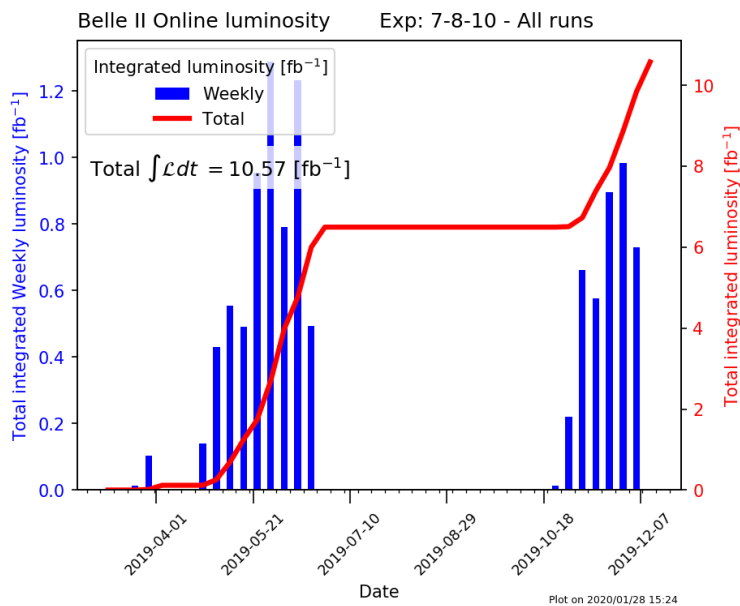


Figure 9.10: Weekly and total integrated luminosity during the 2019 data taking runs (Phase 3).

It is not trivial to evaluate the effects of all these aspects on the analysis and how much the limits on the coupling constant g' (or on $\epsilon \cdot \sigma$ for the LFV case) can improve, since we need: new MC samples (the ones used for this analysis were relying on Phase 2 geometry and beam background) a new optimization of the selection criteria (for example, in the Punzi FOM used for the τ suppression procedure the number of expected background events at a given luminosity plays a crucial role); new studies to evaluate the systematics uncertainties (for example, the uncertainty associated to the discrepancy in the $\mu\mu$ yield heavily affects the results of the upper limits calculation).

Some aspects of the current analysis strategy may change in the future: thanks to the larger statistics and reduced discrepancies between data and MC, the estimation of the background yields can be done directly from data, using a sideband technique; a more sophisticated background rejection strategy is under study, replacing the τ suppression procedure with a non-linear selection based on multivariate techniques.

Using the 2019 data set, and thanks to the improved performance of the Belle II detector, we expect to have a larger improvement of the upper limits than a simple scaling driven by the increased size of the data set, and we may start to probe, for the standard Z' , the $(g-2)_\mu$ band in some regions of the Z' mass. With the full data set of 50 ab^{-1} we expect to be sensitive to the $10^{-3} - 10^{-4} g'$ region, where the $(g-2)_\mu$ band currently lies.

With an increased data set, the $L_\mu - L_\tau$ model can be fully investigated also by looking at different and complementary final states. In particular, we foresee to look at the visible Z' final states, like $e^+e^- \rightarrow \mu^+\mu^-Z'(\rightarrow \mu^+\mu^-)$ (as already done by BaBar) or $e^+e^- \rightarrow \mu^+\mu^-Z'(\rightarrow \tau^+\tau^-)$ (never investigated so far, but more challenging from an experimental point of view).

9.3 Summary

In summary, we searched for an invisibly decaying Z' boson in the process $e^+e^- \rightarrow \mu^+\mu^-Z'(\rightarrow \text{invisible})$ and for a LFV Z' in the process $e^+e^- \rightarrow e^\pm\mu^\mp Z'(\rightarrow \text{invisible})$, using 276 pb^{-1} of data collected by the Belle II experiment in 2018.

We found no significant excess and set for the first time 90% CL upper limits to the coupling constant g' in the range from $\mathcal{O}(10^{-2})$ to 1 for the former case and to the efficiency times cross section of the order of 10 fb for the latter.

A future analysis full Belle II data set, with better muon identification, a deeper knowledge of the detector, and the use of more sophisticated techniques will probe the full $(g-2)_\mu$ band.

A paper that summarizes the results presented in this work was prepared and submitted for publication to Physical Review Letters [12].

Bibliography

- [1] X.-G. He, G. C. Joshi, H. Lew, and R. R. Volkas, *New Z' phenomenology*, Phys. Rev. D **43** (1991) R22–R24.
- [2] X.-G. He, G. C. Joshi, H. Lew, and R. R. Volkas, *Simplest Z' model*, Phys. Rev. D **44** (1991) 2118–2132.
- [3] M. Pospelov, *Secluded $U(1)$ below the weak scale*, Phys. Rev. D **80** (2009) 095002, [arXiv:0811.1030 \[hep-ph\]](#).
- [4] B. Shuve and I. Yavin, *Dark matter progenitor: Light vector boson decay into sterile neutrinos*, Phys. Rev. D **89** (2014) 113004, [arXiv:1403.2727 \[hep-ph\]](#).
- [5] W. Altmannshofer, S. Gori, S. Profumo, and F. S. Queiroz, *Explaining dark matter and B decay anomalies with an $L_\mu - L_\tau$ model*, Journal of High Energy Physics **2016** (2016) no. 12, 106, [arXiv:1609.04026 \[hep-ph\]](#).
- [6] I. Galon and J. Zupan, *Dark sectors and enhanced $h \rightarrow \tau\mu$ transitions*, Journal of High Energy Physics **2017** (2017) no. 5, 83, [arXiv:1701.08767 \[hep-ph\]](#).
- [7] I. Galon, A. Kwa, and P. Tanedo, *Lepton-flavor violating mediators*, Journal of High Energy Physics **2017** (2017) no. 3, 64, [arXiv:1610.08060 \[hep-ph\]](#).
- [8] J. P. Lees et al., BaBar Collaboration, *Search for a muonic dark force at BaBar*, Phys. Rev. D **94** (2016) 011102, [arXiv:1606.03501 \[hep-ex\]](#).
- [9] D. Curtin, R. Essig, S. Gori, and J. Shelton, *Illuminating dark photons with high-energy colliders*, Journal of High Energy Physics **2015** (2015) no. 2, 157, [arXiv:1412.0018 \[hep-ph\]](#).
- [10] K. Akai, K. Furukawa, and H. Koiso, *SuperKEKB collider*, Nuclear Instruments and Methods in Physics Research Section A **907** (2018) 188–199, [arXiv:1809.01958 \[physics.acc-ph\]](#).
- [11] F. Abudinén et al., Belle II Collaboration, *Measurement of the integrated luminosity of the Phase 2 data of the Belle II experiment*, Chinese Physics C **44** (2020) no. 2, 021001, [arXiv:1910.05365 \[hep-ex\]](#).
- [12] I. Adachi et al., Belle II Collaboration, *Search for an invisibly decaying Z' boson at Belle II in $e^+e^- \rightarrow \mu^+\mu^-(e^\pm\mu^\mp)$ plus missing energy final states*, [arXiv:1912.11276 \[hep-ph\]](#). Submitted for publication to Physical Review Letters.

- [13] M. Tanabashi et al., Particle Data Group, *Review of Particle Physics*, Phys. Rev. D **98** (2018) 030001.
- [14] V. C. Rubin, W. K. Ford, Jr., and N. Thonnard, *Rotational properties of 21 SC galaxies with a large range of luminosities and radii, from NGC 4605 ($R = 4\text{kpc}$) to UGC 2885 ($R = 122\text{kpc}$)*, Astrophysical Journal **238** (1980) 471–487.
- [15] A. G. Bergmann, V. Petrosian, and R. Lynds, *Gravitational lens models of arcs in clusters*, Astrophysical Journal **350** (1990) 23–35.
- [16] J. Jaeckel and A. Ringwald, *The Low-Energy Frontier of Particle Physics*, Annual Review of Nuclear and Particle Science **60** (2010) 405–437, arXiv:1002.0329 [hep-ph].
- [17] W. Altmannshofer, M. Baker, S. Gori, R. Harnik, M. Pospelov, E. Stamou, and A. Thamm, *Light resonances and the low- q^2 bin of R_{K^*}* , Journal of High Energy Physics **2018** (2018) 188, arXiv:1711.07494 [hep-ph].
- [18] S. R. Mishra et al., *Neutrino tridents and W - Z interference*, Phys. Rev. Lett. **66** (1991) 3117–3120.
- [19] W. Altmannshofer, S. Gori, M. Pospelov, and I. Yavin, *Neutrino Trident Production: A Powerful Probe of New Physics with Neutrino Beams*, Phys. Rev. Lett. **113** (2014) 091801, arXiv:1406.2332 [hep-ph].
- [20] T. Araki, S. Hoshino, T. Ota, J. Sato, and T. Shimomura, *Detecting the $L_\mu - L_\tau$ gauge boson at Belle II*, Phys. Rev. D **95** (2017) 055006, arXiv:1702.01497 [hep-ph].
- [21] J. Abdallah et al., DELPHI Collaboration, *Measurement and interpretation of fermion-pair production at LEP energies above the Z resonance*, Eur. Phys. J. **C45** (2006) 589–632, arXiv:hep-ex/0512012 [hep-ex].
- [22] P. Lewis, I. Jaegle, H. Nakayama, et al., *First measurements of beam backgrounds at SuperKEKB*, Nuclear Instruments and Methods in Physics Research Section A **914** (2019) 69–144, arXiv:1802.01366 [physics.ins-det].
- [23] A. Paladino, *Beam Background at SuperKEKB During Phase 2 Operation*, in Proc. 62nd ICFA ABDW on High Luminosity Circular e^+e^- Colliders (eeFACT’18), Hong Kong, China, 24-27 September 2018, no. 62 in ICFA ABDW on High Luminosity Circular e^+e^- Colliders, pp. 221–225. 2019.
- [24] T. Abe et al., Belle II Collaboration, *Belle II Technical Design Report*, arXiv:1011.0352 [physics.ins-det].
- [25] E. Kou, P. Urquijo, et al., *The Belle II Physics Book*, Progress of Theoretical and Experimental Physics **2019** (2018) no. 12, 123C01, arXiv:1808.10567 [hep-ex].
- [26] T. Kuhr, C. Pulvermacher, M. Ritter, T. Hauth, and N. Braun, Belle II Framework Software Group, *The Belle II Core Software*, Computing and Software for Big Science **3** (2019) no. 1, 1, arXiv:1809.04299 [physics.comp-ph].

- [27] J. Alwall, R. Frederix, S. Frixione, V. Hirschi, F. Maltoni, O. Mattelaer, H.-S. Shao, T. Stelzer, P. Torrielli, and M. Zaro, *The automated computation of tree-level and next-to-leading order differential cross sections, and their matching to parton shower simulations*, Journal of High Energy Physics **2014** (2014) no. 7, 79, [arXiv:1405.0301 \[hep-ph\]](#).
- [28] S. Jadach, B. F. L. Ward, and Z. Was, *The precision Monte Carlo event generator KK for two-fermion final states in e^+e^- collisions*, Computer Physics Communications **130** (2000) no. 3, 260–325, [arXiv:hep-ph/9912214 \[hep-ph\]](#).
- [29] N. Davidson, G. Nanava, T. Przedziński, E. Richter-Was, and Z. Was, *Universal interface of TAUOLA: Technical and physics documentation*, Computer Physics Communications **183** (2012) no. 3, 821–843, [arXiv:1002.0543 \[hep-ph\]](#).
- [30] F. A. Berends, P. H. Daverveldt, and R. Kleiss, *Complete lowest-order calculations for four-lepton final states in electron-positron collisions*, Nuclear Physics B **253** (1985) 441–463.
- [31] H. Czyż, M. Gunia, and J. H. Kühn, *Simulation of electron-positron annihilation into hadrons with the event generator PHOKHARA*, Journal of High Energy Physics **2013** (2013) no. 8, 110, [arXiv:1306.1985 \[hep-ph\]](#).
- [32] G. Balossini, C. Bignamini, C. M. Carloni Calame, G. Montagna, O. Nicrosini, and F. Piccinini, *Photon pair production at flavour factories with per mille accuracy*, Physics Letters B **663** (2008) no. 3, 209–213, [arXiv:0801.3360 \[hep-ph\]](#).
- [33] S. Agostinelli et al., GEANT4 Collaboration, *GEANT4 - a simulation toolkit*, Nuclear Instruments and Methods in Physics Research Section A **506** (2003) 250–303.
- [34] I. Komarov and G. Inguglia, *Performance of the CDC trigger for very low multiplicity studies in Phase 2 data*, BELLE2-NOTE-TE-2018-017, 2018.
- [35] W. Verkerke and D. P. Kirkby, *The RooFit toolkit for data modeling*, eConf **C0303241** (2003) MOLT007, [arXiv:physics/0306116 \[physics\]](#).
- [36] T. Skwarnicki. PhD thesis, Cracow INP and DESY, 1986.
- [37] G. Punzi, *Sensitivity of searches for new signals and its optimization*, eConf **C030908** (2003) MODT002, [arXiv:physics/0308063 \[physics.data-an\]](#).
- [38] I. Komarov, *Comparison of electron tracking efficiency in data and simulations using radiative Bhabha events in Phase 2*, BELLE2-NOTE-TE-2018-020, 2018.
- [39] I. Komarov, A. Martini, and G. De Pietro, *Study of muon identification performance in Phase 2 using ECL variables*, BELLE2-NOTE-TE-2018-019, 2018.
- [40] A. Caldwell, D. Kollár, and K. Kröniger, *BAT - The Bayesian analysis toolkit*, Computer Physics Communications **180** (2009) no. 11, 2197–2209, [arXiv:0808.2552 \[physics.data-an\]](#).

- [41] J. P. Lees et al., BaBar Collaboration, *Search for Invisible Decays of a Dark Photon Produced in e^+e^- Collisions at BaBar*, Phys. Rev. Lett. **119** (2017) 131804, arXiv:1702.03327 [hep-ph].